Mechanisms of rainfall-induced landsliding in Wellington fill slopes

By

Bradley Mark Cosgrove

A thesis

submitted to Victoria University of Wellington

in partial fulfilment of requirements for the degree of

Master of Science in Physical Geography

School of Geography, Environment and Earth Sciences

Victoria University of Wellington

2018

Abstract

Recent landslides from Wellington fill slopes have occurred as potentially hazardous, mobile debris flow-slides with long runouts during heavy rainstorms. Globally, catastrophic landslides from fill slopes are well documented, and in many instances their rapid failure and long runout suggests that their shear zones may be subject to liquefaction. Various generations of fill slopes throughout Wellington, and urban New Zealand, have been constructed using different practices and at variable scales. Despite this, very few laboratory based studies to determine how different fill slopes may perform during rainstorms have been attempted, as conventional laboratory tests do not adequately simulate the failure conditions in the slope.

This study uses a novel, dynamic back-pressured shear box to conduct rapid shear and specialist pore pressure inflation tests in order to replicate rainfall induced failure conditions in fill slopes with different consolidation histories and particle size characteristics. During each test, excess pore-water pressures and deformation were monitored until failure in order to determine the failure mechanisms operating.

This study demonstrates that the failure mechanisms in fill slopes are strongly influenced by the consolidation history and particle size characteristics of the shear zone materials. In over-consolidated and fine grained (< 0.4 mm) fills where cohesion is present, brittle failure was observed. In these materials, failures occur more rapidly but require much higher pore-water pressures to initiate. Conversely, normally-consolidated fill slopes constructed from coarser material (0.4 - 2 mm) fail through ductile deformation processes, which typically initiate at much lower pore-water pressures but result in a less rapid slope failure. Although liquefaction was not observed, excess pore-water pressures can be generated during rapid shearing, indicating that liquefaction could occur after a landslide has initiated in conditions where excess pore-water pressures are unable to dissipate away from the shear zone. These results provide new insights into the types of failure that may be anticipated from different fill slopes, the hazards they may pose and potential mitigation measures that could be implemented.

Acknowledgments

First and foremost, I would like to thank my supervisors Jon Carey and Kevin Norton for the help and guidance throughout my Master of Science degree. Without your expertise and assistance this project would not have gotten very far – somewhat more importantly, thanks for being easy to talk to and down to earth as this made things a lot easier.

This research was in part funded by: the Ministry of Business, Innovation and Employment through their Endeavour funded: PROP-43001-HAITR-GNS. Emerging anthropogenic slope hazards: Establishing risk assessment methods and remediation approaches for infrastructure-critical slopes; and the Landslide Hazards programme, funded by the GNS Science Strategic Science Investment Fund.

Thanks to those that assisted with laboratory work, including J. Chewings at Victoria University of Wellington, and B. Lyndsall, Z. Bruce, and J. Carey at GNS – without your help, acquiring all the data would have been very difficult. Thanks to Greater Wellington Regional Council for allowing sampling of fill material from the Priscilla Crescent site, and thanks to B. Rosser at GNS for access and assistance with the National Landslide Database. Thanks to VUW for supporting me financially through the Master's by thesis scholarship.

Huge thanks to my flatmates (Jack, Lauren, Lauren, Lucas and Tom) for always keeping the mood light and the mind fresh. Thanks to those in the J.B. library who have shared the same experience, in particular Adam, Tom, Lisa, Lucas, Maggie and Mel for keeping a cheery atmosphere, fishing trips and regular mental health breaks.

Huge thanks to my family, in particular my parents, your support and motivation throughout my entire education has been above and beyond what I could have hoped for. My brothers also deserve a mention, thanks for the support, and more importantly for the opportunity to be the only one of us with an MSc.

Last, but absolutely not least, my biggest thanks goes to my better half Lauren. I feel like you have had to experience everything over the last two years with me, but you have been there willing me along the whole time and supporting me in an assortment of ways. You are a star, and your support has been second to none.

Table of Contents

List of Figures

Chapter 1

Chapter 2

Chapter 3

Chapter 4

Chapter 5

Chapter 6

List of Tables

1 Introduction

1.1 The global fill slope hazard

Many devastating rainfall-induced landslides observed around the globe have occurred in loosely compacted fill slopes (e.g. Bishop, 1973; Blight & Fourie, 2005; Chen et al., 2004; Dawson et al., 1998; Hungr et al., 2002; Take et al., 2004). These failures can be extremely destructive and occur with very little warning, often resulting in deaths, injuries and significant damage to property and infrastructure (e.g. Bishop, 1973; Malone, 1988). Prominent examples of these catastrophic events include the 1966 Aberfan disaster in Wales and the 1972 disaster in Kowloon, Hong Kong (Bishop, 1973; Take et al., 2004).

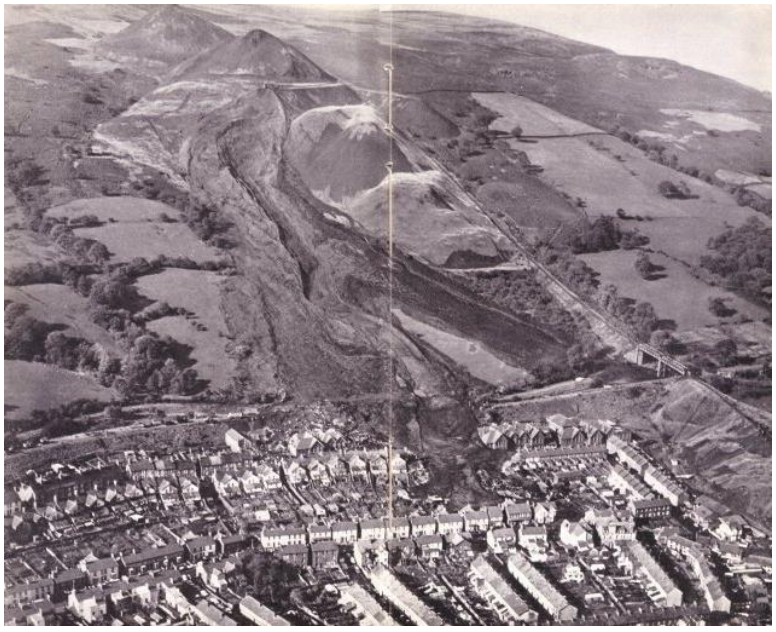

Figure 1.1: Aerial view of the Aberfan flow-slide disaster. Figure from Davies et al. (1967).

The 1966 Aberfan disaster in Wales, United Kingdom (Figure 1.1), first caught the attention of the general public, engineers, and geologists alike, highlighting the lack of knowledge surrounding the stability of spoil heaps and fill slopes. The tragedy occurred when a colliery spoil heap failed and developed into a rapid flow-slide following a period of heavy rainfall (Bishop, 1973). 100,000m^3 of material travelled 500m downslope killing 144 people, 116 of which were children (Bishop, 1973). Just as devastating was the 1972 landslide in the Sau Mau Ping district of Kowloon, Hong Kong, where three days of heavy rainfall triggered a catastrophic landslide in a decomposed granite fill (Figure 1.2). This flow-like landslide travelled approximately

160m into a temporary housing area killing 71 people and injuring 60 more (Malone, 1988; Take et al., 2004).

Figure 1.2: The 1972 Landslide in the Sau Mau Ping district of Kowloon, Hong Kong. Figure from Malone (1988).

Many other catastrophic failures have been observed globally in different types of loosely compacted fills. For example, Malone (1988) describes a series of engineered fill slope failures that killed 173 people and displaced thousands more in Hong Kong, including the 1972 Kowloon event described above; Blight (2008) describes failures in municipal waste fills, detailing three events between 1993 and 2005 that killed 464 across Turkey, Indonesia and the Philippines; and Bishop (1973); Dawson et al. (1998); Hungr et al. (2002) describe numerous failures in spoil heaps across North America and the United Kingdom. Just why these failures can be so destructive is because of the fluidised failure behaviour they commonly exhibit.

The characteristic behaviour of many fill slope failures, including those described above, is that they occur with little or no warning and display highly mobile, fluidised motion and long runout distances; features that together account for their extremely destructive nature (Bishop, 1973; Blight & Fourie, 2005; Dawson et al., 1998). In most cases, rainfall and changing pore pressure conditions play a leading role in triggering these failures, while liquefaction has been suggested as the mechanism responsible for failure and the reason for fluidised failure behaviour in many instances (e.g. Bishop, 1973; Dawson et al., 1998; Take et al., 2004).

1.2 The fill slope hazard in Wellington, New Zealand

Loosely compacted engineered fill slopes are a common form of earth surface modification across many urban centres in New Zealand, including Wellington. These anthropogenic slopes have been constructed at various scales, through varying engineering practices during the city's development. Although the fill slopes that are presently constructed are required to adhere to strict design regulations, several significant failure events over the past 11 years in the Wellington Region have brought into question the reliability of some fill slopes during intense rainfall. These include the 2013 and 2017 events that were less than 200 metres apart in the Wellington City suburb of Kingston (Hunt & George, 2017). Whilst these failures did not result in the catastrophe observed in Aberfan or Kowloon, they were characterised by failure behaviours analogous to those devastating events witnessed globally and described above. This may suggest that the hazard posed by some of Wellington's fill slopes may not be fully understood, as to effectively determine landslide hazard requires a detailed knowledge of the potential mechanisms and behaviour of slope failure (Aleotti & Chowdhury, 1999; Dai et al., 2002). Despite this, few laboratory based studies have yet considered how different fill slopes in Wellington may perform during intense rainfall events.

It is clear that rainfall-induced landslides in fill slopes pose a significant global hazard due to their fluidised failure behaviour. It is also apparent that the hazard posed by some of Wellington's fill slopes may not be fully understood, as their potential failure behaviour is not well known. To more accurately classify the hazard posed by Wellingtons fill slopes requires a greater understanding their potential failure behaviour, which itself requires a detailed understanding of the key mechanisms acting during shear zone formation.

1.3 Study aims and objectives

This study aims to better understand the potential failure behaviours of loosely compacted engineered fill slopes in Wellington, New Zealand.

The key objectives are to:

1. Investigate mechanisms of shear surface development in different fill materials under changing pore-water pressure conditions using specialist laboratory testing.

2. Infer from the results obtained what the potential hazard posed by Wellington's fill slopes may be.

Specifically, the following research questions will be answered:

1. How does strain accumulate in different fill materials in response to changing pore-water pressure conditions?
2. What is the pore-water pressure response of different fill materials to rapid shear?
3. How do particle size distribution and consolidation history influence 1) and 2) above.

1.4 Thesis structure

This thesis consists of seven chapters, detailing the information necessary to give the reader a robust understanding of the study and its key findings.

- **Chapter 1** (this chapter) provides an introduction to the research by outlining its relevance. It also details the aims and objectives of the study, as well as explaining the structure of the thesis.
- **Chapter 2** gives a comprehensive background to the thesis, describing the fundamentals of slope stability, different types of landslide movement, and the use of laboratory testing and theoretical models to determine the movement types and subsequent hazard of specific landslides.
- **Chapter 3** describes the regional setting of the site location (Wellington, New Zealand) and provides context for the potential fill slope hazard.
- **Chapter 4** outlines the methodologies employed for sample collection, physical property analyses, and specialist laboratory testing using the dynamic back-pressured shear box.
- **Chapter 5** details the data collected from the physical property testing of the fill material, and provides an analysis of data collected through dynamic back-pressured shear box testing.
- **Chapter 6** discusses the implications of the results collected in correlation with relevant knowledge. In particular, potential movement behaviours and the influence of particle-size and consolidation history are discussed, before the possible implications for fill slope behaviour in Wellington is suggested.

- **Chapter 7** concludes the thesis by highlighting the key findings and how they contribute to the current understanding of fill slope failure behaviour, with focus on the implications for Wellington, New Zealand.

2 Background

2.1 Fundamentals of slope failure

Landslides occur when slope forming materials move down-slope under the influence of gravity in order to find a more stable state (Selby, 1993; Varnes, 1978). This failure most commonly occurs along a shear surface or zone where a balance of shear force and shear resistance exists (Figure 2.1).

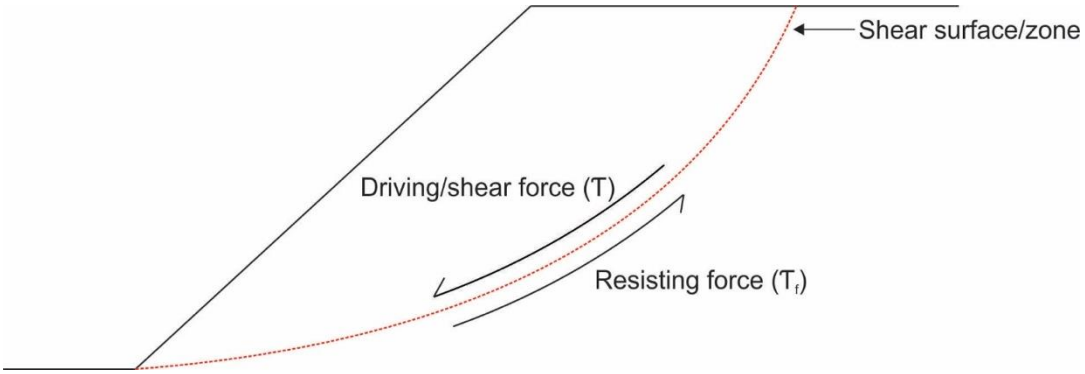

Figure 2.1: Basic forces acting in a landslide.

Failure is generally caused when the sum of forces promoting motion (shear forces, τ) exceed those resisting it (shear resistance, τ_f). This relationship is commonly expressed as the Factor of Safety (FoS) (Selby, 1993):

$$FoS = \frac{Shear\ resistance}{Shear\ forces} = \frac{\tau_f}{\tau} \qquad \textit{Equation 2.1}$$

Where τ_f = shear strength and τ = shear stress

When the shear forces are equal to the shear resistance, then the FoS is equal to 1 and the forces are in equilibrium. When the FoS is > 1, the slope is likely to be stable as the forces resisting motion are greater than those promoting it. Conversely, when the FoS is < 1, the slope is likely to be unstable as the opposite is true.

The importance of the relationship between shear stress (τ) and shear strength (τ_f) in the problem of slope stability necessitates the need for a comprehensive understanding of those (τ & τ_f) components and how they are derived in soil mechanics.

In soil mechanics, the shear stress acting upon a slope is a function of the mass of the soil body above (W), and the inclination of the shear surface (β) as shown in Figure

2.2 (Sidle & Ochiai, 2006). Where with increasing inclination of the shear surface (β) a greater shear stress acts upon the body.

$$\tau = W sin\ \beta \qquad \textit{Equation 2.2}$$

The shear strength (τ_f) of a soil, which is defined as the ability of the solid-particle skeleton to resist shear, is expressed in the Mohr-Coulomb equation (Selby, 1993);

$$\tau_f = c' + (\sigma - u)\ tan\ \varphi' \qquad \textit{Equation 2.3}$$

where the shear strength (τ_f) is a function of apparent cohesion (c'), normal stress (σ), pore-water pressure (u) and the effective internal angle of friction (φ'), where $\sigma - u$ represents the effective normal stress (σ').

In the Mohr-Coulomb equation (*Equation 2.3*), cohesion describes the bonding between particles, and most commonly results from the presence of water (capillary action), electrostatic bonds and cementing materials (Selby, 1993). The internal angle of friction describes the ability of particles to move past each other, and is influenced by grain orientation, shape and size (Selby, 1993). And finally, the normal stress is created by the weight of the slope above the shear surface – the same force that produces the shear stress. It acts normal (at a right angle) to the shear surface, and depends on the mass of the soil body above (W) and the inclination of the shear surface (β) (Figure 2.2) (Crozier, 1986):

$$\sigma = W cos\ \beta \qquad \textit{Equation 2.4}$$

As the inclination of the shear surface (β) increases, the stabilising force of the normal stress decreases.

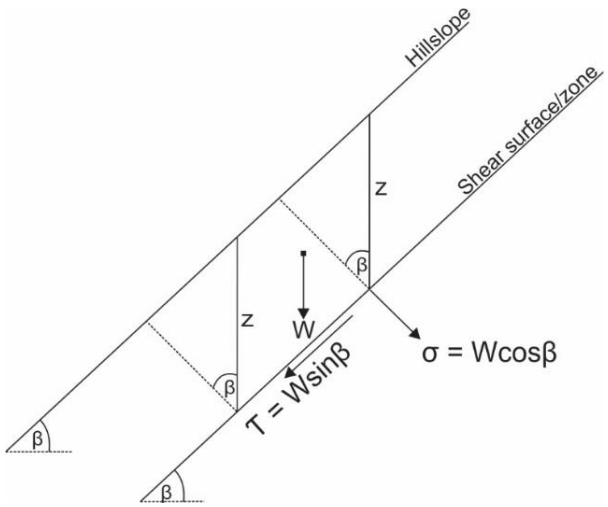

Figure 2.2: Forces acting in a landslide. Figure after Selby (1993).

Based on *Equations 1.2, 1.3 & 1.4*, the FoS (*Equation 2.1*) can now be written as:

$$FoS = \frac{c' + (\gamma z cos^2\beta - u) tan\varphi'}{\gamma z sin\beta cos\beta} \qquad \textit{Equation 2.5}$$

Where c' is the effective cohesion, γ is the unit weight of the soil (at its natural moisture content), z is the soil depth in the direction of normal stress, β is the slope's inclination, u is the pore-water pressure and φ' is the effective internal angle of friction (Selby, 1993).

Another common method for expressing and evaluating the shear strength of a slope is by using a Mohr circle that is defined by the effective principle stresses σ'_1 and σ'_3 at a particular failure point of interest (Figure 2.3) (Craig, 2004). A tangential line, denoted by *Equation 2.3*, to the Mohr circle representing the stress state at failure is known as a *failure envelope*. Any stress state represented by a point above the line is theoretically impossible (Craig, 2004).

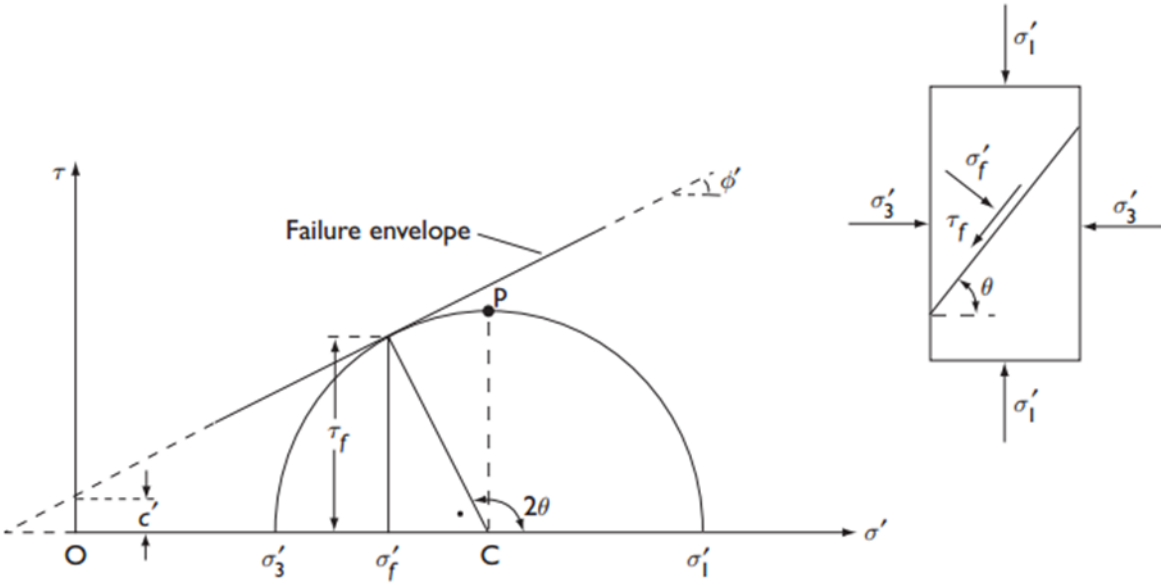

Figure 2.3: Mohr-Coulomb failure criterion for stress conditions at failure. Where c' = effective cohesion, φ'= effective friction angle, σ'_1 and σ'_3= principle stresses, τ_f= shear strength, σ'_f= effective normal stress at failure, Θ = theoretical angle between major principle plane and plane of failure. Figure from Craig (2004, p. 93).

Understanding and being able to conceptualise the fundamental driving and resisting forces present in landslide mechanics provides key insights into the issue of slope stability. However, it should be noted that these methods are a simplification and parameter acquisition is associated with inherent uncertainty.

2.2 Landslide classification

Landslides are extremely complex, with the many processes, controls, and materials involved resulting in a great variety of movement types; in terms of both form and rate (Selby, 1993). Consequently, many definitions of a landslide exist, such as those proposed by Varnes (1978), Cruden (1991) and Crozier (1999). Varnes (1978) defined a landslide as the downward and outward movement of slope-forming materials under the influence of gravity. This is one of the most widely used definitions of a landslide and will provide ample context for this research.

Arising from the complexity of landslides and the range of definitions proposed, various landslide classification schemes have also been suggested (e.g. Cruden & Varnes, 1996; Hungr et al., 2014; Nemčok et al., 1972; Varnes, 1958, 1978). One of the most widely adopted classification schemes is that proposed by Varnes (1978), which was later refined by Hungr et al. (2014) (Table 2.1). The updated scheme proposed by Hungr et al. (2014) details 32 types of landslides, with the major development from that proposed by Varnes (1978) being the refinement of the terminology used to describe the landslide-forming material.

Table 2.1: Mass movement type classification from Hungr et al. (2014). Note that '' identifies movement types that commonly reach 'extremely rapid' (> 5x10^3 mm/sec) movement rates as defined by Cruden and Varnes (1996)*

Type of movement	Rock	Soil
Fall	Rock/ice fall*	Boulder/debris/silt fall*
Topple	Rock block topple*	Gravel/sand/silt topple*
	Rock flexural topple	
Slide	Rock rotational slide	Clay/silt rotational slide
	Rock planar slide*	Clay/silt planar slide
	Rock wedge slide*	Gravel/sand/debris slide*
	Rock compound slide	Clay/silt compound slide
	Rock irregualr slide*	
Spread	Rock slope spread	Sand/silt liquefaction spread*
		Sensitive clay spread*
Flow	Rock/ice avalanche*	Sand/silt/debris dry flow
		Sand/silt/debris flowslide*
		Sensitive clay flowslide*
		Debris flow*
		Mud flow*
		Debris flood
		Debris avalanche*
		Earthflow

		Peat flow
Slope deformation	Mountain slope deformation Rock slope deformation	Soil slope deformation Soil creep Solifluction

Materials are broadly classified as either rock or soil, with sub-categories within those as ‘rock’, ‘ice’, ‘clay’, ‘silt’, ‘sand’, ‘gravel’, ‘boulder’, ‘peat’, ‘mud’ and ‘debris’. Hungr et al. (2014) used these descriptors as they best align with both geological and geotechnical terminology and ultimately proved the greatest insights into the mechanical properties of the materials.

Movement type can then be categorised as either a ‘fall’, ‘topple’, ‘slide’, ‘spread’, ‘flow’ or ‘slope deformation’. A ‘fall’ can be identified by a free-falling movement of a material from a steep slope where little (or no) shear displacement takes place along the failure surface. A ‘topple’ is a similar movement, however, it is characterised by the forward rotation about some axis. ‘Slides’ occur where the failure takes place along a discrete shear surface or shear zone, and can be subdivided into ‘rotational’ and ‘translational slides’; where failure occurs on a circular slip-surface for rotational slide and on a planar surface for translational slides. A ‘lateral spread’ generally occurs on low angled slopes and involves the extension and subsidence of a cohesive mass of material. ‘Flows’ are a spatially continuous movement and generally behave similarly to a viscous liquid due to the amount of liquid and/or air involved. The ‘slope deformation’ movement type was an addition made by Hungr et al. (2014) to the original classification scheme by Varnes (1978), and is characteristic of extremely slow movement rates, often manifesting itself as visible geomorphic features such as scarps, sags, bulges and cracks, but notably no defined failure surface. The ‘complex’ landslide category was removed by Hungr et al. (2014) from the original scheme, as they explain it is not a useful term. In saying this, the authors do acknowledge that it is often the case that more than one unique term is required to describe a landslide, and in fact that most landslides are complex to some degree.

Another important characteristic used in landslide classification is the velocity of a landslide or its ‘rate of movement’. Rate of movement is a fundamental component to consider because of the controlling factor it has on the probable destructiveness of a landslide, as a faster moving mass has a larger force behind it. In some cases the rate of

movement is included in a complete landslide classification scheme such as that proposed by Nemčok et al. (1972), however, others such as Cruden and Varnes (1996) have created a separate rate of movement classification scheme (Table 2.2) to be used in conjunction with classification based on movement type.

Table 2.2: Landslide velocity classes, after Cruden and Varnes (1996).

Velocity class	Description	Velocity
1	Extremely slow	up to 16mm/yr
2	Very slow	up to 1.6m/yr
3	Slow	up to 13m/yr
4	Moderate	up to 1.8m/hr
5	Rapid	up to 3m/min
6	Very rapid	up to 5m/sec
7	Extremely rapid	more than 5m/sec

Whilst classification schemes based on characteristics such as the material(s) involved, rate, and type of movement are numerous, schemes based on geotechnical characteristics that provide fundamental information regarding failure mechanisms and behaviours – which are essential to effective hazard mitigation, are rare. The notable exception to this however, is the geotechnical classification proposed by Sassa (1989).

Sassa (1989) proposes a scheme that classifies based on grainsize and the type of shearing during failure (Table 2.3). Grainsize is used because of the significant effects it has on shear behaviour (through friction angles and pore pressure generation), with 'rock', 'sandy soil' and 'clayey soil' being chosen because of the varying characteristics they represent. The types of shear used in the scheme are described as 'slides', 'liquefaction' and 'creep', and are explained using their simplified stress paths during failure (Figure 2.4).

Table 2.3: Geotechnical landslide classification scheme, modified after Sassa (1989).

	Grain size of the material		
Type of Shear	Rock (20mm)	Sandy soil (20-0.074mm)	Clayey soil (0.074mm)
1. Slides			
A) Peak strength slide	Peak strength rock slide (Rock avalanche)	Sandy peak strength slide	Clay peak strength slide
B) Residual state slide	Residual strength rock slide	Sandy residual strength slide	Clay residual strength slide

2. Liquefaction	None	Soil creep	Quick clay landslide
3. Creep	Rock creep	Soil creep	Clay creep

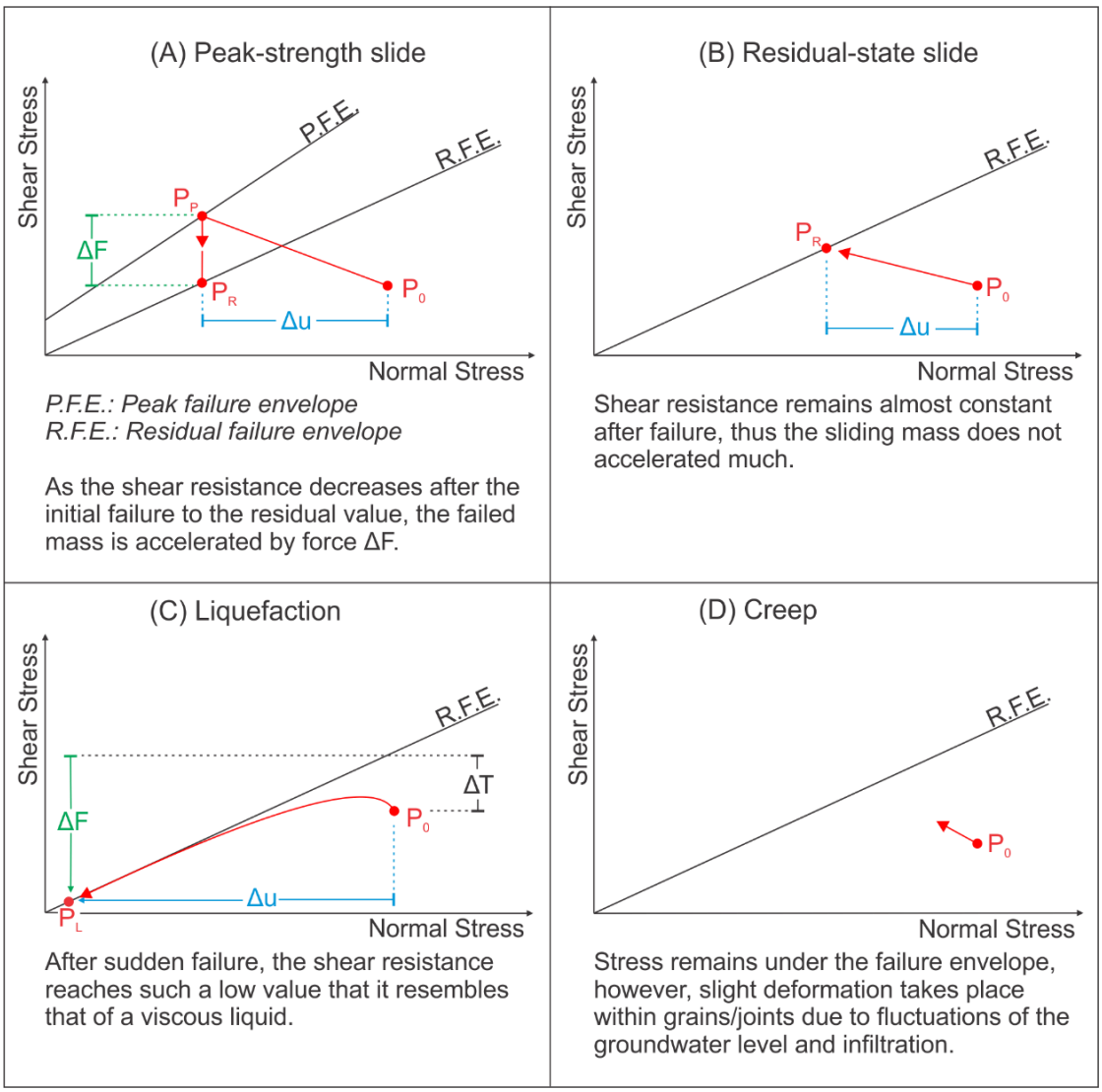

Figure 2.4: Simple stress path diagrams for the geotechnical classification of landslides. Figure after Sassa (1989).

A 'peak strength slide' occurs when the stress acting within a slope reaches its undisturbed failure envelope, and movement then occurs along a slip-surface. When the pore-pressure in the slope increases, the effective stress acting within the slope decreases from P_0 (the initial state) towards the peak strength failure envelope by an amount Δu (Figure 2.4 A, Equation 2.6).

$$\sigma' = P_p = P_o - \Delta u \quad \textit{Equation 2.6}$$

Once the failure envelope is reached (P_P), sliding motion begins. Following the initiation of movement, the shear surface state moves quickly to the residual state,

where an imbalance of forces between the shear stress and resistance is created (Sassa, 1989). This causes accelerated landslide motion, often leading to rapid landslides where a substantial difference between the shear stress and shear resistance exists.

Alternatively, if the shear surface or shear zone is already in the residual state then a 'residual strength slide' occurs. Motion begins when the effective stress reaches the residual strength failure envelope (P_R). However in this case, shear resistance does not decrease and is more likely to remain constant (Figure 2.4 B). This often results in slow movement rates where a minor recovery in the stress state is able to stabilise motion (Sassa, 1989).

'Liquefaction' occurs when a saturated, loose soil mass experiences undrained loading, causing the soil structure to fail without exerting its frictional shear resistance (i.e. it does not reach the failure envelope) (Sassa, 1989). During failure, the effective stress of the soil body decreases significantly (to point P_L on Figure 2.4 C) resulting in the initiation of flow-like movement due to the extremely low frictional resistance experienced (Sassa, 1989).

Lastly, Sassa (1989) refers to 'creep' as the slow movements that occur in a natural slope resulting from fluctuations in groundwater levels and thus stress. As groundwater levels fluctuate the effects of drainage and saturation also adjust, causing partial movements of very unstable slope-forming materials, with the stress never reaching the failure envelope (Figure 2.4 D) (Sassa, 1989).

The different classification schemes presented here, as well as others that have not been mentioned or discussed, all provide a useful framework for classifying landslides. However, the underperformance of these classification schemes is evident. Most schemes do not identify geotechnical characteristics essential for effective hazard management, and almost all schemes fail to account for the variable failure mechanisms that often operate during a landslide; resulting in most schemes classifying landslides as complex - ultimately providing limited beneficial understanding. New research that helps further the knowledge surrounding relationships between failure mechanisms and physical properties of materials will help provide useful insights for future classification schemes.

2.3 Factors that influence landsliding

As discussed in Section 2.1, slope stability is governed by the relationship between the shear and resisting forces acting upon and within a slope, while failure is driven by the many factors that transition this relationship into an unstable state. In the majority of cases, it is the interplay of several factors that will ultimately be responsible for any given failure, often creating complexity in discerning those responsible (Crozier, 1986; Selby, 1993). Cruden and Varnes (1996) and Selby (1993) have broadly differentiated these causal factors based on whether they:

1) Increase the shear stress (τ) acting upon a slope; or

2) Reduce the shear strength (τ_f) acting within a slope.

Examples of common causal factors as suggested Selby (1993) are presented in Table 2.4.

Table 2.4: Factors that influence hillslope instability. Table from Selby (1993, p. 276).

A. Factors increasing shear stress	
Types	Major mechanisms
1. Removal of lateral support	i) Stream, water or glacial erosion ii) Subaerial weathering, wetting, drying and frost action iii) Slope steepness caused by mass movements iv) Removal of toe-slopes by human activity e.g. quarries or road cuttings
2. Overloading by	i) Weight of rain, snow, talus ii) Fills, waste piles, structures
3. Transitory stresses	i) Earthquakes - ground motions and tilts ii) Vibrations from human activity - blasting, traffic, machinery
4. Removal of underlying support	i) Undercutting by running water ii) Subaerial weathering, wetting, drying and frost action iii) Subterranean erosion (eluviation of fines or solution of salts), squeezing out of underlying plastic soils iv) Mining activities, creation of lakes, reservoirs
5. Lateral pressure	i) Water in interstices ii) Freezing of water iii) Swelling by hydration of clay iv) Mobilisation of residual stress
6. Increase of slope angle	i) Regional tectonic tilting ii) Volcanic processes

B. Factors reducing shear strength	
Types	Major mechanisms
1. Composition and texture	i) Weak materials such as volcanic tuff and sedimentary clays
	ii) Loosely packed materials
	iii) Smooth grain shape
	iv) Uniform grain sizes
2. Physico-chemical reactions	i) Cation (base) exchange
	ii) Hydration of clay
	iii) Drying of clay
	iv) Solution of cements
3. Effects of pore-water	i) Buoyancy effects
	ii) Reduction of capillary tension
	iii) Viscous drag of moving water on soil grains, piping
4. Changes in structure	i) Spontaneous liquefaction
	ii) Progressive creep with reorientation of clays
	iii) Reactivation of earlier shear planes
5. Vegetation	i) Removal of trees
	a) reducing normal loads
	b) removing apparent cohesion of tree roots
	c) raising of water tables
	d) increased soil cracking
6. Relict structures	i) Joints and other planes or weakness
	ii) Beds of plastic and impermeable soils

It is clear that many factors exist that can influence landsliding, and because of multiple causality and their transposable nature, identifying those responsible for a particular failure event can be an extremely complex task. One of, if not the most important factor that has the ability to influence slope stability and trigger landslides through a variety of ways is rainfall.

2.3.1 Rainfall as a failure mechanism

The role of rainfall in slope failure will be the only causal factor discussed in detail; partly because it is one of the most influential factors, but more importantly because it is the focal point of this research.

Rainfall is one of the primary causes of landsliding across the globe, and as a result, the role it plays in slope failure is well-studied and well-documented (e.g. Crosta & Frattini, 2008; Selby, 1993; Terzaghi et al., 1996). Rainfall has the ability to influence slope stability through many mechanisms as discussed by Selby (1993) and Crozier

(1986), including via the hydration of clays, decreasing soil aggregation, and through viscous drag on soil particles. However, it is the role of pore-water pressure that is arguably the most significant.

The effect of pore-water pressure

Pore-water pressure (PWP) refers to the pressure the water present in the pores of rock or soil exerts on its surroundings. In general, three states of PWP can exist in a soil body (Figure 2.5). In a completely dry soil (Figure 2.5 A), there is zero PWP as the soil structure is completely supported by the grain-to-grain contacts. In a partially saturated soil (Figure 2.5 B) negative PWPs develop as moisture around the soil particles and subsequent surface tension forces generate a suction effect, imparting apparent cohesion on the soil body (Selby, 1993). In a fully saturated soil (Figure 2.5 C), no apparent cohesion exists as the surface tension forces are lost, and a portion of the load supplied by the normal stress is transferred to the soil-water from the soil-fabric. These conditions create positive PWPs, where the transfer of load to the soil-water creates a buoyancy force (Selby, 1993).

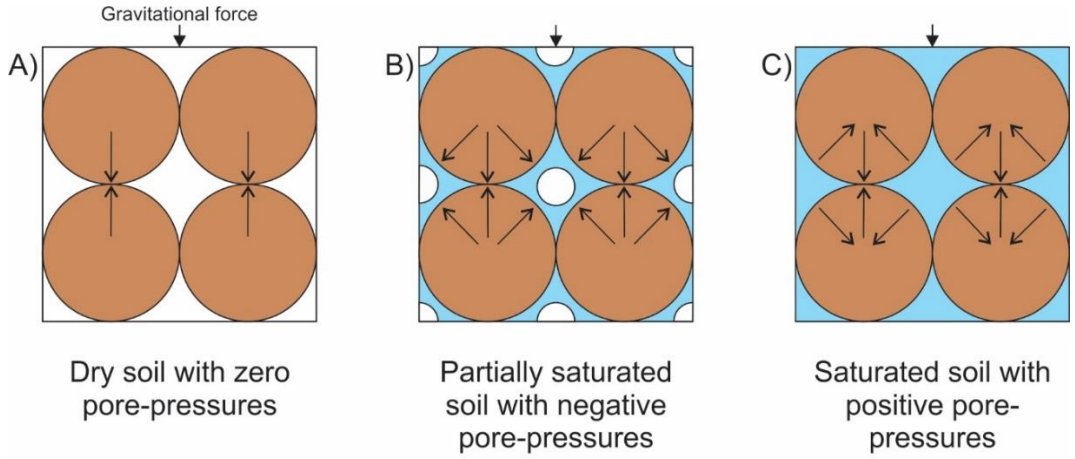

Figure 2.5: States of pore-water pressure in soils. Figure after Selby (1993, p. 58).

The role of PWP in slope stability is best and most simply illustrated using the Mohr-Coulomb equation (*Equation 2.3*). In the most simple terms, a negative PWP (u) leads to a higher shear strength (τ_f), whereas a positive PWP leads to a lower shear strength i.e. the loss of negative PWPs or the development of positive PWPs reduces the shear strength of the slope, increasing its susceptibility to failure.

Rainfall-induced landslides generated by changing pore-pressure conditions are common, and strongly influenced by both the characteristics of the rainfall and the physical properties of the subjected soils (Collins & Znidarcic, 2004; Rahardjo et al.,

2007). Of the soil properties, the hydraulic conductivity of the soil is one of the most important, as it has a large control on the pore-pressure conditions that are able to develop. For example, Collins and Znidarcic (2004) illustrate that, under the same rainfall conditions, it is easier for positive PWPs to develop in a soil with a lower hydraulic conductivity than a soil with high hydraulic conductivity. Furthermore, rainfall characteristics, such as intensity and duration have a significant influence on the type and likelihood of failure as well (e.g. Rahardjo et al., 2007; Tsai, 2008). Of these, it is possibly the role of rainfall intensity that is the most important, as greater intensity rainfall is better able to generate positive PWP conditions. As a result, intense rainstorms are often associated with shallow landsliding that can be characterised by rapid, fluidised movements (e.g. Sassa, 2000; Wang et al., 2002). Additionally, the relationship between the intensity and duration of rainfall has been well studied, with many intensity-duration thresholds being proposed for various locations (e.g. Eyles et al., 1978; Guzzetti et al., 2007). Fundamentally, it requires a shorter period of intense rainfall, or a longer period of less intense rainfall to generate failure (e.g. Caine, 1980; Guzzetti et al., 2008).

2.4 Landslide movement types

Due to extensive landslide monitoring through time, data exists that illustrates various landslide movement types. These movement types include many different accelerating, decelerating and stable regimes. Understanding these different types of movement can lead to improved management of landslide hazards through a greater knowledge of the processes acting at the shear surface (Aleotti & Chowdhury, 1999; Dai et al., 2002) . Additionally, studies of landslide movement patterns have has also led to significant inroads into landslide forecasting and prediction (Massey et al., 2013; Petley, 2010; Petley et al., 2002).

The early work of Allison and Brunsden (1990) investigated movement patterns in coastal mudslides, and suggested that they exhibit four key types of movements, largely in response to changing PWP conditions.

1. Multiple small stick-slip like movements, interspersed with periods of zero displacement. Gradual PWP accumulation preceded small slips, shortly followed by a fall in PWP and subsequent stabilisation.
2. Temporally discrete ‘graded’ movements, characterised by a single continuous movement, generally tens of centimetres of movement over a period of tens of

hours. Movement was preceded by a slow build-up in the phreatic surface, with the rate increasing as movement commenced. The phreatic surface would then decline towards normal values resulting in halted movement.

3. Relatively large, rapid displacements over a short period termed ‘surges’; generally in the order of metres over periods of tens of minutes. A rise in PWP at the toe and top of the slope preceded movement, and rose rapidly near the top when movement commenced.
4. Irregular small displacements associated with internal adjustments and wetting/drying cycles.

A similar role of PWP was found by Carey et al. (2015) in the Ventnor landslide complex in the south of England. Carey et al. (2015) found that the complex displayed two movement types during the monitoring period: a slow background movement, and an increased rate of movement. The slow background movement was at a continuous rate of approximately 5-10mm/year, and while no definitive deformation mechanism was established for this type of movement, they observed that changing PWP was not reflected in changes to deformation (when PWP was below the threshold established for the second movement type). The second movement type recognised was periods of an increased deformation rate in response to a rise in PWP. It was identified that when PWP rose above approximately 107kPa there was a significant, non-linear relationship between increased PWP and increased deformation rate. Carey et al. (2015) suggested that as PWP appeared to govern movement in the second (faster) movement type, but not in the first, that multiple failure mechanisms may be operating within the slope; analogous to the behaviour discussed above and observed elsewhere (e.g. Allison & Brunsden, 1990; Massey et al., 2013). Importantly, in this investigation, by identifying the movement types present, Carey et al. (2015) were able to better constrain the hazard faced by the population of approximately 6000 situated on the complex; ultimately concluding that under the current conditions the probability of a catastrophic failure is low.

While the movement types discussed so far account for considerable damages to infrastructure and still pose a hazard to people and property, they do not describe the rapid movements of landslides which are often the most devastating (e.g. Bishop, 1973; Dawson et al., 1998; Lavigne et al., 2014; Wang et al., 2002). Unfortunately,

due to the rapid and unpredictable nature of these events, specific details of the failure process often have to be inferred from post-failure observations.

Bishop (1973) discusses the movement types of rapid failures in spoil heaps, detailing as much as possible from personal recounts of the events and post-failure observations. For example, the Abercynon spoil heap failure involved an initial rotational slip, likely triggered by rising PWPs, which then transitioned into a rapid flow-slide depositing material approximately 400m from the source. Although no measurements of speed could be made, it was estimated the speed of the flow-slide was in the order of tens of kilometres per hour. Similarly, Bishop (1973) also discusses the catastrophic Aberfan flow-slide which occurred in a spoil heap and ultimately killed 144 people as mentioned earlier. This disaster began when a group of workers at the site noticed the crest of the spoil heap had subsided 3m when they arrived on site one morning, before it had sunk a further 3m and hour later. Approximately 40 minutes later, the toe of the heap was observed to begin creeping, before it transitioned into a rapid flow-slide which travelled 500m at a speed of approximately 16-34km/hr. This disaster was attributed to the development of a zone of positive PWPs below the material initiating liquefaction (Bishop, 1973; Davies et al., 1967). Similar rapid acceleration-to-failure movements in landslides have been observed and studied by others such as Wang et al. (2002), Dawson et al. (1998) and Lavigne et al. (2014), with these movements commonly being attributed to failure mechanisms associated with increased PWPs, and in many cases liquefaction.

In a more general sense, Petley et al. (2002) investigated landslide movement types in a variety of materials and settings, finding that all accelerating regimes exhibited one of two trends. The first type of movement, recognised previously by Saito (1965, 1969), is that of events characterised by catastrophic acceleration. Petley et al. (2002) demonstrated that this movement type is typified by a linear trend in 1/Velocity-time space (Figure 2.6 A), and results from first-time failures caused by crack-propagation (shear surface development). The second movement type identified by Petley et al. (2002), is that where movement rates trend towards steady-state behaviour (constant velocity), and is characterised by an asymptotic trend in 1/Velocity-time space (Figure 2.6 B). It was suggested by Petley et al. (2002) that this movement type results from ductile deformation processes by failure on antecedent planes of weakness.

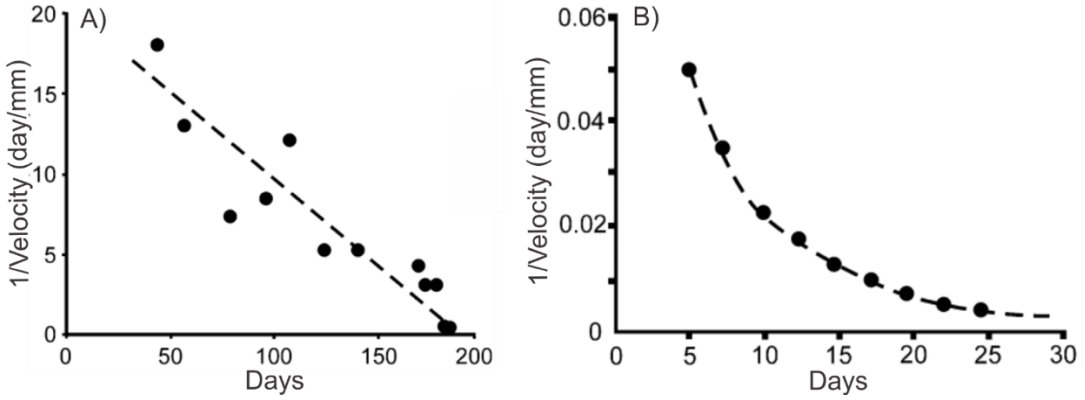

Figure 2.6: Two trends in 1/Velocity-time space observed by Petley et al. (2002). A) Linear trend, B) Asymptotic trend. Figure after Petley et al. (2002).

What is clear from the above discussion, is that landslides can move in a variety of ways, with past studies showing that site-specific characteristics play a major role in determining the behaviour (e.g. Allison & Brunsden, 1990; Carey et al., 2015; Massey et al., 2013; Petley et al., 2002). While slow movement types can cause damage to infrastructure, they often pose a limited threat to life. On the contrary, movement types that display rapid failure behaviours can pose an extreme risk to both infrastructure and life, and have historically been the most catastrophic. Consequently, understanding landslide movement type is imperative to hazard assessments. To fully understand these movements however, requires a comprehensive knowledge of the key mechanisms of deformation that are acting at the shear surface during failure; something commonly investigated using specialist laboratory testing.

2.5 Laboratory testing of rainfall-induced landslides

Complex mechanisms that act during shear surface development are often difficult and expensive to analyse in the field, and so are often investigated through the laboratory simulation of the complex hillslope environment (e.g. Carey et al., 2017; Ng & Petley, 2009; Wang & Sassa, 2003). Of relevance to this study, is laboratory testing that can investigate the mechanics of rainfall-induced landsliding, and specifically those techniques that can monitor and/or control PWP generation in a sample during the failure process; thus simulating the effects of rainfall and changing groundwater conditions.

Ng and Petley (2009) used a triaxial cell to carry out specialist pore-pressure reinflation (PPR) testing on rhyolite lava and tuff samples from Lantau Island, Hong Kong. The aim of the study was to investigate movement patterns in the material in response to changing pore pressure conditions. Ng and Petley (2009) carried out a

series of linear and stepped PPR tests using different rates obtained from past rainfall records. Results from the study identified that during rainfall-induced landsliding, the material can undergo three movement types during failure development (Figure 2.7).

Stage 1: Low rates of strain accumulation when mean effective stress levels are high.

Stage 2: As the mean effective stress decreases, periods of non-linear PWP increase cause pulses of variable increases in strain rate.

Stage 3: Rapid acceleration to failure when PWP increases to a sufficient level, suggested to be associated with the internal restructuring of the shear zone.

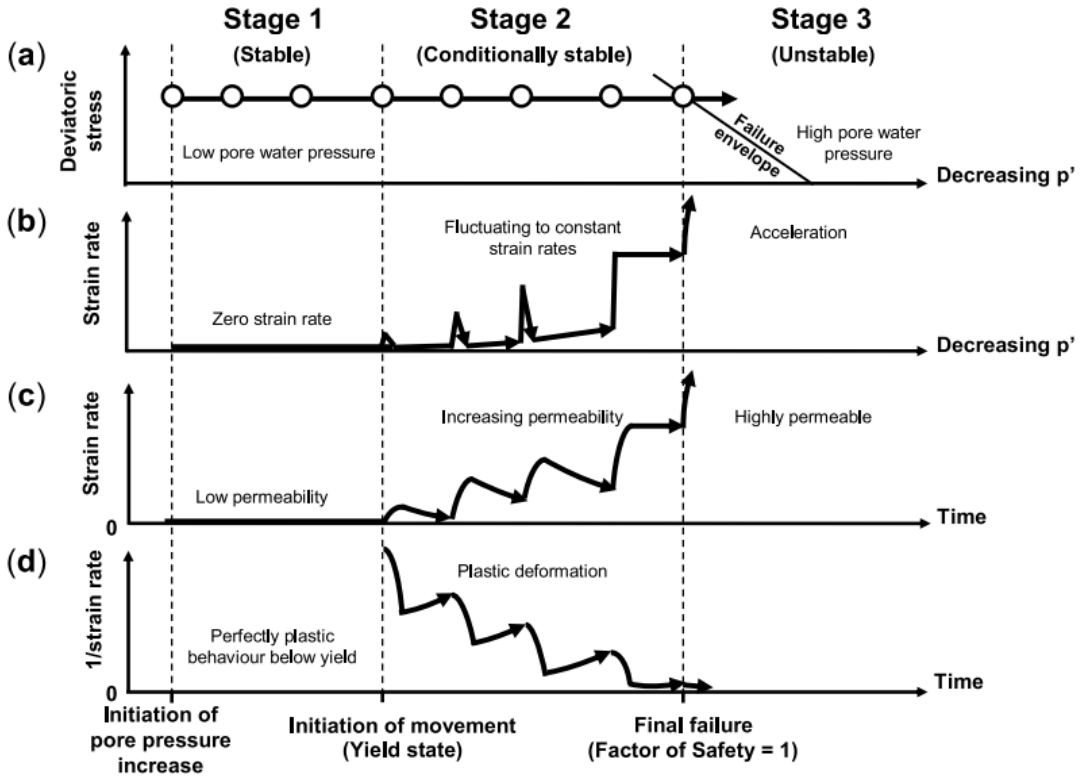

Figure 2.7: Three stages of rainfall-induced landslide movement in residual soils. Note circles indicate instantaneous periods of PWP increase. Figure from Ng and Petley (2009, p. 496).

One of the key outcomes of the study by Ng and Petley (2009) was that they were able to show that there is a time dependent component of the failure process. They demonstrated that rapid acceleration to failure can occur while PWPs are held constant, indicating that this acceleration is associated with the internal restructuring of the landslide mass (Figure 2.8). This behaviour has significant implications for rainfall thresholds that are derived for hazard assessments.

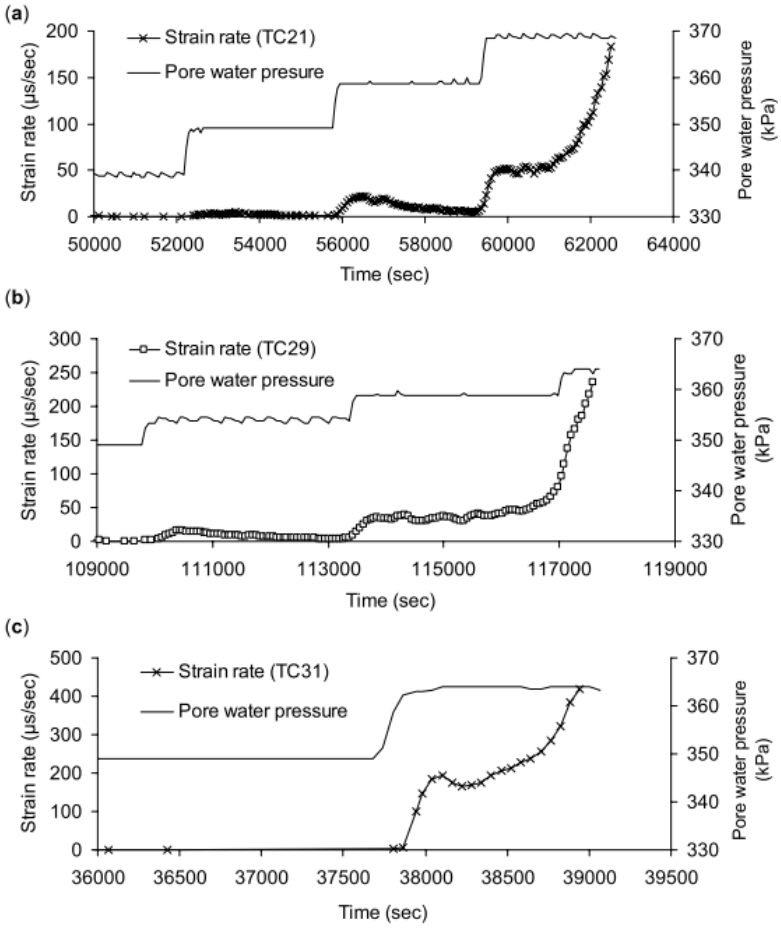

Figure 2.8: Plots showing axial strain and PWP against time that reveal a strong time component in the failure process. a), b) and c) show the results of three different samples. Figure from Ng and Petley (2009, p. 495).

Further to the study by Ng and Petley (2009), was the work carried out by Carey et al. (2016) that involved the laboratory simulation of slow landslide mechanisms. Carey et al. (2016) used a dynamic back-pressured shear box to better understand the relationship between ground movements and PWP in the Utiku landslide complex. Undisturbed samples were initially saturated and consolidated, before a given shear stress was applied to simulate the stress state of a landslide close to failure. The samples were then subjected to varying rates of both linear and stepped PWP increase, thereby replicating conditions of failure. Results from the study correlated well with results from the work of Ng and Petley (2009), as Carey et al. (2016) observed both slow movement when the PWP increase was enough to generate a marginally unstable state; and also accelerated movement when the effective normal stress decreased further due to a continued rise in PWP. Furthermore, results showed that the displacement rate slowed when the rate of increase in PWP reduced, a behaviour observed in other laboratory and field based studies of landslides (e.g. Allison &

Brunsden, 1990; Ng & Petley, 2009). This behaviour suggests that faster landslide movements are controlled not only by the amount of PWP generated, but also the rate in which it is generated. While the studies discussed above have investigated failure mechanisms in slow moving landslides, laboratory studies have also successfully investigated failure mechanisms in rapid moving landslides (e.g. Sassa et al., 2004; Take et al., 2004; Wang & Sassa, 2002).

Sassa et al. (2004) describe the development of a ring-shear device and its application to investigating a slide-triggered debris flow in Minamata, Japan that killed 15 people. The ring-shear apparatus was first used to investigate the initial failure mechanism of the slide, before being used to simulate the loading of a torrent deposit/soil layer that generated the debris flow. To simulate the original failure, initial stresses were applied to the sample in the apparatus before PWPs were gradually raised reflecting the heavy rainfall that fell prior to the failure. This test was undertaken in drained conditions, meaning that while PWP was controlled, water was free to move through the sample and out a drainage valve. This behaviour reflects the natural groundwater rise that would have occurred. Results from the test showed that once the stress path reached the failure envelope due to decreasing the effective normal stress (increasing PWP), shear resistance dropped rapidly, before stabilising at some value (Figure 2.9). Sassa et al. (2004) interpreted this behaviour as initial shear failure producing grain crushing along the shear surface, which then resulted in the generation of excess PWP and rapid failure. The excess PWP was not recorded however, as the transducer was located on the opened drainage valve, not the shear surface where excess pressure developed.

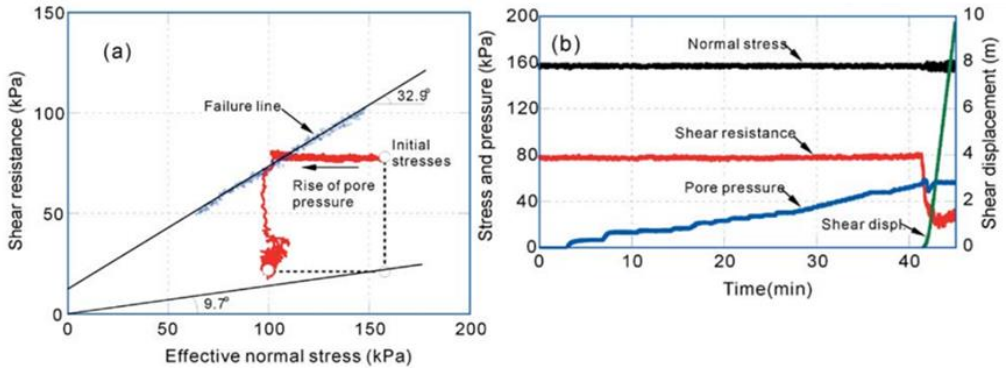

Figure 2.9: Results from the simulation of the original landslide at Minamata. Figure from Sassa et al. (2004, p. 14).

Following the initial test, Sassa et al. (2004) then investigated the rapid loading that generated the debris flow. This test involved gradually increasing the shear stress on

both tuff breccia and andesitic lava samples (as the torrent deposit was composed of both materials) under undrained conditions. Both tests revealed that only a small increase in shear stress, 18.5kPa in the case of the tuff, and 45.5kPa for the lava, was necessary to generate sufficiently high PWPs and subsequent failure (Figure 2.10). Through laboratory testing, Sassa et al. (2004) were able to establish that sliding-surface liquefaction triggered by rising groundwaters explained the initial slope failure, while the subsequent undrained loading of the torrent deposits by the initial landslide mass easily explained the debris-flow mobilisation.

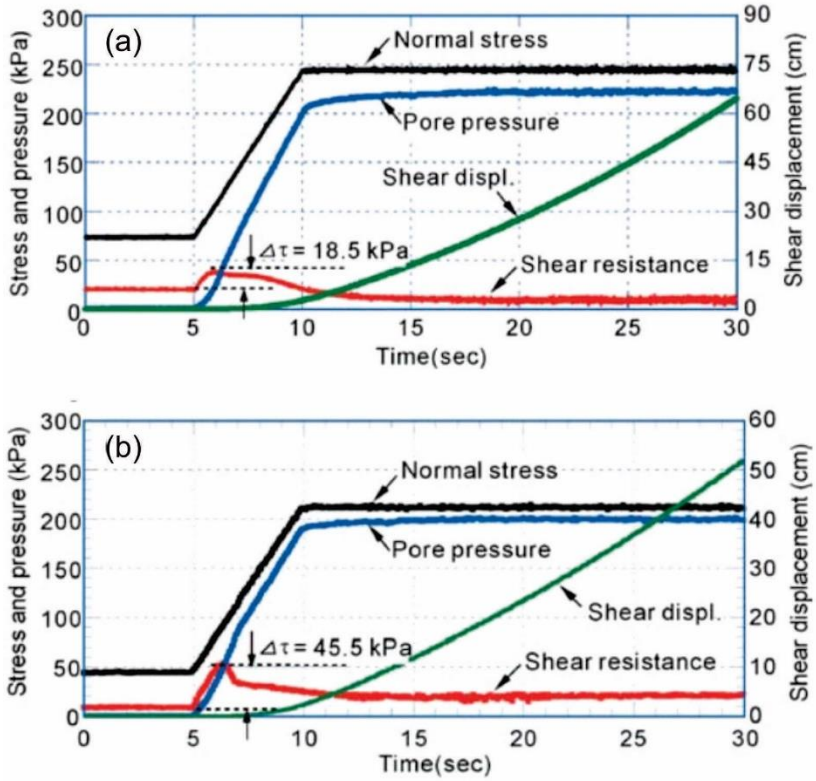

Figure 2.10: Results of undrained loading tests on a) tuff breccia, and b) andesitic lava at Minamata. Figure after Sassa et al. (2004).

It can be seen that laboratory based testing has been successfully used to investigate landslide failure mechanisms in various types of materials and slope failure. Importantly, this includes testing that is able simulate the complex pore-pressure conditions that arise from rainfall and/or changing groundwater conditions; scenarios that are responsible for a large portion of landslides worldwide. Results from laboratory testing, when used in combination with a knowledge of models of shear surface development, are able to better inform hazard assessments through an improved understanding of the processes acting during the development of failure. Furthermore, laboratory testing provides empirical relationships between stress and

strain for various failure scenarios, and it is these relationships that often form the basis for theoretical models of shear surface development.

2.6 Theoretical models of shear surface development

Different theoretical models aiming to explain progressive shear-surface development, as originally defined by Terzaghi (1950), have been proposed in order to gain greater insights into the hazard posed by landslides.

2.6.1 Bjerrum's model of progressive failure

Bjerrum (1967) was the first to attempt to explain the concept of progressive failure, albeit while conceding that the topic was one of the most challenging in soil mechanics. Bjerrum's conceptual model of progressive failure was based on the significant advances made by Skempton (1964), concerning the residual shear strength of over-consolidated clays. Skempton (1964) concluded that the progressive development of a shear-surface preceded landslides in over-consolidated clays, and that if sufficient time allowed the development of the shear surface in natural slopes, the residual strength of the material is the controlling factor of stability. Bjerrum (1967) pointed out that while Skempton's work made significant advances, further understanding of the mechanisms of progressive failure was needed.

For a detailed description of the complex model, see Bjerrum (1967) or Carey (2011).

Ultimately, Bjerrum (1967) was able to establish several requisite conditions for progressive failure to occur:

1. Some discontinuity must exist - either in the mass or at its boundary.
2. The development of shear stresses that exceed the peak shear strength of the clay must be possible.
3. Local differential strain in the shear zone that is adequate to strain the clay beyond failure is required for shear-surface advancement.
4. A significant and rapid reduction in the shear strength of the clay with strain must occur once the failure strength is mobilised.

The ultimate goal of Bjerrum (1967) was to stimulate discussion and interest in order to find solutions to the problem of concern. While his progressive shear-surface development model for over-consolidated clays undoubtedly achieved this, it is worth noting its limitations. Bjerrum's model provides an explanation for the progressive development of a linear shear surface resulting from toe unloading in a simple,

homogeneous slope; conditions which do not reflect the complexity of landslides observed around the world, as many failures occur on irregular shear surfaces or zones through heterogeneous materials. Also, while many failures do result from toe unloading processes such as river incision and anthropogenic cutting, other mechanisms of failure that are likely to result in different stress patterns than those described in Bjerrum's model, such as PWP changes are also known to exist (e.g. Wang & Sassa, 2003).

2.6.2 Simple slider block friction model

Helmstetter et al. (2004) proposed a power-law model that aims to explain the stability of progressive failure. Specifically, they provide a physical basis for explaining stable and unstable acceleration to failure behaviours observed in landslides (as discussed by Voight & Pariseau, 1978) using a simple slider block model coupled with a state-and-rate dependent friction law.

The model structure consists of a rigid block sliding down an inclined surface under the influence of gravity, where basal friction regulates acceleration (Helmstetter et al., 2004). The authors identify that within such a conceptual structure, landsliding behaviour is influenced by three factors; 1) block behaviour dynamics, 2) dynamical interactions between the block and substratum, and 3) the history of any external loading (Helmstetter et al., 2004).

As a function of initial conditions and the frictional law used, the model produced exhibited four different sliding regimes (Figure 2.11):

1) Velocity strengthening - stable/constant acceleration
2) Velocity weakening - unstable acceleration
3) Velocity strengthening - deceleration
4) Velocity weakening - deceleration

The model assumes that it is the materials properties that control which sliding regime occurs, as these properties are embedded in key parameters used and/or the initial conditions set.

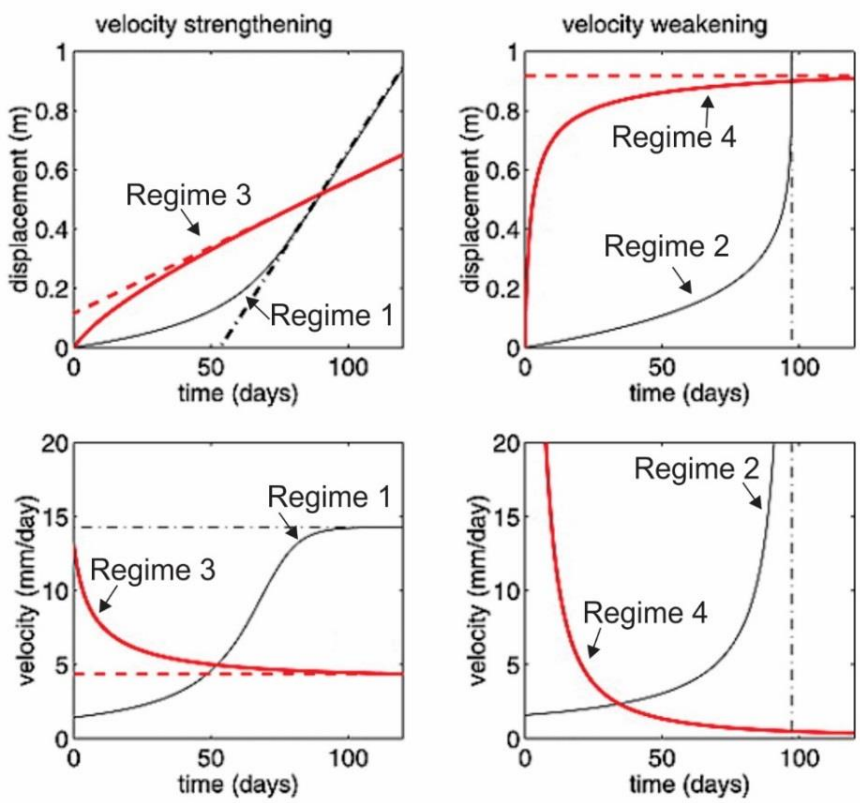

Figure 2.11: Graphic representation of the sliding regimes proposed by Helmstetter et al. (2004). Red lines represent decelerating regimes and black lines represent accelerating regimes, dashed lines represent critical values. Figure after Helmstetter et al. (2004).

The model was used to quantitatively analyse the displacement history of two historic landslides, the Vaiont and the La Clapière landslides, ultimately finding it correlates well with observations from both. They established that the Vaiont landslide, which was attributed to failure in clays bands within a limestone mass, and was characterised by devastating slope acceleration was analogous to the unstable acceleration regime (regime 2). And in the case of the La Clapière landslide, which was a failure in weak gneiss bedrock, characterised by peak acceleration and subsequent stabilisation, was found to resemble the stable acceleration regime of the model (regime 1) (Helmstetter et al., 2004).

While the slider block model proposed by Helmstetter et al. (2004) provided an initial step towards a greater understanding of sliding regimes and their potential prediction, its simplicity results in some significant limitations. Of the limitations, the inability to model pore-pressure variations at the shear surface is one of the largest.

2.6.3 Dilatancy feedback model

Iverson (2005) incorporates the role of pore water as a first-order control on landslide movement to better understand the transition from stable to unstable motion, due to the

implications it has for the downslope hazard. The critical difference from the model proposed by Helmstetter et al. (2004) is the inclusion of a mechanical feedback between displacement and shear zone dilation or contraction by Iverson (2005). This feedback in turn feeds changes in basal pore-water pressure and ultimately regulates basal friction.

The model itself is a slider block model where landslide displacement is governed by Newton's second law and is solely resisted by basal Coulomb friction (schematically shown in Figure 2.12) (Iverson, 2005). Iverson's model is a development of the sliding-consolidation model proposed by Hutchinson (1986), which similarly involves the regulation of a sliding block by pore-water pressure, with the key difference being the feedback mechanism included by Iverson (2005).

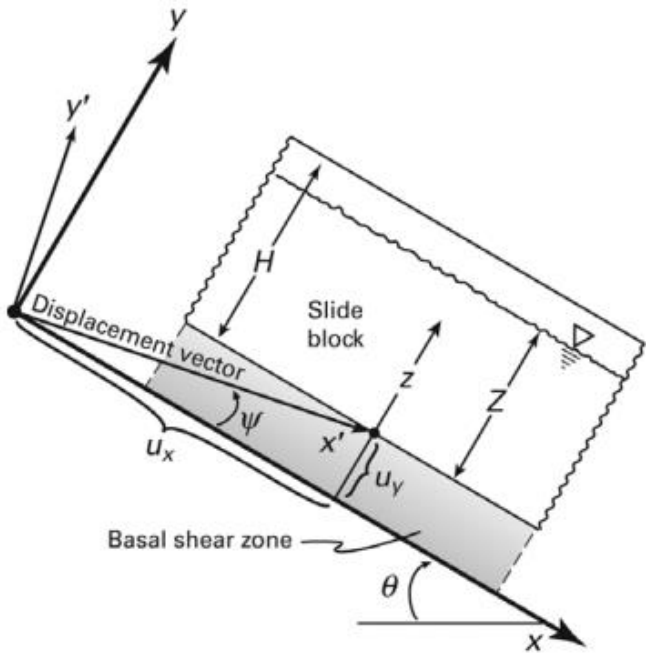

Figure 2.12: Schematic diagram of Iverson's dilatancy feedback slider block model. Figure from Iverson (2005, p. 2).

Iverson found that dilatant or contractive shearing in a saturated basal shear zone can lead to an acceleration or stabilisation of landslide motion. This is the product of the feedback between landslide displacement, shear zone volume change, pore-water pressure change and the consequent effect on Coulomb friction (Iverson, 2005). Iverson established that the aforementioned feedback depends on the dimensionless parameter α, which itself depends on the dilatancy angle (Ψ) that describes a materials propensity for shear-zone volume change and the inherent timescales for pore-water pressure generation and diffusion (Iverson, 2005). Where α is found to be small, which

is typical of sand-rich material, shear-zone contraction can lead to a transition from stable motion to unstable acceleration. On the other hand, if α is large, typical of clay-rich material, dilation of the shear zone can lead to a stabilisation of motion (Iverson, 2005). Ultimately, Iverson suggests that it is the physical properties of a material and the historic forcing by rainfall that influence the evolution of a landslide.

This model proposed by Iverson (2005) addresses the significant role pore-water pressure plays in landslide motion and evolution, provides an explanation for movement behaviours observed in some landslides and showcases how it is the materials properties that determines types of failure behaviours. However, like Helmstetter et al. (2004), it does not account for all complexities that have been observed in landslide motion, such as non-linear relationships between pore-water pressure and displacement.

2.6.4 Micro-cracking and shear surface development model

Petley et al. (2005) proposed a conceptual model for the development of a progressive, first-time failure in cohesive material landslides, that unlike the work by Helmstetter et al. (2004) and Iverson (2005), incorporated laboratory based testing. In the proposed model, four stages of failure development exist (Figure 2.13).

Petley et al. (2005) suggest that the initial development of a shear-zone occurs when some critical FoS value is reached in response to fluctuations (in particular a rise) in PWP. At this stage, micro-crack formation begins, and a small amount of creep-like displacement takes place as a result (Figure 2.13 A). While formation of the micro-cracks may have the effect of weakening the slope and reducing the FoS slightly, the slope is principally stable and any subsequent fall in PWP will cause the FoS to increase again. The second stage (Figure 2.13 B) would be termed secondary creep according to the classification by Varnes (1978). It begins when a second FoS threshold is met, where the coalescence of micro-cracks occurs and shear-surface development begins. A complete failure surface is not yet developed at this stage, but progressive development of the shear surface results in small amounts of displacement. The third stage of development is characterised by continued shear surface growth, leading to a concentration of stress, accelerated movement, and a linear trend in inverse velocity-time space during tertiary creep (Figure 2.13 C). PWP becomes increasingly unimportant during this stage, as continued movement is regulated by propagation of the shear surface, however, it is possible for a significant reduction in

PWP to arrest movement. Stage four is when complete failure occurs as the shear surface develops completely as the FoS reaches unity i.e. the shear forces are equal to the resisting forces (Figure 2.13 D).

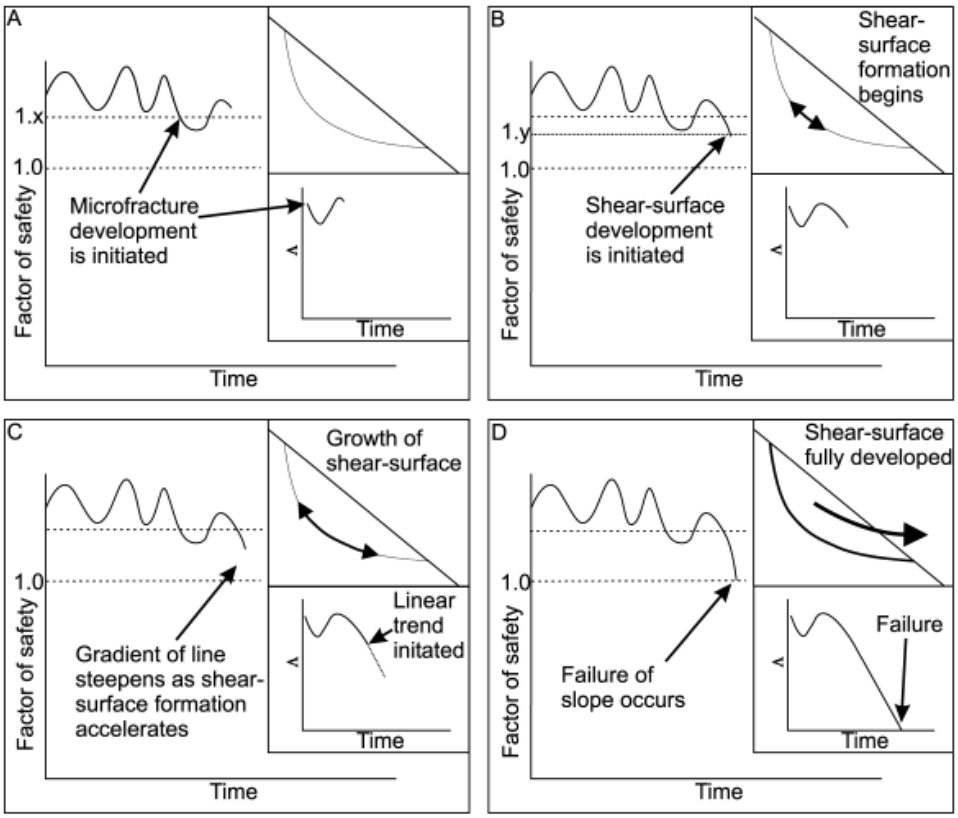

Figure 2.13: Four stages of failure development in the conceptual model proposed by Petley et al. (2005). Figure from Petley et al. (2005).

This model, proposed by Petley et al. (2005), provides an explanation for brittle failure in cohesive materials, addresses the development of failure when the FoS is above unity, and explains a linear trend in inverse velocity-time space during tertiary creep. However, whilst the model does provide explanations for some observed phenomena, just like the other models reviewed, it is unable to account for the complexities observed in other failures.

What is clearly evident from the several models reviewed here, is that each model is able to explain some phenomena well, but cannot account for the observed behaviours of all landslides. Each model is largely dependent on the type of landslide, the materials involved, and the mechanisms of deformation acting at the shear-surface; characteristics which vary between landslides.

One potentially devastating failure behaviour the models described above do not seem to account for is that of rapid flow-slides. Rapid flow-slides, previously discussed as a

behaviour observed in fill slope failures, can be catastrophic due to their rapid movement and fluid-like behaviour; a behaviour widely hypothesised to be caused by liquefaction (e.g. Bishop, 1973; Take et al., 2004; Wang & Sassa, 2003).

2.7 Liquefaction

Liquefaction is the process by which a soil body loses a large proportion of its shear strength in response to a rapid rise in PWP. This occurs as the result of excess strain collapsing the soil structure (Figure 2.14 A), which instigates an increase in PWPs and a subsequent loss of strength in an undrained setting (Hungr, 2007). The most common form of liquefaction, as defined above, can be triggered by static factors such as rainfall and snowmelt, or by dynamic factors such as an earthquake (Wang & Sassa, 2003). Whilst liquefaction most commonly occurs via the process discussed above, another type of liquefaction, termed sliding-surface liquefaction has also been identified (Okada et al., 2000; Sassa et al., 1996).

Sliding-surface liquefaction develops following an initial failure, unlike the liquefaction mechanism described above. The Initial failure results in displacement and shearing along a shear zone, causing subsequent grain-crushing in the shear region (Figure 2.14 B). This textural change results in contraction (densification) of the shear zone and a subsequent rise in in PWP; ultimately leading to liquefaction occurring along the newly densified layer (Hungr, 2007). Importantly, grain-crushing is the only requirement for this behaviour, and does not require a given density state (Sassa, 2000).

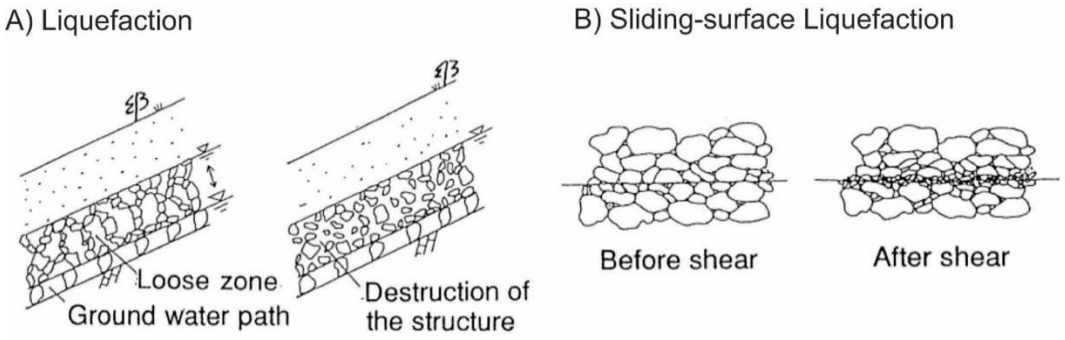

Figure 2.14: Liquefaction and sliding-surface liquefaction. Figure after Sassa et al. (1996).

Although failure via liquefaction can occur through two differing mechanisms, the characteristic failure behaviour that results from both mechanisms is the same. Landslides triggered by liquefaction are generally characterised by fluidised motion; with relatively higher rates of movement and longer run-out distances than most other

types of landslides (Huang et al., 2012; Wang & Sassa, 2003). Critically, it is the implications this behaviour has on the prospective hazard that needs to be appreciated; as flow-like landslides have the potential to be devastating.

One hazard in particular that should be appreciated and investigated is that loosely compacted fill slopes seem to be pre-disposed to failing through liquefaction. As discussed earlier catastrophic examples of fluidised failures in fill slopes have been seen globally (e.g. Bishop, 1973; Take et al., 2004), and importantly in the context of this research, several significant failures have been observed in Wellington, New Zealand over the past decade.

3 The susceptibility of fill slopes in Wellington, New Zealand

3.1 Regional setting

The Wellington region is a physically dynamic environment located on the southwest coast of the North Island of New Zealand. It is bounded to the east by the Rimutaka Range, south by the Cook Strait, west by the Tasman Sea and to the north by the Tararua Range (Figure 3.1). 'The Wellington Region' refers to Wellington City and the surrounding urban centres as displayed in Figure 3.1. The climatic, geologic and geomorphic setting have created an environment susceptible to landsliding, and has subsequently become an area of significant landslide activity and research (e.g. Crozier & Glade, 2005; Eyles et al., 1978; Glade, 1997, 1998).

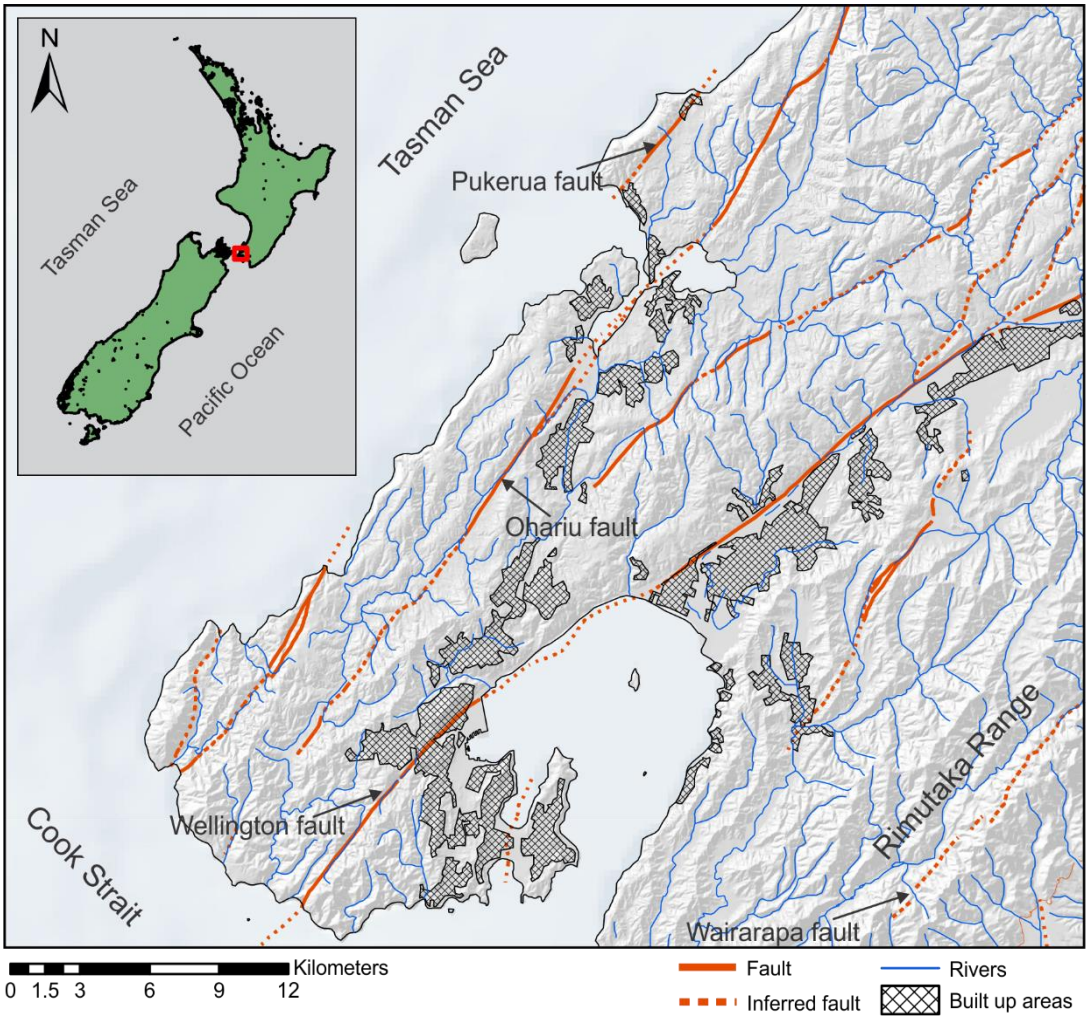

Figure 3.1: Image of the wider Wellington Region and key features of the area. Inset image (top left) highlights the location of the Wellington region in New Zealand (red box).

3.1.1 Geology

The Wellington Region is founded on bedrock of the Torlesse Subgroup, comprising alternating layers of indurated sandstone (greywacke) and mudstone (argillite) of Mesozoic age (Begg & Johnston, 2000). These rocks have been significantly deformed and tectonically fractured by the faulting and folding of the northeast trending Ohariu and Wellington faults that run through the region, as well as the nearby Wairarapa and Pukerua faults that lie to the east and west respectively. Unconsolidated sediments of late Pleistocene and Holocene age, including alluvium, fill and aeolian sand deposits are also sparsely present in valleys, river basins, sand dunes, reclaimed areas and fills (Begg & Johnston, 2000; Khan et al., 2012).

The broad structure of the region is shaped by the westward tilting fault blocks formed by varying uplift rates along the major northeast-southwest striking faults (Figure 3.1). Faulted synclines and anticlines that strike north-south have also developed as a result of frictional drag on fault boundaries, in particular the Wellington fault, forming key landforms such as the Wellington Harbour, Lower Hutt and Upper Hutt basins (Eyles & McConchie, 1992). These underlying geological formations that mould the region have continuously been heavily modified by climatic processes to reveal the landscape observed today.

3.1.2 Climate

The climate of the Wellington region is spatially and temporally variable, with the presence of the Cook Strait to the south and local topography playing important modulating roles. In general, the climate of the region reflects the interplay of the general westerlies and interposed anticyclones with the rugged local topography (Chappell, 2014).

Precipitation in the region is highly variable due to the topographical influence on airflow, ranging from 2000mm/yr in the nearby Rimutaka and Tararua Ranges, to 1000mm/yr at the airport in Wellington City (Figure 3.2). Average monthly rainfall is consistently above 58mm throughout the year, with winter months generally receiving the most at ~100mm/month (Table 3.1). Extreme weather events and associated periods of heavy rainfall are also a feature of the region, where high winds and heavy rain often result in flooding, slips and other hazards leading to significant clean-up costs (Chappell, 2014; Tomlinson & Dyke, 1977).

Table 3.1: Average precipitation totals and wet days at the airport in Wellington City. Table from Chappell (2014).

	Jan	Feb	Mar	Apr	May	Jun	Jul	Aug	Sep	Oct	Nov	Dec	Ann
Ave Precip (mm)	58	61	67	68	86	101	113	93	75	95	75	65	957
Wet days (> 1mm)	6	7	7	8	9	12	12	12	10	11	9	8	110

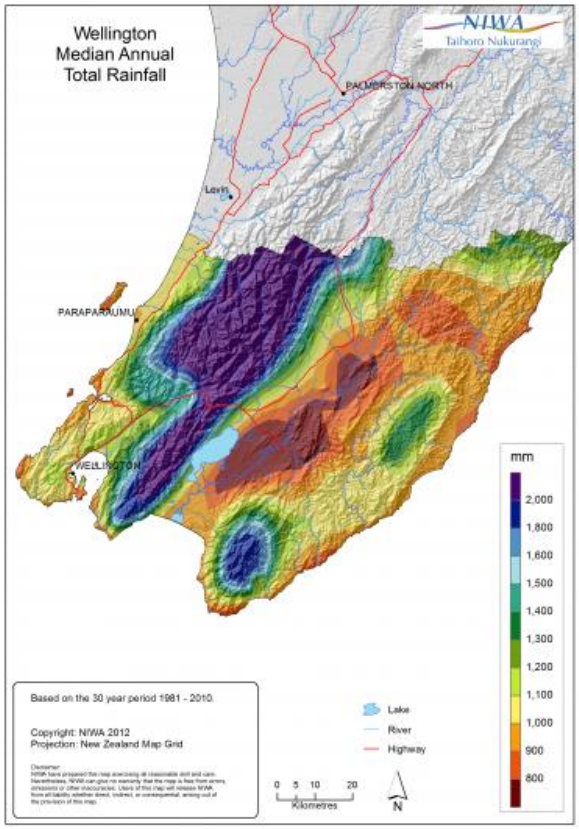

Figure 3.2: Median annual rainfall in the Wellington region between 1981 and 2010. Figure from Chappell (2014).

Wellington has a temperate climate, with temperatures relatively evenly spread year round due to the proximity of the ocean and windiness of the region. Summer months are characterised by mean average temperatures of approximately 16-18°C, while winter temperatures are typically around 9-11°C (Figure 3.3). Figure 3.3 also highlights the variability in temperatures experienced, with mean monthly minimums reaching 1-2°C during winter, and mean monthly maximums reaching 26-27°C in summer months. Temperatures are spatially variable across the region, with altitude, attitude, and proximity to the coast being the major controlling factors (Chappell, 2014).

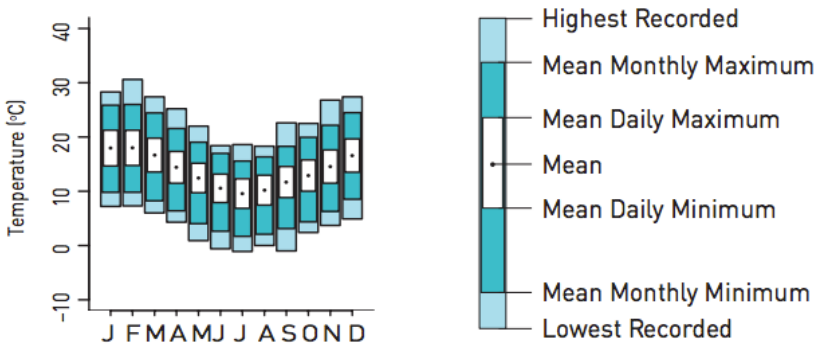

Figure 3.3: Wellington City average monthly air temperature variations. Figure from Chappell (2014, p. 25).

The climatic conditions described above have acted (and act) to shape the underlying geology, with climate-driven processes playing a major role in producing the geomorphic landscape we observe today (Eyles & McConchie, 1992).

3.1.3 Geomorphology

The geomorphology of the Wellington region reflects the relationship between tectonism and ongoing geomorphic adjustment that has, and continues to, occur. This interaction has sculpted a topography that is generally characterised by moderate to steep sloping hillsides and significant fluvial dissection of the landscape (Glade, 1997). One of the more recognisable features of the region is the so termed 'K' surface, which refers to the western areas characterised by uplifted surfaces of low relief and steep side slopes, as identified by Cotton (1957).

The substantial tectonism in the region is reflected in the landscape with geomorphic features such as ridges and basins striking northeast-southwest or north-south following the trend of the major faults and their associated structures. Drainage in the region is also largely fault-controlled, as highlight by the orientation of major valleys and rivers such as the Hutt and Ohariu (Eyles & McConchie, 1992). Moderate to steep hillslopes are a key feature of the region, largely resulting from the combination of tectonic uplift and climate-driven erosional processes. Additionally, anthropogenic modification has played a significant role in modifying the urban geomorphology through cut and fill processes, resulting in the over-steepening of natural slopes and infilling of small valleys (Figure 3.4) (Eyles & McConchie, 1992).

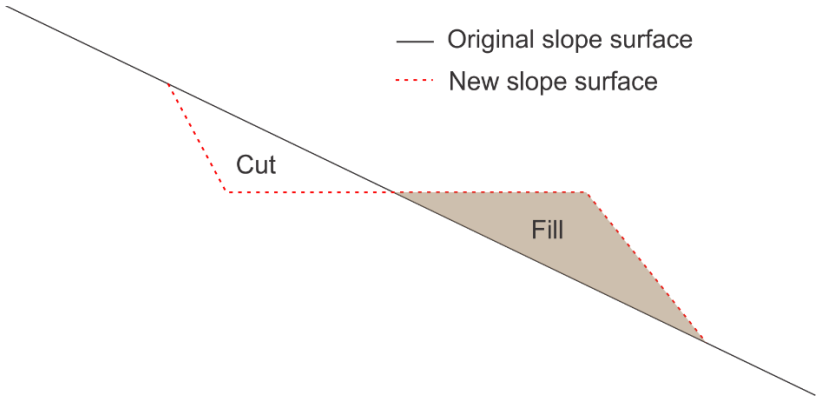

Figure 3.4: Basic schematic of a cut and fill slope.

While the region has a characteristic geomorphology shaped by interacting processes over millions of years, it is constantly in a state of ongoing adjustment (Eyles & McConchie, 1992). One of the key processes that plays a significant role in this constant adjustment is mass wasting (e.g. Eyles et al., 1978; Eyles & McConchie, 1992; Glade, 1997).

3.2 Historical landslide activity

Landslides have long played a major role in sculpting the geomorphic environment of the Wellington Region, with early observations of earthquake and rainfall induced landslides dating back to 1848 and 1881 respectively (Eyles & McConchie, 1992; Glade, 1997). This susceptibility to landsliding is largely the result of the regional setting described previously, which predisposes the landscape to such mass wasting events. Major events in the region, characterised by spatially extensive and numerous failures, occur on average twice a year (Grant et al., 2005). Although past events (since at least 1997) have not resulted in any deaths or injuries, they have come at a substantial cost to the economy. Seven significant rainfall events between 1998 and 2005 resulted in 792 insurance claims being paid a total $5,146,000 for damages caused by landsliding (Grant et al., 2005). While seismicity and anthropogenic processes account for some of the landsliding observed in the Wellington Region, evidence suggests that heavy and/or prolonged rainfall is the most prevalent triggering mechanism (Eyles et al., 1978; Eyles & McConchie, 1992).

Between 2000 and 2010, at least 238 of the 323 (73.7%) landslides in the Wellington Region recorded by the National Landslide Database were triggered by rainfall (GNS, 2018). More specifically, a study investigating an unusually wet year as well as a singular event by Eyles et al. (1978) revealed in detail the enormous impact rainfall

can have. 1974 recorded one of the highest annual rainfall total in Wellington, with 1495-2080mm recorded at rainfall stations across the city, whilst several other rainfall records also occurred, including highest monthly totals, wettest four month period and most wet days (Eyles et al., 1978). Field work undertaken by Eyles et al. (1978) captured the true impact of rainfall that year, identifying a total of 1149 landslips in the region (Figure 3.5). Furthermore, a single storm on the 20th of December 1976 was similarly destructive, with Eyles et al. (1978) identifying 550 landslips in Wellington City as a result of the event, which was characterised by rainfall totals varying from 71 to 300mm (Tomlinson & Dyke, 1977). Although it is rainfall and other triggers that cause landsliding, ongoing anthropogenic modification may have exacerbated the susceptibility of many slopes to failure (Eyles and McConchie, 1992).

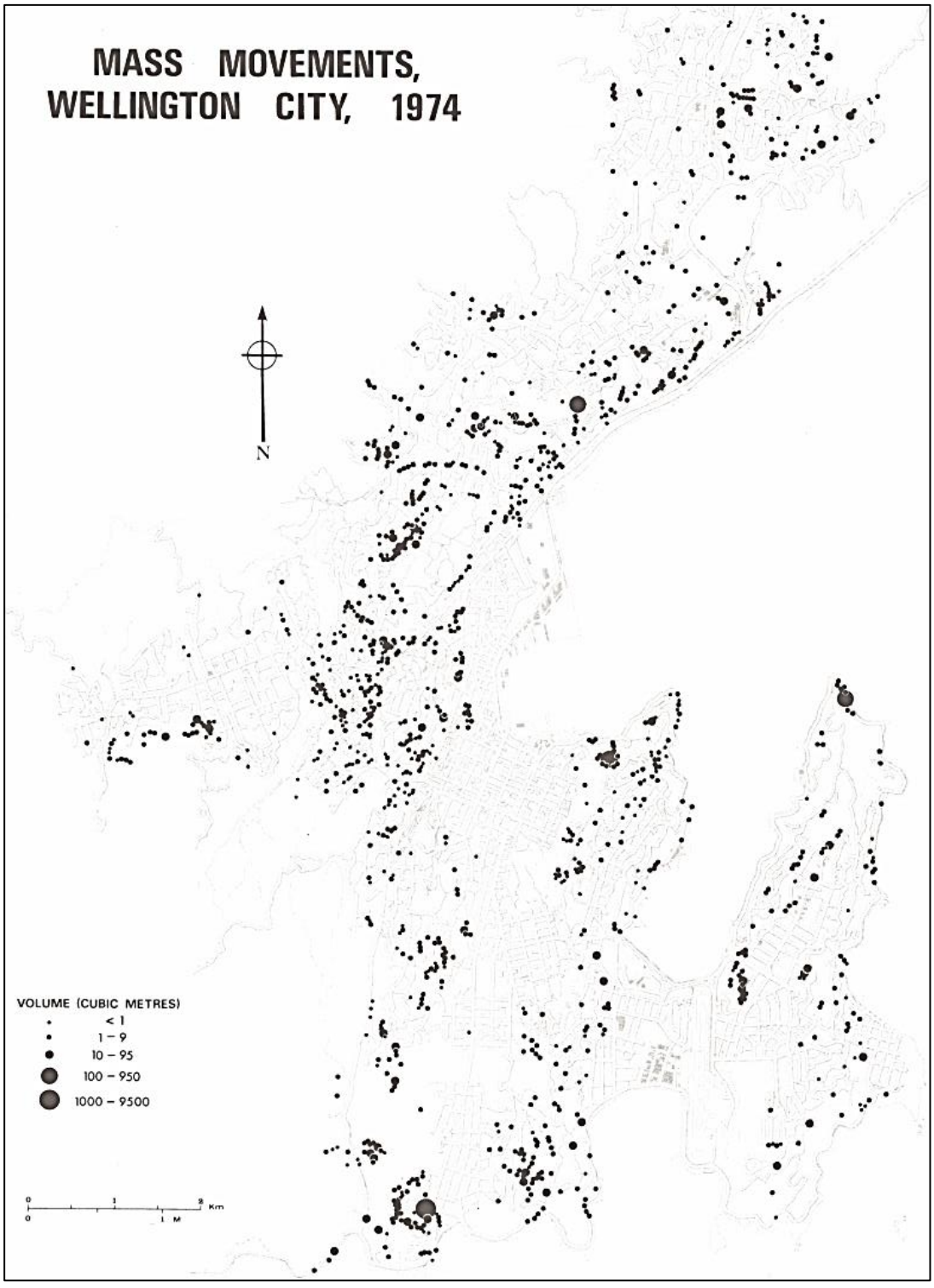

Figure 3.5: Landslides in Wellington during 1974. Figure from Eyles et al. (1978, p. 5).

Of the 1149 landslides identified by Eyles et al. (1978) in 1974, only two occurred in natural slopes, with the rest taking place on road cuts and various fills. Adding to this, 70% of the landslides identified during the 1976 storm also occurred in cut and fill slopes (Eyles et al., 1978). Although many of the failures on anthropogenic slopes are only minor slumps and slips, there have been several significant failures in the

Wellington Region since 2006 that suggest some fill slopes in particular may pose a considerable hazard. Explicitly, these failures are concerning because they displayed fluidised failure behaviours analogous to devastating fill slope failures observed globally (discussed in Section 1.1).

In 2006, a large landslide estimated to have involved approximately 1500-2000m^3 of material occurred in a fill slope after ~52mm of rainfall fell over a 48 hour period in the Lower Hutt suburb of Kelson (Hancox et al., 2007). Luckily, no homes were destroyed by this event, however, several were left lurching only metres from disaster with one having to be demolished as a result (Figure 3.6). Investigations into the landslide by the local council laid blame on the poor construction of the fill in the 1970's, and that the presence of a decomposed layer of vegetation at the base of the landslide contributed to failure (Hancox et al., 2007).

On the 1st of June 2013, at least 90 people had to be evacuated from their homes as a large fill slope failure undermined two houses and threatened several more on Priscilla Crescent in the Wellington City suburb of Kingston (Figure 3.6). This landslide involved ~50,000m^3 of material producing a run-out approximately 150m long and 40m wide, and was observed by residents to fail over a period of minutes displaying highly fluidised motion (Boyer & Daly, 2013; Duff, 2013). While it is still unclear exactly what caused the failure, the surface ponding of water and fluidised nature of the event indicate the landslide mass was highly saturated, strongly suggesting that changing pore pressure conditions were responsible for failure.

Most recently, on the 6th of April 2017, a second large fill slope landslide occurred in the Wellington City suburb of Kingston (Figure 3.6). This landslide occurred on Halifax Street, less than 200m from the Priscilla Crescent failure. Heavy rainfall triggered the Halifax Street landslide, as fragments of an ex-tropical cyclone passed across the northern parts of New Zealand, with over 100mm of rainfall falling in the three days prior to the failure (NIWA, n.d.). The size of the landslide was estimated to be up to three times greater than that of the Priscilla Crescent failure (Hunt & George, 2017), and it exhibited very similar fluidised failure characteristics.

An analysis of the geomorphology and behaviour of the three landslide events identifies important similarities and reveals crucial failure information. All three events were characterised by a steep head-scarps, moderate-to-low angle runouts, and rapid, fluidised motion (Figure 3.6). In the case of the two failures in Kingston, lobe deposits

at the end of the runout were also present, while in the case of the Kelson event, no image/information was found to identify the presence or lack of. Furthermore, all three failures took place in gully-head fills, typified by convergent geomorphic hollows (Figure 3.6). This information suggests all three landslides are best classified as debris flow-slides using the scheme proposed by Hungr et al. (2014), while also indicating important information about soil conditions prior to failure and controls on landslide motion.

The location of the landslides in topographic hollows is important, as the convergent nature of the hillslopes act to concentrate groundwater flow and drainage from rainfall (Fernandes et al., 2004; Montgomery & Dietrich, 1994). This suggests that the sites of the three fill slope failures may have had relatively high permanent water tables, or that during rainfall, the concentration of drainage would have allowed saturated conditions to readily develop. Additionally, another important observation was the moderate (Kelson failure) to low (both Kingston failures) angle runouts, and subsequent high mobility of the landslides. In particular, the low runout angles of both the Kingston failures suggests that the finer sediments are having a dominant control on landslide behaviour, and not the gravel and cobble sized particles present. This is because the high mobility of the landslides implies that the finer sediments may act to sustain high pore-water pressures following failure (Iverson et al., 2015; Legros, 2002), allowing the landslides to display fluidised, highly-mobile runouts. These interpretations suggest two key features of failure in the fill slopes: 1) saturated soil conditions were likely present, and 2) the fine grained sediments have a significant control of slope failure behaviour.

It is clear that the Wellington Region is an active environment predisposed to slope instability, where rainfall-induced landslides are recorded annually. Wellington's anthropogenic slopes are of key interest as a series of failures since 2006 suggests that some engineered fill slopes may be susceptible to fluidised failure with long runout during rainstorms. These failure types present a significant hazard, but to date little laboratory-based research has been conducted to understand their failure mechanisms.

Figure 3.6: Geomorphic analysis of three fluidised Wellington fill slope failures. Sources: 2) Hunt and George (2017), 5) Boyer and Daly (2013), 8) & 9) Hancox et al. (2007).

4 Methodology

The methods employed during this research were chosen to better understand the failure behaviour of fill material and specifically to carry out the aims of the study outlined in Section 1.3; they can be summarised as follows:

1. Sample collection (Section 4.1)
2. Physical property analysis (Section 4.2)
3. Specialist dynamic back-pressured shear box testing (Section 4.3)

4.1 Sample collection

Both disturbed and undisturbed samples of the engineered fill material were collected from the location of the 2013 Priscilla Crescent landslide using standard sampling techniques. Sampling of fill material only took place at the Priscilla Crescent site as access was permitted by the Wellington City Council, however, this material is likely representative of fill in the region, which is generally composed of Torlesse greywacke aggregate.

Two undisturbed block samples, which maintain the in-situ properties of the material, were taken from the true left and true right of the landslide head scarp. This was achieved by first creating a rectangular exposure, and then slowly chiselling downward to expose four sides. A plastic container was then placed over the protruding block, and then the bottom plane was chiselled away until the block could be removed freely. Once the blocks were removed they were handled carefully and wrapped tightly in cling-film to prevent any degradation and desiccation occurring. Two disturbed samples, which do not maintain the in-situ properties of the material were also collected in sealed plastic bulk bags to maintain the natural moisture content.

The samples were then transported to GNS Science in Wellington, where they were stored in a climate controlled chamber to maintain the in-situ properties of the materials collected. Subsequent testing and preparation occurred at GNS Science and Victoria University of Wellington.

4.2 Physical property analyses

A suite of conventional soil classification tests were undertaken on the engineered fill material in order to determine the basic physical properties of the material. The tests included particle size distribution, moisture content, loss on ignition, density and

Atterberg limit tests. These tests determine the fundamental properties of the material that may help explain why the material exhibits the failure mechanisms and behaviours it does.

4.2.1 Particle size distribution

A complete particle size distribution (PSD) was obtained through standard dry-sieving techniques using steel sediment sieves. An undisturbed sample was dried in an oven to remove any moisture to enable the dry sieving. This sample was then sieved into >19, 19-9.5, 9.5-4.75, 4.75-0.425, <0.425mm particle size ranges. A pestle was needed to disaggregate material that clumped during drying, however, care was taken to ensure no individual particles were crushed. The particle size fractions were then weighed, and the weight percentage of each size range was calculated to identify to complete PSD.

A more detailed PSD for the fine fraction (<2mm) of the material was also determined using a SediGraph 5000 laser particle sizer (LPS). An undisturbed sample was dried, disaggregated and sieved to obtain the portion of sample <2mm. Four 5g samples were then obtained using a sample splitter to ensure a true PSD representation. A 0.5g/L Calgon solution was added to the samples before they were then placed in an ultrasonic tank for 30 minutes prior to being run through the LPS to ensure the material was completely disaggregated. The four samples were then run through the LPS, and an average across the obtained PSDs was determined.

4.2.2 Moisture content

Undisturbed samples that retained the in-situ characteristics of the fill material were used to calculate the moisture content of the material. This was achieved by comparing the weights of samples that had been fired in a furnace (W_d) at 110°C for ~24 hours to remove any moisture from the original weight of the samples (W_m). An average across four samples was taken, where the moisture content was equal to: $(W_m - W_d)/ W_m$

4.2.3 Loss on ignition

The fraction of organic content in the material was identified using loss on ignition testing methods. Eight pre-weighed samples were ignited in a furnace at high temperatures (400°C) for three hours causing the organic material to combust. The post-ignition weight (W_p) was then compared to the pre-ignition weight (W_i) to obtain

the fraction of organic content present, where the fraction of organic content was equal to $(W_i - W_p)/ W_i$. An average across the eight samples was taken.

4.2.4 Density

Due to the irregular shape of the undisturbed samples (Figure 4.1), the bulk density of the material was obtained using unconventional methods. Archimedes' principle was used to obtain the volume of three undisturbed samples as they were wrapped in cling-film (to prevent the absorption of water) and then submerged in water. Using Archimedes' principle the volume and the density of the material was estimated as follows:

$$m_3 = m_2 - V_w \rho_w \qquad \text{(using Archimedes' principle)}$$

$$V_{specimen} = \frac{m_2 - m_3}{\rho_w} - \frac{m_2 - m_1}{G_\rho} \qquad \text{(finding the volume of the specimen)}$$

$$\rho = \frac{m_1}{V_{specimen}} \qquad \text{(finding the bulk density)}$$

Where: m_1 = specimen mass, m_2 = specimen + cling film mass, m_3 = apparent immersed mass, V_w = volume of displaced water, ρ_w = density of water, $V_{specimen}$ = volume of the specimen, G_ρ = cling film density, ρ = bulk density, and w = water content.

From the bulk density, the dry density could then be calculated as follows:

$$\rho_d = \frac{\rho}{1 + w}$$

Figure 4.1: In-tact block sample taken from Priscilla Crescent, Wellington.

4.2.5 Atterberg limits

Atterberg limits are a measure of the critical water content of a soil that define boundaries of behaviour change (Selby, 1993). The liquid and plastic limits, defined as the moisture content at which the material begins to behave as a liquid and plastic respectively, were obtained for the fine portion (<425µm) of the material.

Liquid limit

The liquid limit of the material was determined using a Casagrande apparatus following standard procedures (e.g. Das, 2013; Vickers, 1978). The Casagrande device (shown schematically in Figure 4.2 a) is primarily made up of a brass cup and a rubber base. The cup can be raised and dropped repeatedly onto the rubber base by a cam operated using a crank on the side of the device.

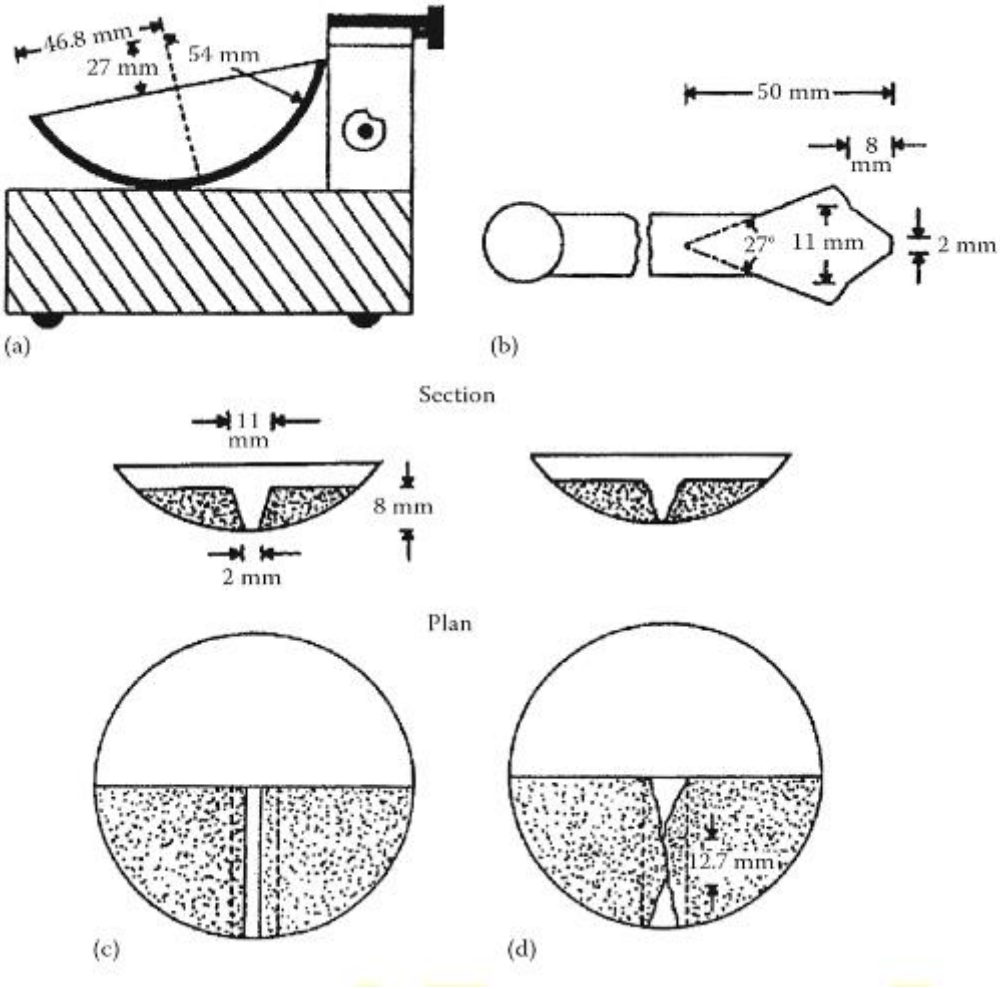

Figure 4.2: Schematic diagram of the Casagrande device (a), a grooving tool (b), sample at the beginning of a test (c) and at the end (d). Figure from Das (2013).

To perform the test, a sample was dried, disaggregated using a pestle, and then sieved so only material <425µm was used in the test. The sample was then mixed with water, forming a paste, which is then placed inside the brass cup. Using a grooving tool (Figure 4.2 b), a groove was cut in the sample along the diameter of the cup from the cam to produce the schematic in Figure 4.2 c. The crank was then turned, lifting the cup and dropping it onto the rubber base (referred to as a blow). The crank was turned at a constant rate until the groove in the bottom of the sample was closed (Figure 4.2 d), and the number of blows was recorded. This process was repeated three times with the sample at varying moisture contents. The liquid limit, by definition (e.g. Das, 2013), was then taken as the moisture content (in percent) at which it takes 25 blows of the cup to close the groove in the cup, which was obtained based on the trend-line (commonly referred to as a flow curve) fitted to the graph shown in Appendix A.

Plastic limit

The plastic limit was again obtained following standard procedures (e.g. Das, 2013; Vickers, 1978). As in the liquid limit testing, the material was dried, disaggregated and sieved so only material <425µm was used. The sample was then mixed with water until it was sufficiently plastic to be rolled into a ball. The ball was then split into three parts, and the following was undertaken for each:

The sample was rolled on a glass plate using fingertips forming a thin thread approximately 3.2mm in diameter, using a glass rod with a 3.2mm diameter as a guide. The thin thread was then rolled back into a ball, and rolled into a thin thread again. This process was repeated until cracks developed in the thin thread, at which point the moisture content was determined.

An average of the moisture content of the three samples was taken as the plastic limit of the sample (as can be seen in Appendix A).

Liquid and plasticity index

From the values obtained in the liquid and plastic limit testing, the liquidity and plasticity indexes were then calculated for the material using the equations outlined in Selby (1993) and shown in Appendix A.

The plasticity index (PI) defines the range of water contents between the liquid (LL) and plastic limits (PL):

$$PI = LL - PL$$

The liquidity index (LI), in percent, compares the soils natural moisture content (NMC) with its plasticity:

$$LI\ (\%) = \frac{NMC - PL}{PI}$$

Where a LI of 0% suggests the soil is at its PL, and a LI of 100% suggests it is at its LL.

4.3 Dynamic back-pressured shear box testing

A series of specialist laboratory tests were carried out on remoulded fill samples from the Priscilla Crescent site using a Dynamic Back-Pressured Shear Box (DBPSB). The

DBPSB was developed by GDS Instruments Ltd., and is a relatively novel apparatus for laboratory-based landslide testing (Figure 4.3). The DBPSB allows static and dynamic direct shear testing to be undertaken while being able to control and measure the pore pressure within the sample (Brain et al., 2015; Carey et al., 2017). Importantly, this capability provides a unique opportunity to investigate how shear surfaces develop within fill slopes in response to increasing pore-water pressures.

The device uses samples of 100 x 100 mm (plan) and 20 mm (depth) dimensions. Samples are placed in a sample chamber that is divided into an upper and lower section (to allow for shearing). During sample preparation, the upper and lower sections are kept connected using two screws as the sample is placed into the chamber away from the rest of the DBPSB apparatus. An in-tact or remoulded sample is placed above the porous plate (present in a recess), with two pieces of filter paper (of the same 100 x 100 mm dimensions) placed on either side of the sample. An upper porous plate is then placed above the sample and filter paper. The sample chamber is then secured in the DBPSB pressure vessel using four screws, before a vertical spacer is placed on top of the sample chamber and the two securing screws (holding the upper and lower sections) are removed. The pressure vessel is then sealed by mounting and fastening in place the upper section of the DBPSB, while at the same time making sure the normal load cell (NLC) aligns with the sample chamber. Securing clamps are then fastened to hold the sample chamber in place, and the pressure vessel (surrounding the sample chamber) is then flooded with de-aired water.

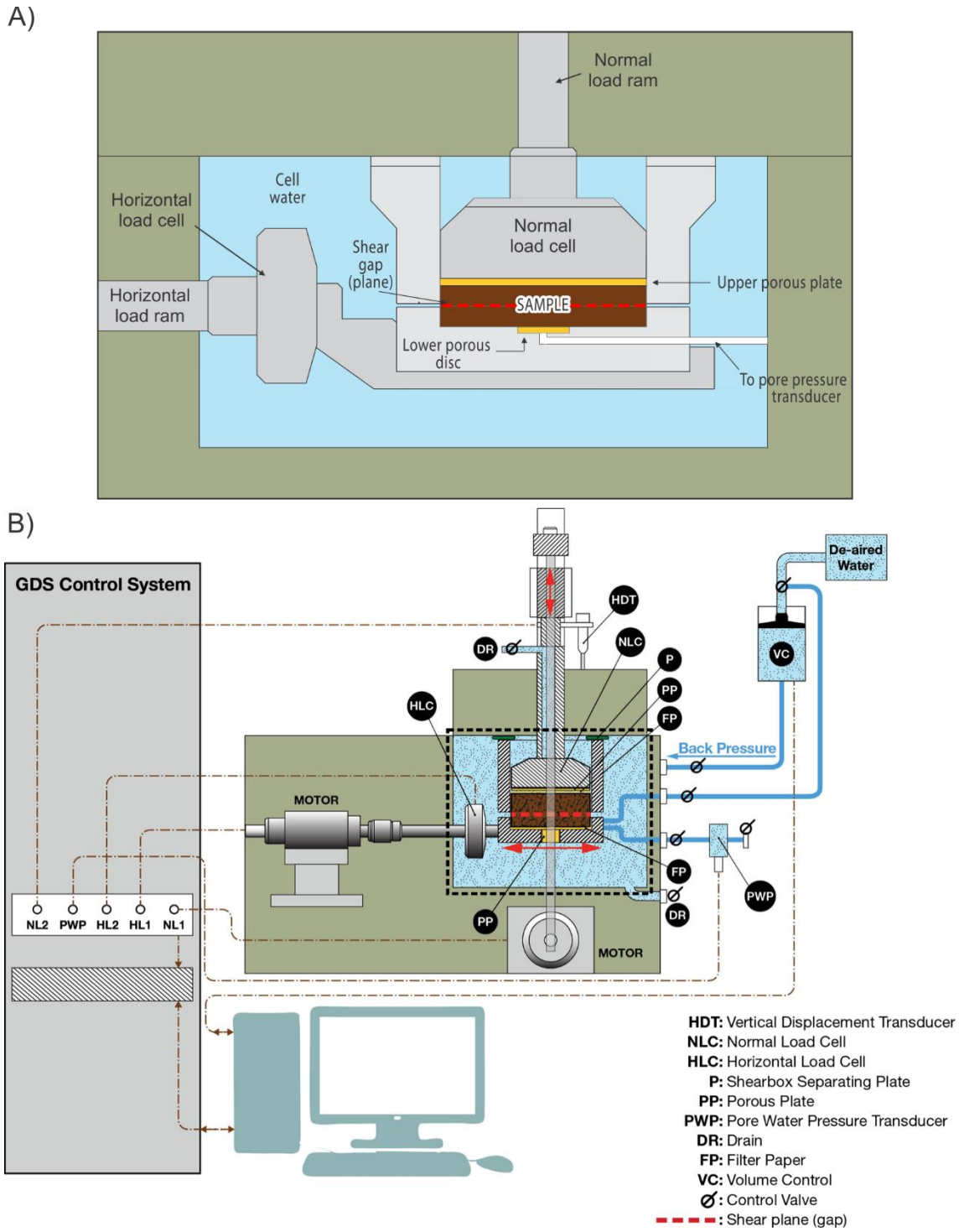

Figure 4.3: Schematic of the dynamic back pressured shear box (DBPSB), A) displays area highlighted by black-dashed box in B). Sources: A) adapted from Brain et al. (2015), B) from Carey et al. (2017).

Samples are tested in saturated conditions as described in Section 4.3.2. Once saturated (or not), the sample is then loaded (consolidated) using the normal load ram (NLR), simulating in-situ hillslope conditions (i.e. the weight of overlying material). The upper section of the sample chamber is then lifted by fastening multiple screws, creating space to allow for shearing to take place. During shearing, the upper section is

held steady, as the lower section is displaced by the horizontal load ram (HLR). Shearing can be controlled by increasing the shear stress at a given rate, increasing the PWP and thus decreasing the effective stress, or by specifying a displacement rate (Brain et al., 2015).

The device is controlled using GDSLab software, which was set to record measurements of all variables (horizontal displacement, stress and load; normal displacement, stress and load; pore pressure; back pressure, back volume) throughout testing at ten second intervals.

4.3.1 Sample preparation

Three different soil sample types that had different particle size distributions (PSDs) were used throughout testing: 0-0.4mm (PSD1), 0-2mm (PSD2) and 0.4-2mm (PSD3). Samples were prepared by first dry sieving both the undisturbed and disturbed fill samples collected from the Priscilla Crescent site into the specified particle size ranges. 100 x 100 x 20mm remoulded samples were then prepared for each test which reflected the true natural density and moisture content of the fill material identified during the physical property testing.

4.3.2 Sample saturation and consolidation

Samples were initially saturated to replicate worse-case ground conditions in a hillslope. Carbon-dioxide was first pumped through the sample at a slow, controlled rate, to remove the pore-air (carbon-dioxide was used as it readily dissolves in water). De-aired water was then pumped through the sample, again at a slow rate, filling all of the pore space. The back-pressure and normal stress were then raised simultaneously to 150 and 160kPa respectively, in order to dissolve any remaining carbon-dioxide into solution ensuring complete saturation. A constant effective normal stress of 10kPa was maintained during this stage to ensure no sample swelling occurred.

Following the completion of the saturation stage, and prior to shearing, samples were consolidated to replicate in-situ conditions. This was achieved by applying a specified normal load to the samples over a ten minute period. The testing conditions were then held constant until any resulting consolidation (change in axial strain) concluded. The amount and trend of the load applied varied between tests.

4.3.3 Conventional drained direct shear testing

The DBPSB was initially used to undertake a series of conventional, drained direct shear tests in order to identify the conventional failure envelopes (CFEs) of the three soil samples and investigate the basic behaviour of the materials. Results from these tests will also define failure parameters to be used in the design of future tests.

Following saturation, the samples were first consolidated at an effective normal stress of 50kPa. Once this first stage of consolidation was completed, the samples were then subjected to three stages of displacement-rate controlled shearing at a rate of 0.1mm/minute. These stages were labelled 1A, 1B and 1C, corresponding to shearing 6cm forward (A), 12cm backwards (B) and then 6cm forwards (C).

Once the first shearing stages were completed, the samples were then reconsolidated at an effective normal stress of 150kPa. Another three stages of shearing, identical to the first stages, were then undertaken (labelled 2A, 2B, and 2C). Once again, following the completion of the second shearing stages, the samples were reconsolidated once more under an effective normal stress of 400kPa and three shearing stages (3A, 3B, and 3C) were completed.

In total, three shearing stages at normal effective stresses of 50, 150 and 400kPa were completed in order to determine the CFEs of the three soil samples. A summary of the CFE tests and key parameters used are shown in Table 4.1.

Table 4.1: Conventional direct shear tests

Test reference	Sample	Consolidation stress (kPa)	Shear rate (mm/min)	PPI rate (kPa/hr)	Sample condition
DS1	PSD1	50, 150, 400	0.1	n/a	remoulded
DS2	PSD2	50, 150, 400	0.1	n/a	remoulded
DS3	PSD3	50, 150, 400	0.1	n/a	remoulded

4.3.4 Rapid direct shear testing with pore-water pressure measurement

A set of displacement-rate controlled rapid direct shear tests were conducted on the three soil samples to investigate their PWP response to shearing.

Following the completion of the saturation stage, samples were consolidated at an effective normal stress of 150kPa. Samples were then sheared from 0 to 7.5mm at a constant rate of 1.5mm/minute. Once PWP had then dropped back to the baseline value

of 150kPa following the first rapid shear, the samples were then sheared from 7.5 to 0mm at the same rate (1.5mm/minute).

A summary of the rapid shear tests and the key parameters used are shown in Table 4.2.

Table 4.2: Direct rapid shear tests

Test reference	Sample	Consolidation stress (kPa)	Shear rate (mm/min)	PPI rate (kPa/hr)	Sample condition
RS1	PSD1	150	1.5	n/a	remoulded
RS2	PSD2	150	1.5	n/a	remoulded
RS3	PSD3	150	1.5	n/a	remoulded

4.3.5 Pore pressure inflation testing

In order to simulate the conditions of rainfall-induced slope failure, a set of pore-pressure inflation (PPI) tests were carried out on the three samples. During these PPI tests, the shear stress is held at a constant rate, while the pore-pressure in the sample is increased at a specified style and rate in order to replicate the effects of different rainfall scenarios; ultimately leading to a reduction in the effective normal stress and eventual failure.

Normally-consolidated linear PPI

Linear PPI tests were carried out on all three samples. Samples were first normally consolidated at an effective normal stress of 150kPa. The shear stress was then raised to 70% of the samples CFE at an effective normal stress of 150kPa, which was obtained during the CFE testing described in Section 4.3.3. This corresponded to a shear stress of 42kPa for PSD1, 65kPa for PSD2, and 70kPa for PSD3.

Following the application of the shear stress and the termination of any displacement that developed as a result, the PWP was raised from 150kPa at a rate of 5kPa/hour until failure.

Over-consolidated linear PPI

Linear PPI tests were also carried out on two over-consolidated PSD2 samples. These over-consolidated tests were only undertaken on the PSD2 material as it contains the PSD most representative of fill slopes. The only difference between these tests and the previously described linear PPI tests, is that here the samples were consolidated at a greater effective normal stress. The first sample was consolidated at an effective

normal stress of 300kPa, while the second was consolidated at 600kPa. Once the samples had finished consolidating, the effective normal stress was then reduced to 150kPa, producing an over-consolidation ratio of two (OC2) and four (OC4) respectively. Following this reducing of the effective normal stress, the linear PPI test was carried out as described above, by increasing the PWP at 5kPa/hour until failure.

A summary of all PPI tests carried out and the key parameters used is shown in Table 4.3

Table 4.3: PPI tests

Test reference	Sample	Consolidation stress (kPa)	Shear rate (mm/min)	PPI rate (kPa/hr)	Sample condition
PPILinear1	PSD1	150	n/a	5	remoulded
PPILinear2	PSD2	150	n/a	5	remoulded
PPILinear3	PSD3	150	n/a	5	remoulded
PPILinear2-OC2	PSD2	300	n/a	5	remoulded
PPILinear2-OC4	PSD2	600	n/a	5	remoulded

5 Results

5.1 Physical properties

The fill material collected from the Priscilla Crescent landslide site was described in-situ as:

Sandy fine to coarse GRAVEL with minor silt and trace organics; light brown to yellow. Moderately to loosely packed; dry; well graded. Gravel, sub-angular to angular, moderately weathered greywacke (indurated sandstone); Sand, fine to coarse; Organics, rootlets.

The physical properties of the fill material obtained during laboratory testing are presented in Table 5.1, and indicate the material has an average moisture content of 7.5%, and an average bulk density of 2.39g/cm^3. The total PSD analysis determined that the majority of the material (by mass) consists of fine to coarse gravel (72%), whilst the remainder consists of cobbles (8%), sand (16.5%) and fines (3.5%) (Figure 5.1). Analysis of material finer than 1.5mm, which accounts for approximately 17% of the total material by mass, revealed more specifically that this finer portion of the material consists of 66% sand, 31% silt, and 3% clay (Figure 5.2).

Table 5.1: Physical properties of the Priscilla Crescent fill.

Physical property	Priscilla Crescent Fill
Dry density (g/cm^3)	2.23
Bulk density (g/cm^3)	2.39
Organic content (%)	3.5
Moisture content (%)	7.5
Particle size:	
Cobble (%)	8
Gravel (%)	72
Sand (%)	16.5
Fines (%)	3.5
Material finer than 425µm:	
Liquid limit (%)	28.6
Plastic limit (%)	19.1
Liquidity index	-1.2
Plasticity index	9.4
Class	CL

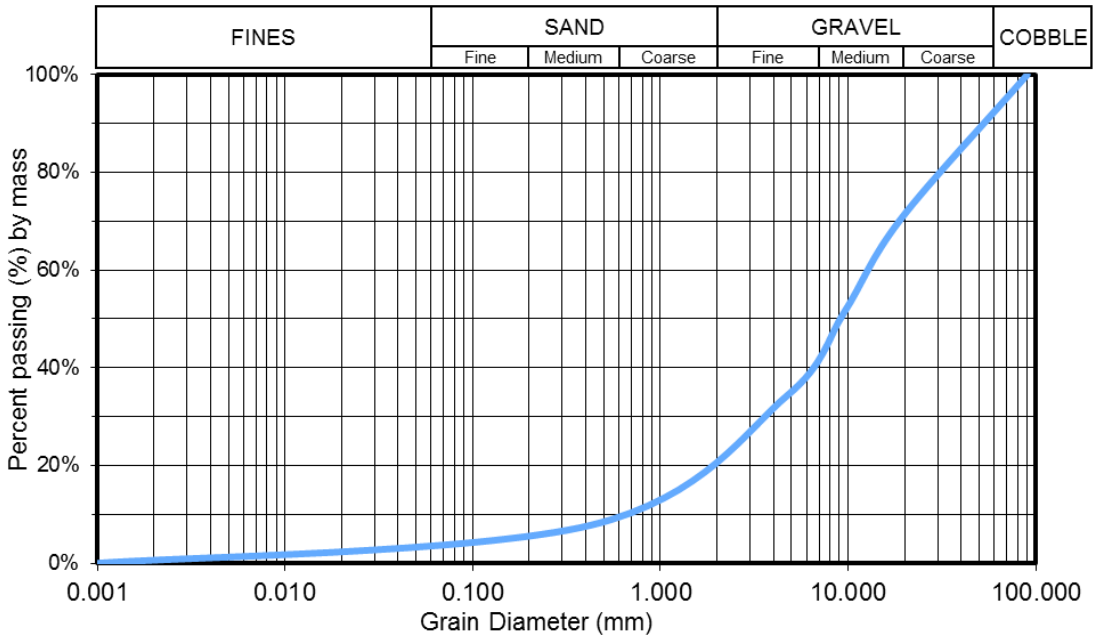

Figure 5.1: Total particle size distribution of the Priscilla Crescent fill obtained from dry sieving.

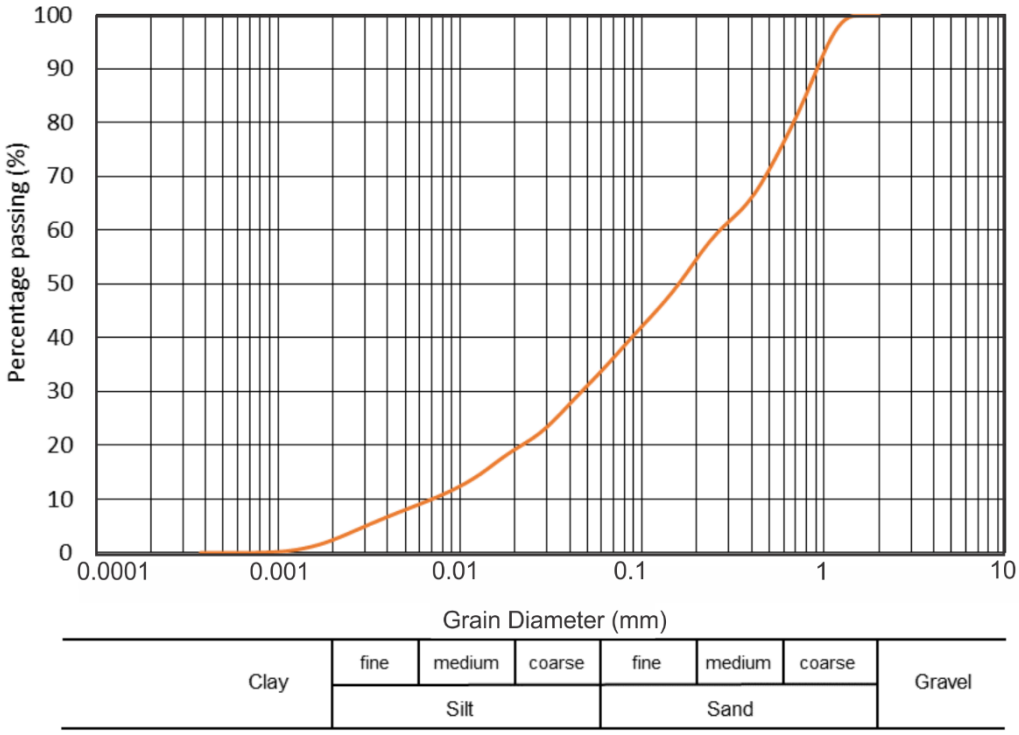

Figure 5.2: Particle size distribution of material finer than 1.5mm in the Priscilla Crescent fill obtained from LPS.

Atterberg limit testing conducted on the material finer than 425µm revealed that the fill material contains a low plasticity clay (Figure 5.3), with a plastic limit of 19.1% and a liquid limit of 28.6% (Appendix A).

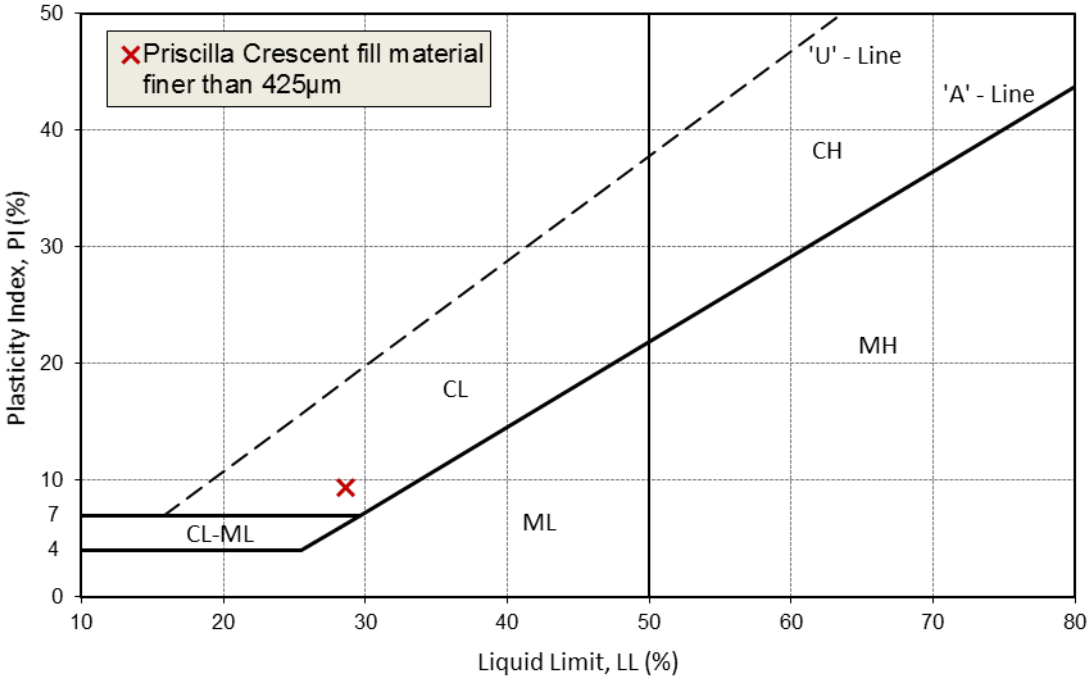

Figure 5.3: Classification of the fill material finer than 425µm collected from the Priscilla Crescent site using a plasticity chart. Note: M = Silt, C = Clay, L = Low plasticity index, H = High plasticity index. The 'A' line separates clays and silts, and the 'U' line represents the approximate upper boundary for the properties of natural soils (i.e. natural soils should plot below).

5.2 Dynamic back-pressured shear box testing

To accomplish the aims of the study, a series of specialist laboratory tests were carried out using a DBPSB. A summary of the tests conducted and key parameters used is presented in Table 5.2.

Table 5.2: Summary of all test conducted using the DBPSB

Test reference	Sample	Consolidation stress (kPa)	Shear rate (mm/min)	PPI rate (kPa/hr)	Sample condition
CFE1	PSD1	50, 150, 400	0.1	n/a	remoulded
CFE2	PSD2	50, 150, 400	0.1	n/a	remoulded
CFE3	PSD3	50, 150, 400	0.1	n/a	remoulded
RS1	PSD1	150	1.5	n/a	remoulded
RS2	PSD2	150	1.5	n/a	remoulded
RS3	PSD3	150	1.5	n/a	remoulded
PPILinear1	PSD1	150	n/a	5	remoulded
PPILinear2	PSD2	150	n/a	5	remoulded
PPILinear3	PSD3	150	n/a	5	remoulded
PPILinear2-OC2	PSD2	300	n/a	5	remoulded
PPILinear2-OC4	PSD2	600	n/a	5	remoulded

5.2.1 Consolidation behaviour

During direct shear testing, all samples underwent three stages of consolidation at normal effective stresses (p') of 50, 150 and 400kPa. When viewing consolidation data from the direct shear tests (Figure 5.4 A), it is important to note that the three consolidation stages for each PSD occurred on the same sample, with stages of shearing (and subsequent consolidation) in between. This means we do not see increasing amounts of axial strain (ε_a) occurring when the samples are consolidated at an increasing effective stress; importantly, it is the overall behaviour of the different materials which is of interest. In general, we can see the PSD2 sample consolidates the least, and PSD3 the most (Figure 5.4 A). This behaviour is most easily observed when looking at the axial strain occurring during the first consolidation stage (solid lines), or when comparing the total axial strain that occurred over the entire set of direct shear tests (dotted lines).

Consolidation data from the (normally consolidated) rapid shear and linear PPI tests where all samples were consolidated under an effective stress of 150kPa is more variable than the direct shear data (Figure 5.4 B). In saying this, a similar trend can still be observed, with the PSD3 material generally undergoing the most consolidation, and the PSD2 samples the least, with irregularities likely the result of sample variability.

Data from PPI testing on the over-consolidated PSD2 material displays an expected trend, with samples consolidated under greater effective stresses experiencing the greatest amount of axial strain (consolidation) (Figure 5.4 C). The average axial strain occurring on the normally consolidated PSD2 samples was ~18%, while the over-consolidated samples experienced 24% and 35% axial strain for the OC2 and OC4 samples respectively.

Overall, data across all tests indicates that the PSD3 material is predisposed to experiencing the greatest amount of consolidation, followed by PSD1, whereas the PSD2 material is prone to consolidating the least. Additionally, an increase in the consolidation stress is observed to increase the amount of consolidation that occurs.

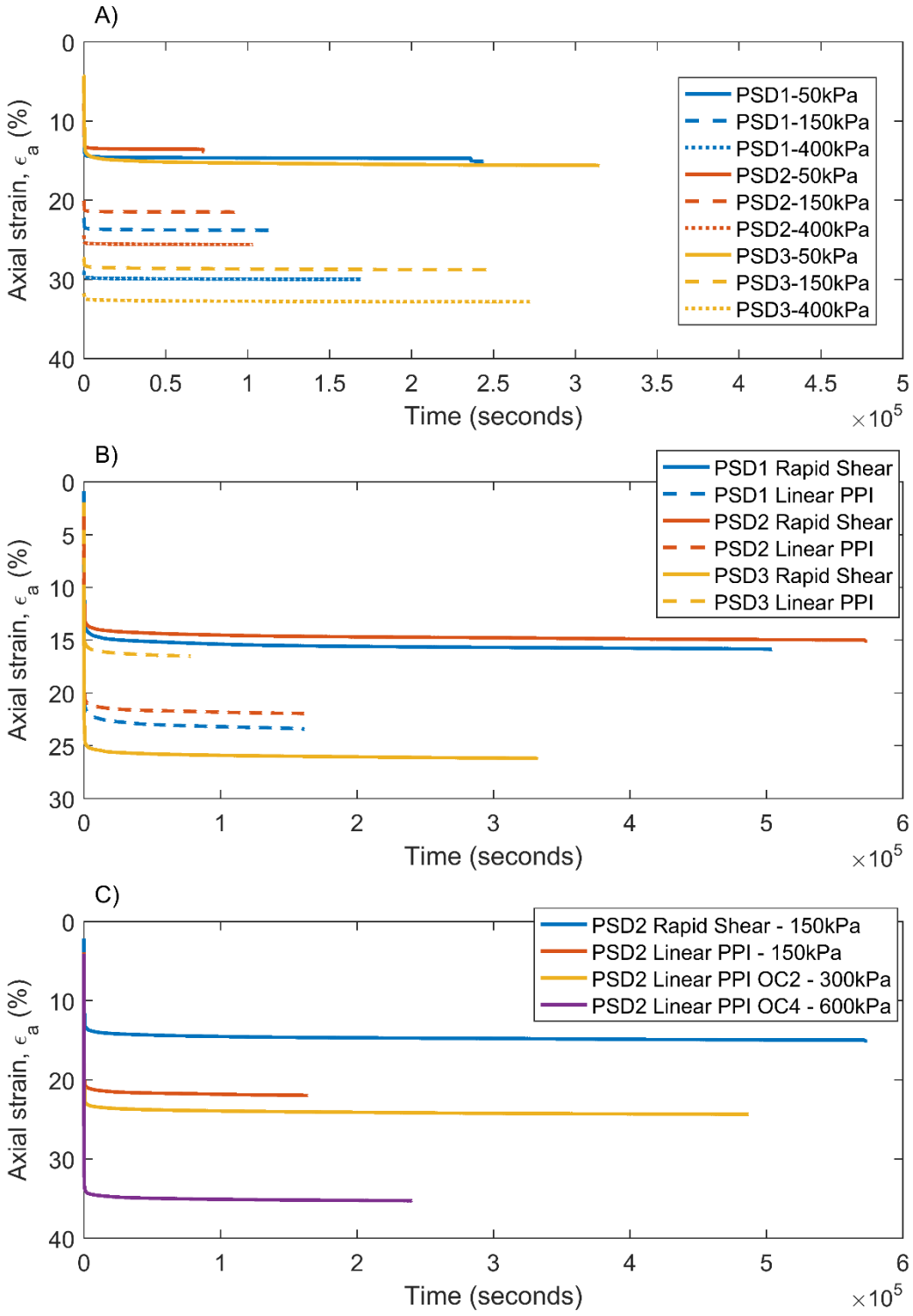

Figure 5.4: Consolidation results from all testing. A) Conventional direct shear testing, B) Rapid shear and linear PPI testing – all samples consolidated at 150kPa, C) Over-consolidation testing. Note an increase in axial strain (ε_a) indicates sample consolidation.

5.2.2 Conventional direct shear testing

During the direct shear testing, samples were subjected to three stages of displacement-rate controlled shearing under different effective stresses (p') (50, 150, 400kPa). Note that shear 'stages' correspond to 1, 2, 3, while shear 'phases' corresponds to A, B, C.

In general, all three materials initially display strain-hardening behaviour, before either continuing to strain-harden at decreased rates, or achieving a steady state where strain continues to accumulate with little or no further increase in stress. Only two minor periods of strain-softening behaviour are observed across all shear phases.

PSD1 stress-strain behaviour (Figure 5.5)

During the first stage of shearing, PSD1 exhibits a similar behaviour across all shearing phases. Initially, the PSD1 sample undergoes a period of increasing stress with strain, before strain then begins to accumulate with very little further increase in stress. Each subsequent shear phase during stage one (1B, 1C) reaches a higher shear stress than the previous phase. Shear phase 2A displays a more rapid increase in stress with little strain accumulation, before the rate of stress increase, reduces, and a peak shear strength is reached after approximately 10% strain. After reaching the peak, the stress required for strain to accumulate slowly reduces until a residual shear strength is reached after ~30% strain. Phases 2B and 2C initially undergo much more gradual increases in stress with strain, until a steady state is reached at around 30% strain. The stress required in phases 2B and 2C is approximately twice as much as that observed during phase 2A. During the third shear stage, shear phase 3A initially displays a rapid increase in stress, before the rate of stress increase reduces developing into a shallow linear trend. Shear phase 3B and 3C first undergo relatively subdued increase in stress with strain when compared to 3A, before reaching approximately 20% strain a similar shallow linear relationship develops. Analogous to the behaviour from the second shear stage, shear phases 3B and 3C reached approximately double the stress of shear phase 3A.

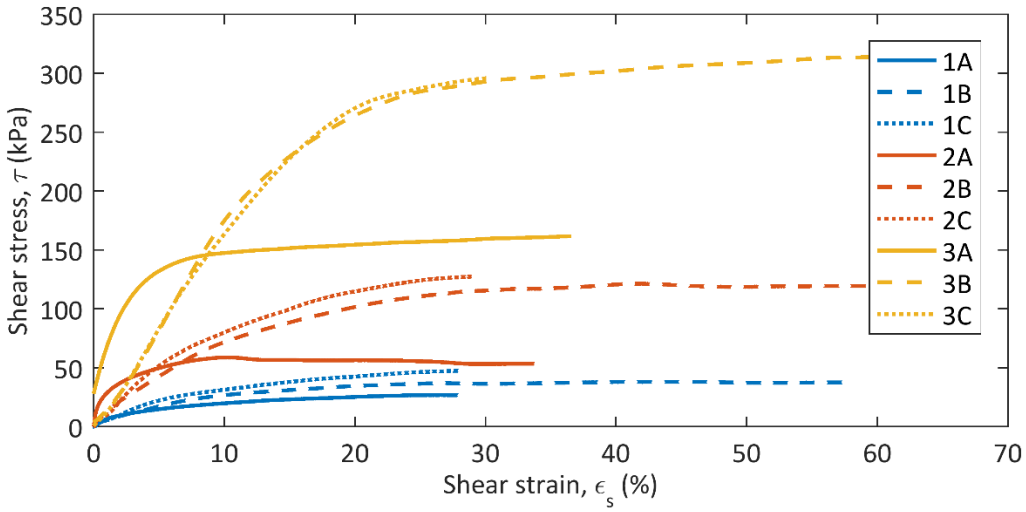

Figure 5.5: Stress-strain behaviour of PSD1 obtained from conventional direct shear testing.

PSD2 stress-strain behaviour (Figure 5.6)

The PSD2 material displays a similar behaviour in all shear phases of the first stage, with the material first undergoing a very gradual increase in stress with strain, before an approximately linear relationship develops after ~8% strain. Shear phase 2A initially shows a much more rapid rise in stress with strain, before a shallow linear trend develops after ~3% strain. Shear phases 2B and 2C first experience a gradual increase in stress with strain, before reaching a somewhat similar linear trend to phase 2A, albeit at almost twice the shear stress and after nearly 25% strain. The behaviour during the third shear stage is analogous to that of the second. Shear phase 3A undergoes a rapid increase in stress with strain, before developing into a linear trend after approximately 5% strain. While during phases 3B and 3C, stress increases more gradually with strain, before a similar linear trend develops at a much higher shear stress and after approximately 24 and 34% strain respectively.

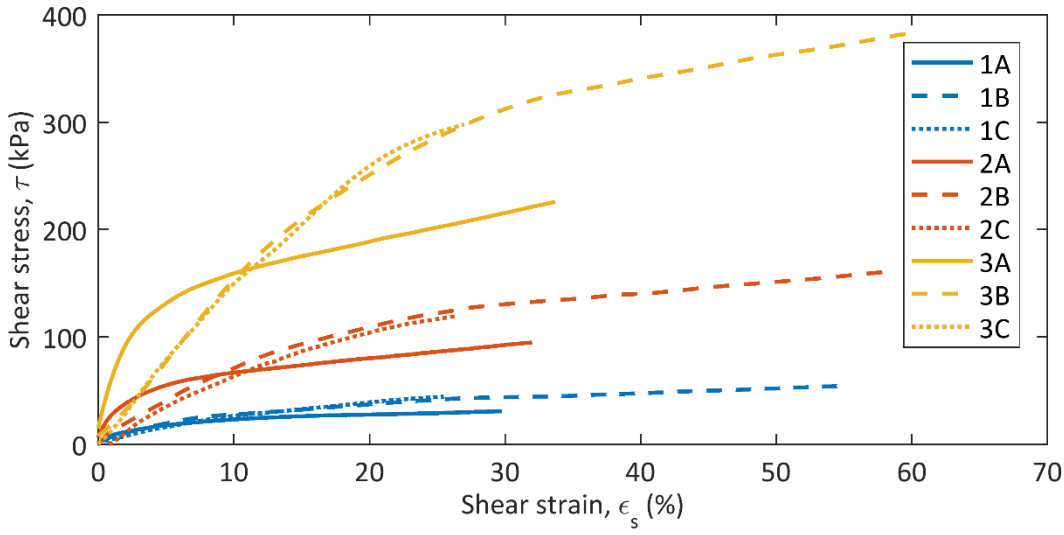

Figure 5.6: Stress-strain behaviour of PSD2 obtained from conventional direct shear testing.

PSD3 stress-strain behaviour (Figure 5.7)

During the first shear stage, the PSD3 material displays a consistent behaviour across all three phases, characterised by a very minor, but rapid initial increase in stress to roughly 0.5% strain, before a shallow linear relationship develops after ~1% strain. The second shear stage is much like the first, undergoing an initial period of rapid increase in stress with strain until reaching approximately 2% strain, after which, strain continues to accumulate with very little further increase in stress as a shallow linear trend develops. Phases 2B and 2C require over twice the shear stress as observed in phase 2A. Shear phases during the third shear stage are analogous to those observed in

the first and second stages, undergoing an initial rapid increase in stress to approximately 5% strain, before the rate of stress increase reduces significantly and develops into a linear trend. Phases 3B and 3C require well over double the stress as observed in 3A.

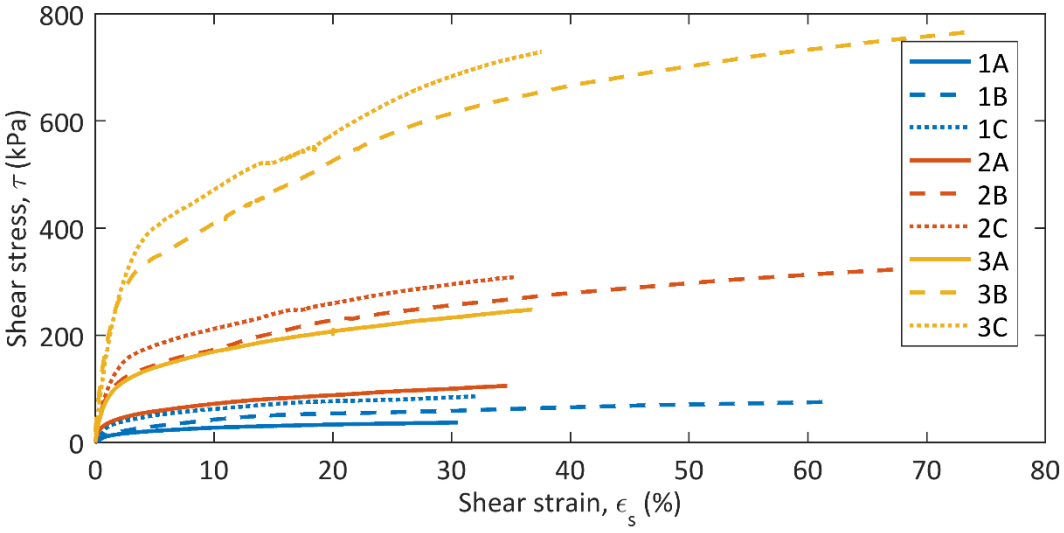

Figure 5.7: Stress-strain behaviour of PSD3 obtained from conventional direct shear testing.

Conventional failure envelopes

From the above stress-strain plots, multiple CFEs for each material could be obtained by picking the peak shear strength value from each shear stage and plotting it against the consolidation stress under which the shear took place. In all cases, the failure envelopes obtained were linear (Figure 5.8; Figure 5.9). Originally, just the initial shear phase (1A, 2A, and 3A) of each stage was used as it is the most representative of first-time failure in the material. The subsequent shear phases (1B, 1C, 2B, 2C, 3B, and 3C) were also analysed, and are presented here to investigate how the behaviour evolves with subsequent shearing.

The CFEs for first-time shears (failures) in each material clearly shows that PSD1 is significantly weaker than both PSD2 and PSD3 samples, displaying a friction angle (φ') of 22.1° and cohesion (*c*') of 2kPa (Figure 5.8). PSD3 was the strongest of the three materials, exhibiting φ' and *c*' values of 32.0° and 4.7kPa, respectively, slightly more than the 29.9° and 3.5kPa recorded for PSD2. The low cohesion values obtained are to be expected due to the nature of remoulded samples.

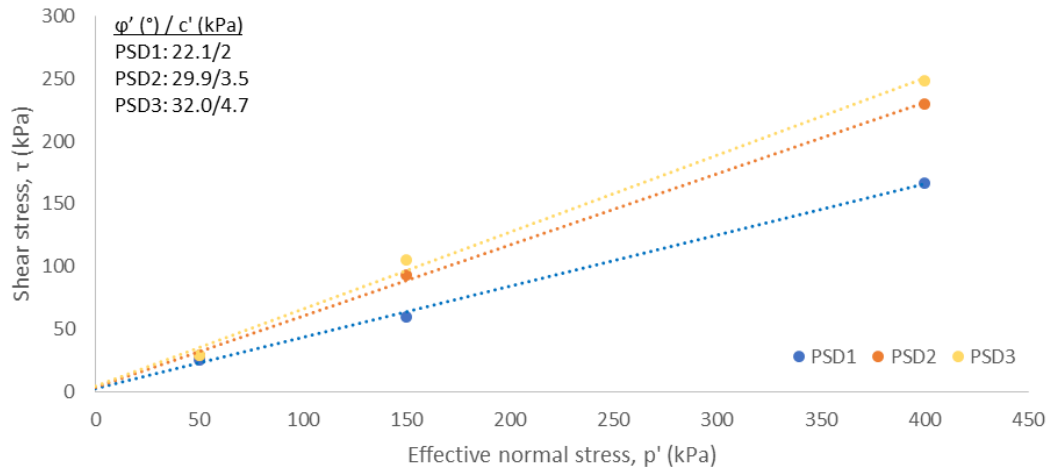

Figure 5.8: CFEs and soil friction angles of the three different PSDs obtained from conventional direct shear testing.

When investigating how the materials' CFE characteristics changed with subsequent shearing stages, it can be seen that all three samples strengthened significantly from the first shearing phase to the second (A to B) (Figure 5.9). PSD1's φ' value increased from 22.1° to 36.1°, PSD2's increased from 29.9° to 42.6°, and PSD3's increased from 32.0° to 63.2°. This increase in sample strength is likely due to the consolidation that occurred across all three samples during the first shearing phases (A) (see Appendix B: Figs. B1, B2, B3). Contrastingly, all three samples weakened slightly following the second shearing stage (B to C) (Figure 5.9). PSD1's φ' value decreased slightly from 36.1° to 34.4°, PSD2's decreased considerably from 42.6° to 35.1°, and PSD3's decreased slightly from 63.2° to 61.4°. Considering all three samples consolidated during the second shearing phases (B) (see Appendix B: Figures. B1, B2, B3), this weakening could be the result of the complete development of a shear surface or grain crushing in the shear region.

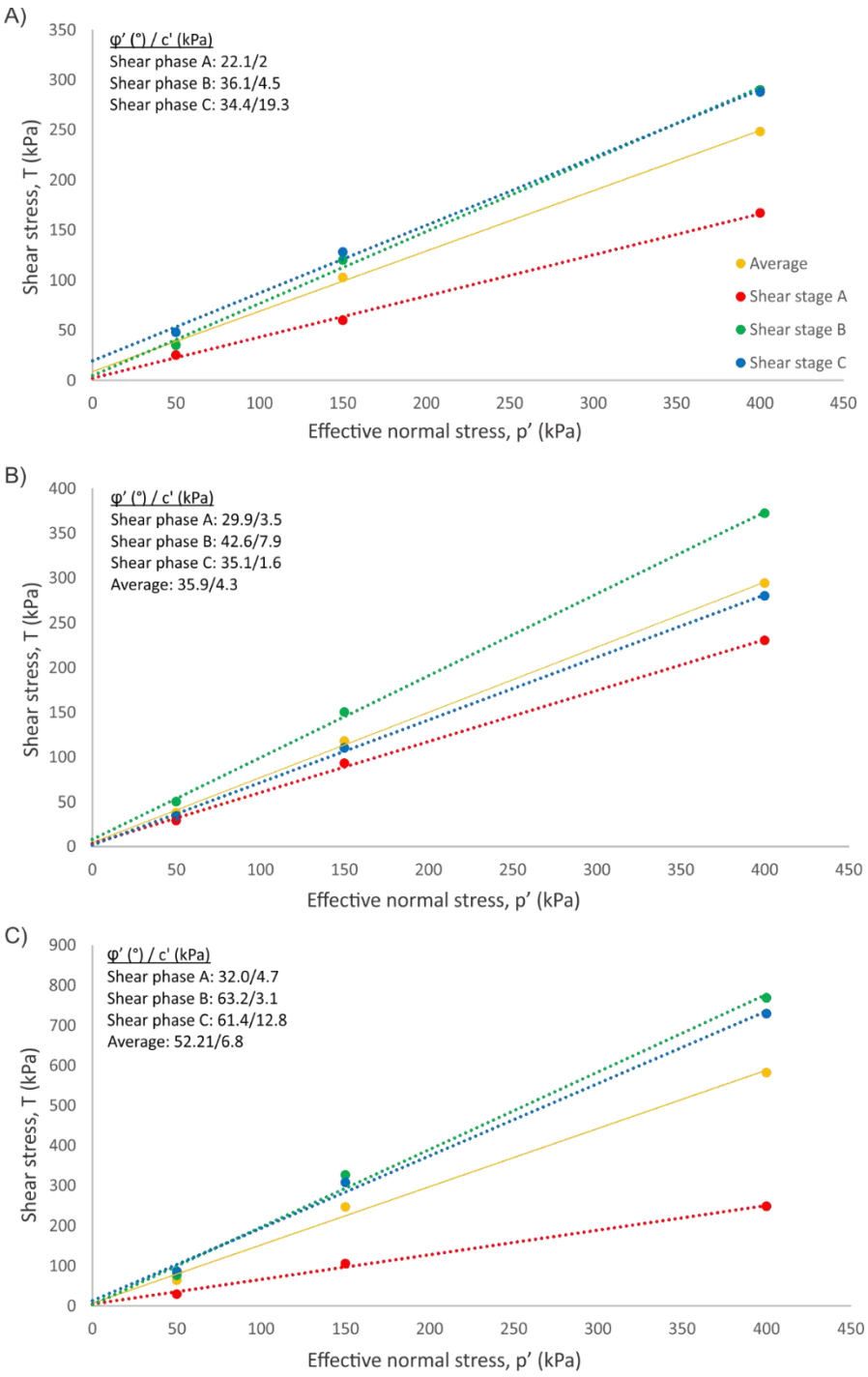

Figure 5.9: All CFEs obtained for each sample during conventional direct shear testing. A) PSD1, B) PSD2, C) PSD3

5.2.3 Rapid direct shear testing with pore-water pressure measurement

To investigate, if, and how the different samples generate and sustain excess PWPs in response to shearing, two stages of displacement-rate controlled shearing were undertaken on all samples. During these tests, all samples were able to generate excess PWPs through the early stages of shear, before subsequent drainage caused PWPs to fall to the baseline value (Figure 5.10). While all samples were able to generate excess PWPs, their behaviour differed notably, in terms of the rate of generation and diffusion

of PWPs, and also the maximum PWP generated. Additionally, there was a marked difference in behaviour observed between the first and second shears.

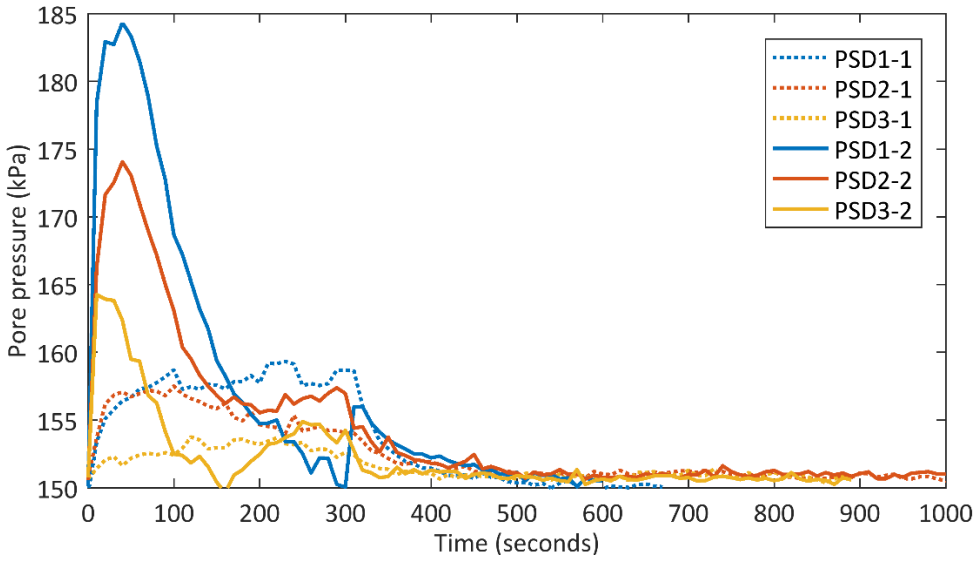

Figure 5.10: PWP generation during rapid shear testing across all samples.

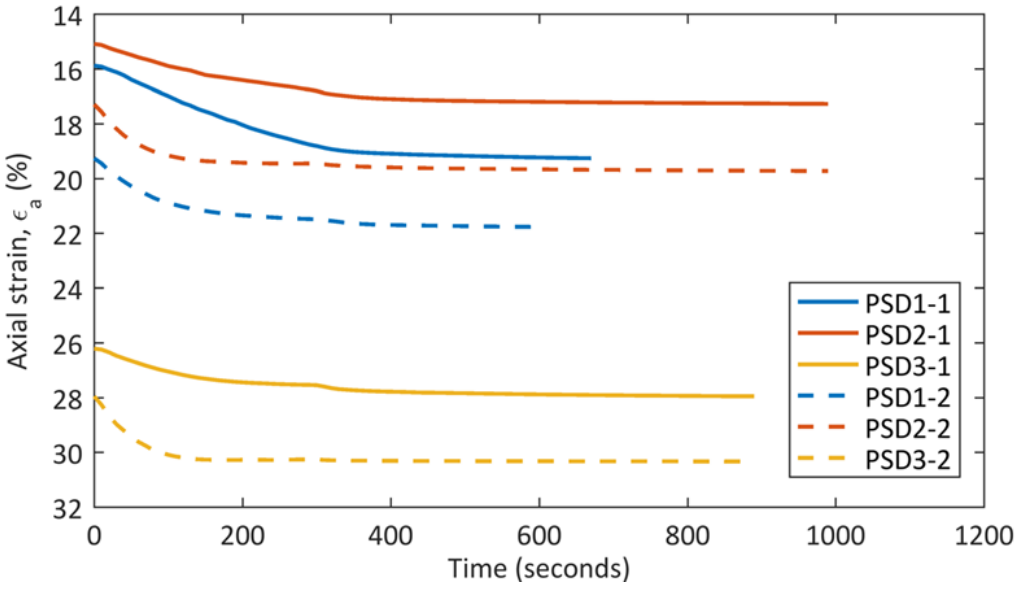

Figure 5.11: Contractive behaviour of samples during rapid shear testing. Solid lines represent rapid shear 1, dashed lines represent rapid shear 2.

During the first rapid shear stage, PSD1 experiences a steep rise in PWP in response to the shearing, generating approximately 8kPa of excess PWP which it sustained throughout the entire shear. Once shearing ceased (after 300 seconds), the excess PWP then dissipated. Similarly, PSD2 initially generates a small amount of excess PWPs rapidly in response to shearing, reaching a maximum of 7.4kPa after 100 seconds. Unlike PSD1 however, the excess PWP generated begins to slowly dissipate as soon as the peak value is reached. Contrasting the behaviour observed in the PSD1 and PSD2

samples, PSD3 generates excess PWP relatively slowly in response to shearing, reaching a maximum of only 3.8kPa after 220 seconds. Following this peak, excess PWPs slowly dissipate back to the baseline value of 150kPa.

Following the completion of the first shearing stage and the stabilisation of PWPs, a second rapid shear stage was carried out on each of the three PSD samples. It is important to note that the first shearing stage altered the physical properties of the samples. Critically, all samples consolidated during shearing (Figure 5.11). PSD1 experienced an axial strain of 3.37%, PSD2 experienced 2.20%, and PSD3 experienced the least axial strain of 1.74%.

In the second rapid shear stage, all three samples exhibited a very similar PWP response to shearing. All samples experienced a steep rise in PWP to a maximum value, with PSD1 generating the most excess PWP at 34kPa, PSD2 generating 24kPa, and PSD3 generating the least at 14kPa; analogous to the behaviour observed in the first rapid shear stage. The PWP then fell in all three samples after reaching its peak value at a much faster rate than observed in the first rapid shear test, with PSD1 sustaining its excess PWP for the longest, and PSD3 draining the quickest. The PSD2 and PSD3 samples displayed slightly different draining behaviour to that of PSD1. The excess PWPs in the PSD1 sample drained completely after reaching a peak value, whereas the PSD2 and PSD3 samples had drained the majority of excess PWPs after around 150 seconds before they then stabilised, and in the case of PSD3 increasing again slightly. Following the end of the test (300 seconds), PSD1 displayed a small, sharp increase in PWP, which was a product of the DBPSB adjusting once the test had finished and is not related to the sample behaviour.

While PSD1 was able to generate the most excess PWP, and PSD3 generated the least, just like the behaviour observed in the first rapid shear stage, the amount of PWP generated was significantly different. All samples generated more than three times the amount of excess PWP in the second rapid shear stage than in the first, indicating a strong relationship between decreasing sample volume (decreasing void ratio) and the maximum amount of PWP generated (Figure 5.12).

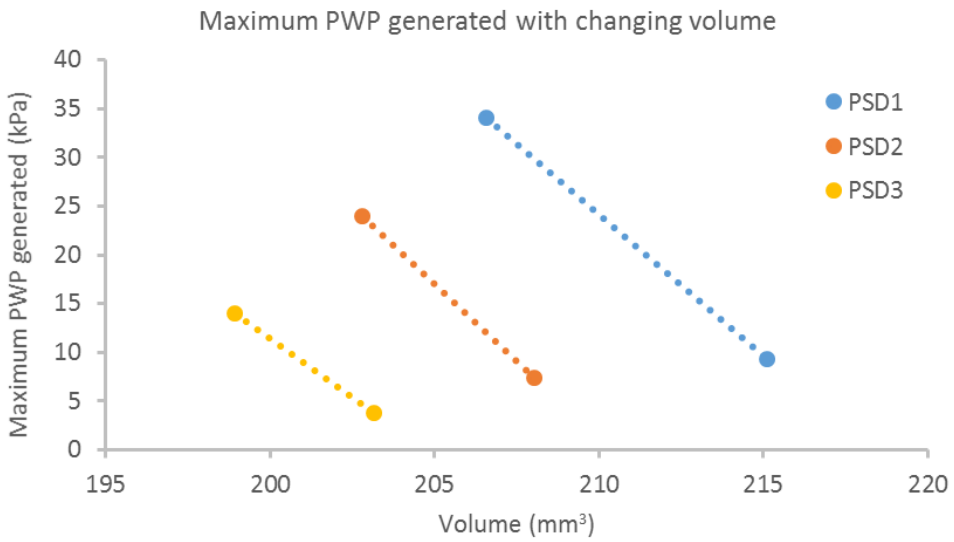

Figure 5.12: Relationship between sample volume and maximum generated PWP.

In general, we can see from the rapid direct shear tests that the presence of finer material (PSD1 and PSD2) generates higher and sustains longer excess PWP, while the coarse material (PSD3) generates less and drains quicker. Furthermore, we also see that with increasing density the amount of excess PWPs generated increases across all samples.

5.2.4 Pore pressure inflation testing

A series of specialist PPI tests were carried out on all three sample types to better understand their deformation behaviour in response to changing pore-pressure conditions. During these tests, the effective normal stress of the samples was reduced by increasing the PWP at a linear rate of 5kPa/hour until failure was reached.

Linear PPI on normally consolidated samples

The first set of linear PPI tests were carried out on samples that were normally consolidated under an effective stress of 150kPa.

The results indicate all three samples display slightly different failure characteristics in response to increased PWPs; Figure 5.13 correlates the initiation of deformation during PPI testing with the CFEs obtained for each material during direct shear testing; Figure 5.14 displays datasets obtained from the entire test period, while Figure 5.15 displays the pre-failure deformation that occurred in more detail.

There is a strong correlation between the onset of deformation observed during PPI testing and the CFEs obtained for each of the materials (Figure 5.13). Noticeable deformation in the PSD1 sample began at a p' value of ~90kPa, while the CFE is

located at p' = 98kPa. An equally strong correlation was observed in the PSD2 and PSD3 samples, with noticeable deformation in both samples initiating at p' value of approximately 105kPa, while the attained CFEs are situated at p' = 108 and 106kPa respectively.

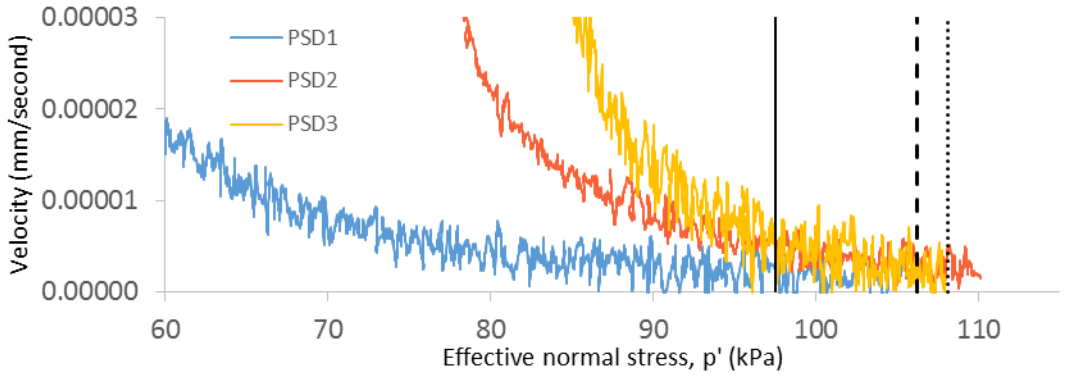

Figure 5.13: Correlation between CFEs obtained during conventional direct shear testing and onset of deformation during PPI testing. Black-solid line = PSD1 CFE, Black-dotted line = PSD2 CFE, Black-dashed line = PSD3 CFE.

All three materials experienced deformation to failure during PPI testing. This was characterised by an initial period of zero displacement until a yield stress was surpassed, where each material then underwent slightly varying periods of pre-failure deformation, before finally experiencing rapid acceleration to failure (Figure 5.14; Figure 5.15 B, D, F).

After an initial phase of little/no displacement, PSD3 begins deforming at the equal lowest effective stress (~105kPa) of the samples and undergoes a relatively long period of pre-failure deformation (~20,000 seconds). This pre-failure deformation is characterised by an approximately linear trend in acceleration, punctuated by small spikes in velocity, until reaching ~0.0007mm/second (Figure 5.15 F). Following this point, the PSD3 sample accelerates hyperbolically until complete failure. Deformation in the PSD2 sample initiated at approximately the same effective normal stress as the PSD3 sample (~105kPa), however, the period of pre-failure deformation experienced was shorter (~17,000 seconds). Ultimately, the PSD2 material was the first to reach complete failure. The velocity initially began to increase hyperbolically in the PSD2 sample until ~0.0003mm/second, before undergoing a short period of linearly increasing velocity to ~0.0007mm/second (Figure 5.15 D). This was then followed by rapid hyperbolic acceleration to failure. Deformation in the PSD1 material displayed a hyperbolic trend in acceleration as soon as deformation began (~90kPa), eventually failing at the lowest p' of the three samples, indicating it requires the highest excess

PWP to induce fail. The PSD1 sample also failed over the shortest period of time (~10,000 seconds), indicating it failed the in the most rapid fashion.

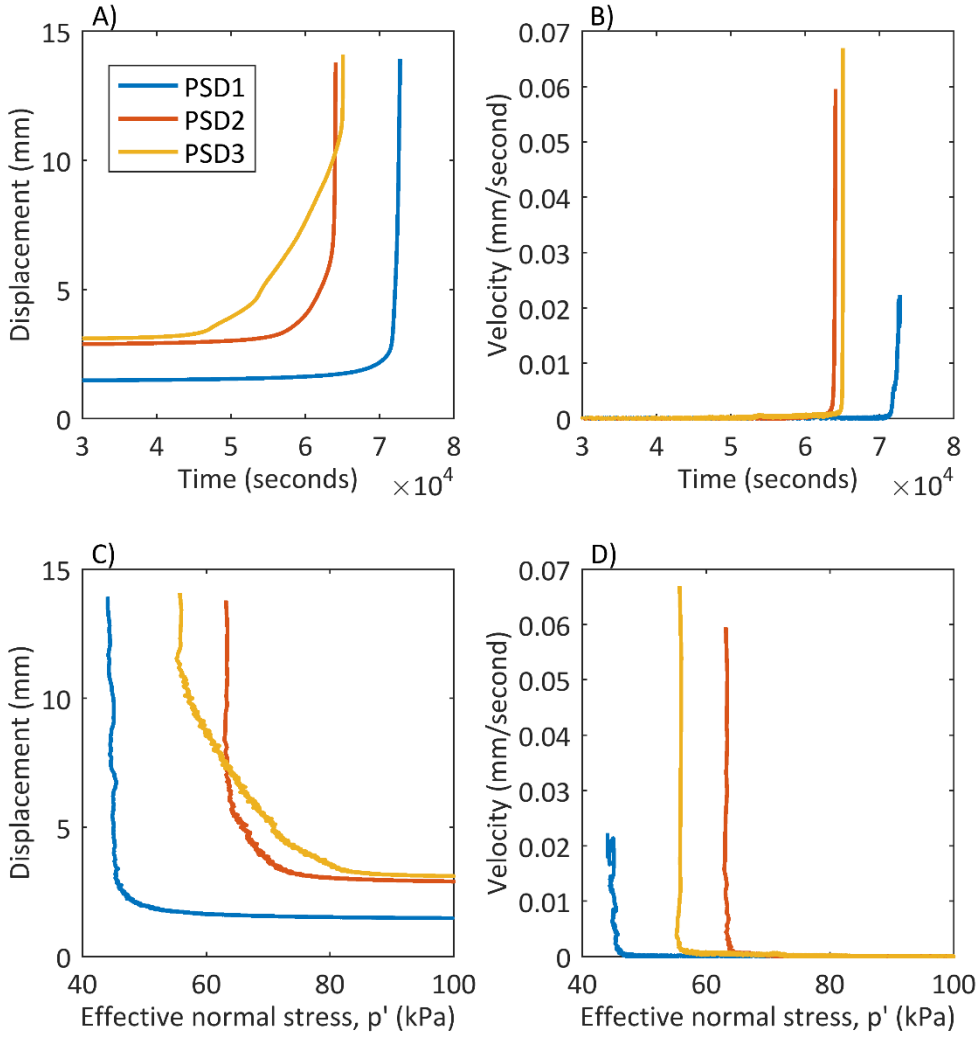

Figure 5.14: Deformation behaviour of all three materials normally consolidated at an ENS of 150kPa during linear PPI tests. A) Displacement against time, B) Velocity against time, C) Displacement against ENS, D) Velocity against ENS.

The different failure behaviour of the three materials in response to increasing PWP is further highlighted when viewing their 1/Velocity trends, with an asymptotic form indicating ductile behaviour, while a linear form indicates a more brittle behaviour; a technique originally developed by Saito (1965, 1969) and later expanded by Petley et al. (2002). Once deformation had been initiated, the PSD1sample initially displayed a period of slightly fluctuating asymptotic trend in 1/Velocity-time space, before transitioning to a clear linear trend through to failure after ~67,500 seconds (Figure 5.15 A). Conversely, both the PSD2 and PSD3 samples displayed a more consistent asymptotic trend in 1/Velocity-time space through to failure, exhibiting only very minor periods of linearity at the conclusion of the tests (Figure 5.15 C & E). The

results of a regression analysis on this deformation period leading to failure further clarifies the trends in 1/Velocity-time space, and reveals the statistical significance of those trends.

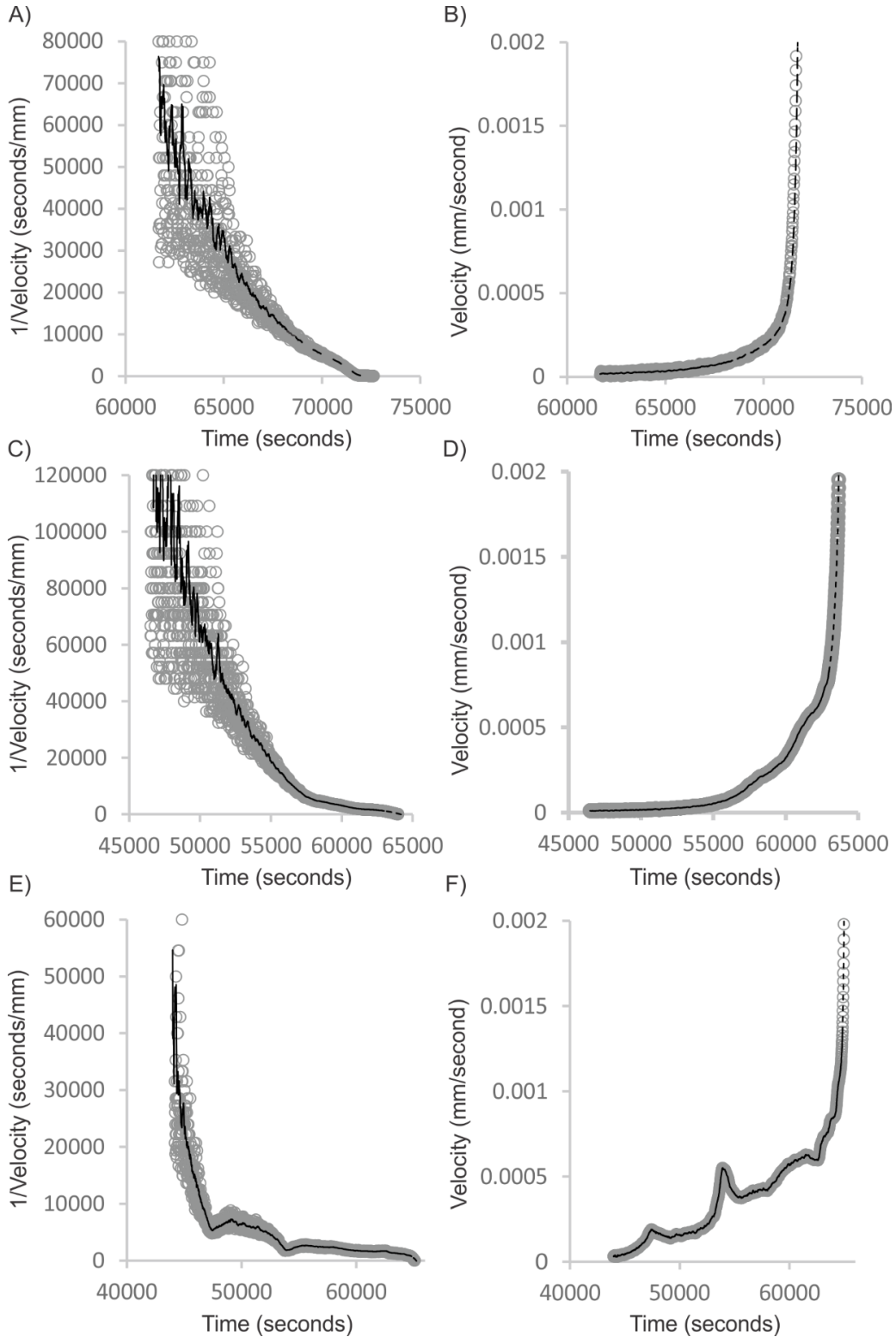

Figure 5.15: Deformation behaviour of the three PSD samples normally consolidated at 150kPa. A) & B) PSD1, C) & D) PSD2, E) & F) PSD3. Note: Grey circles = raw data, black lines = averaged data, black-solid lines = asymptotic trend in 1/Velocity – time space, black-dashed = linear trend in 1/Velocity – time space.

Figure 5.16 displays the best-fit lines of the periods preceding failure, while Table 5.3 presents the coefficients of determination of those, as well as other models, ultimately displaying how closely they fit the data.

The regression analysis demonstrates that the PSD2 sample displays the strongest asymptotic trend, with the data showing a high correlation with both a power law (R^2 =0.9770) and exponential model (R^2 =0.9856) (Figure 5.16 B). Conversely, while PSD1 does exhibit a reasonably strong correlation with both a power law and exponential model, it displays the most significant correlation to a linear model (R^2 =0.9151) (Figure 5.16 A). The PSD3 sample does not show as high a correlation as the other samples with any models, which is likely the product of the two significant declining spikes. In saying this, both the power law (R^2 =0.8979) and exponential (R^2 =0.8783) models display a much better fit than the linear model (R^2 =0.4839), suggesting the sample is displaying a more hyperbolic than linear trend in 1/Velocity-time space to failure (Figure 5.16 C). Visually, it seems that if the two declining spikes were not present, a much more significant hyperbolic fit would be obtained.

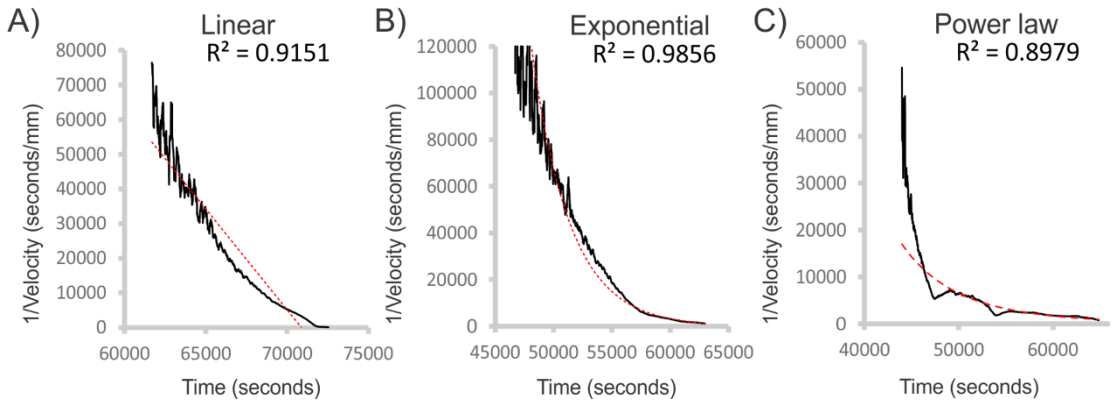

Figure 5.16: Regression analysis of the failure behaviour observed during linear PPI tests on different PSD samples displaying best fit line for each test. A) PSD1, B) PSD2, C) PSD3. Black-solid line represents averaged data, red-dashed line indicates line of best fit.

Table 5.3: Results of regression analysis on pre-failure behaviour in linear PPI tests, displayed as R-squared values for the functions fitted.

Test	Linear fit	Power law fit	Exponential fit
PPILinear1	0.9151	0.8116	0.8240
PPILinear2	0.8297	0.9770	0.9856
PPILinear3	0.4839	0.8979	0.8783

When analysing the axial strain data from the linear PPI tests (Figure 5.17), it can clearly be seen that besides one short period, all samples dilated in response to increasing PWPs. The axial strain that occurred in the PSD3 sample during the test was the most variable of the three, exhibiting periods of slower and more rapid rates of changing axial strain. These variations in rate of axial strain correlate well with changes in deformation velocity (Appendix B, Fig. B4). PSD2 displayed the most consistent trend, showing a continual, hyperbolic decrease in axial strain throughout the entire test. Anomalously, the PSD1 sample contracted towards the end of the test after dilating through the early stages. This contraction began shortly after rapid acceleration to failure began (Appendix B, Fig. B5).

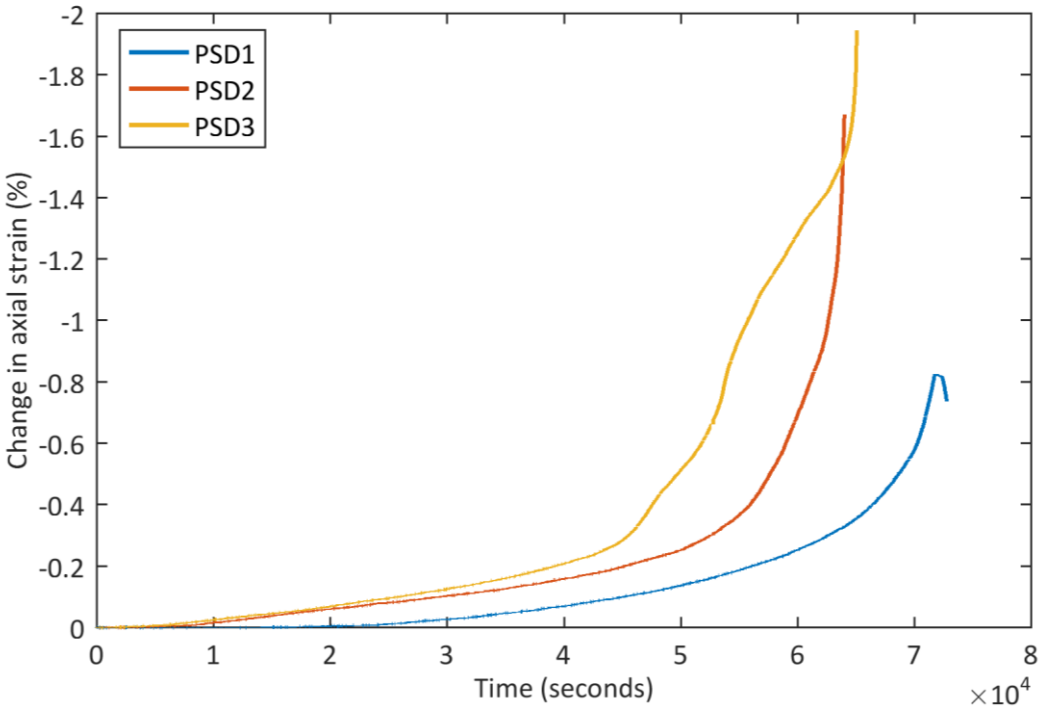

Figure 5.17: Change in axial strain during linear PPI tests. Note: An increasingly negative value signifies sample dilation and decreasing signifies sample contraction

Linear PPI on over-consolidated sample

A set of PPI tests were also carried out on two over-consolidated PSD2 samples (OC2 and OC4), which are compared here with the data obtained from PPI testing on the normally consolidated sample to better understand the influence of density on movement behaviour.

All three materials experienced deformation to failure during PPI testing. This was characterised by an initial period of zero displacement until a yield stress was

surpassed, where each material then underwent slightly varying periods of pre-failure deformation prior to rapid acceleration to failure (Figure 5.18; Figure 5.20 B, D, F).

As described earlier, significant deformation in the normally consolidated PSD2 sample initiated at p' ≈ 105kPa, and failed over a period of ~16,000 seconds. The velocity initially began to increase hyperbolically until 0.0003mm/second, before undergoing a short period of linearly increasing velocity to 0.0007mm/second (Figure 5.20 B). This was then followed by rapid hyperbolic acceleration to failure. The PSD2 OC2 sample behaves quite differently, with the onset of deformation occurring at a much higher p' value of ~125kPa. The sample fails over a period of ~12,500 seconds, initially accelerating to a velocity of approximately 0.0002mm/second, before remaining constant for a short period (Figure 5.20 D). Following the period of steady velocity, the sample accelerated hyperbolically to an initial failure. Following the initial failure, however, drainage of the shear surface caused the velocity to stabilise, before a continued rise in PWP induced another failure (Figure 5.19). Data following the initial failure of the PSD2 OC2 will be ignored, as this secondary failure is a product of the method (discussed in *section 6.2.1*). The PSD2 OC4 sample begins to undergo significant deformation at the lowest p' of all samples (p' ≈ 65kPa) and failed over the shortest period (~4000 seconds). The PSD2 OC4 sample initially experiences a relatively short period of increasing velocity to 0.0006mm/second between p' ≈ 60-45kPa, characterised by greater fluctuations than the other samples (Figure 5.20 F). After reaching a velocity of ~0.0006mm/second, the sample accelerated extremely rapidly towards failure, displaying a hyperbolic trend in velocity-time space. During this phase of acceleration to failure, a slight reduction in the effective stress occurs, suggesting the shear surface may be draining, causing a slight reduction in PWPs (Figure 5.18 C).

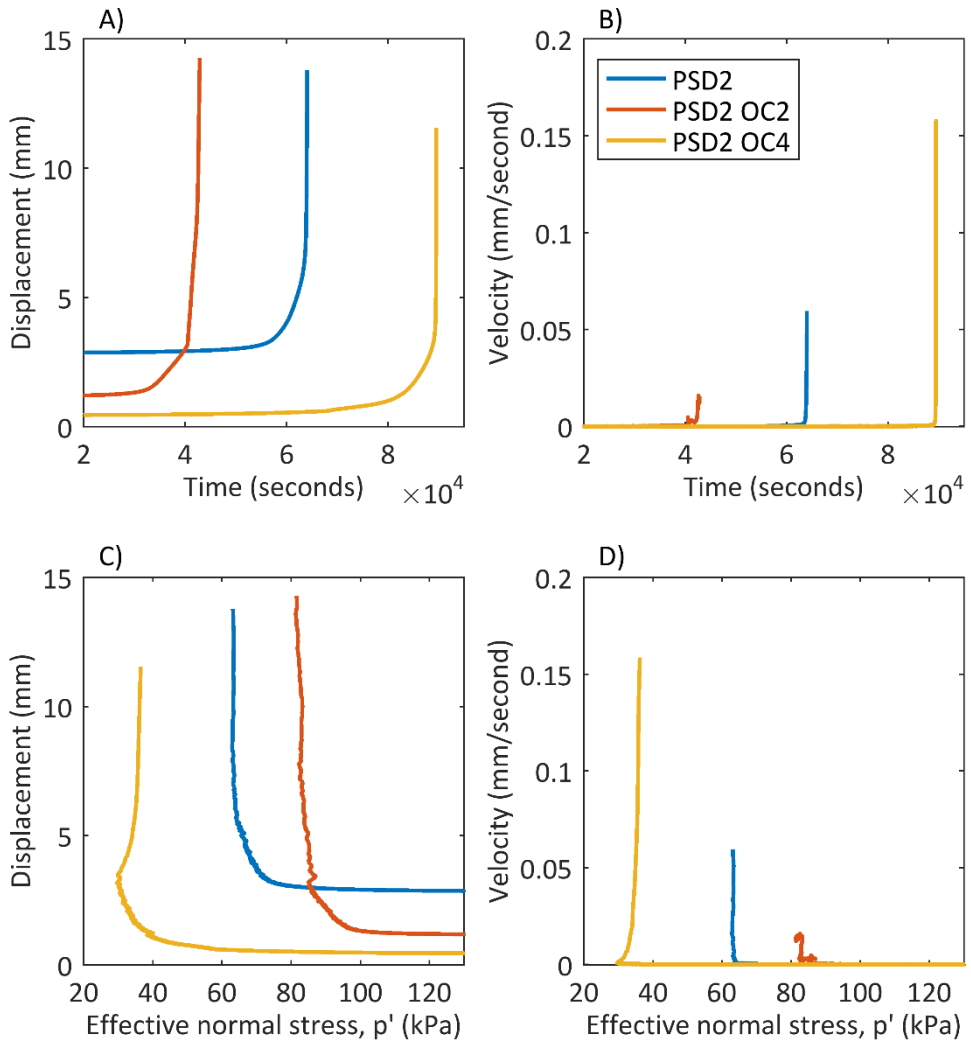

Figure 5.18: Plots comparing the effect of consolidation history on deformation behaviour during linear PPI tests on PSD2 samples. Note: OC2 = over-consolidated ratio of two, OC4 = over-consolidation ratio of four.

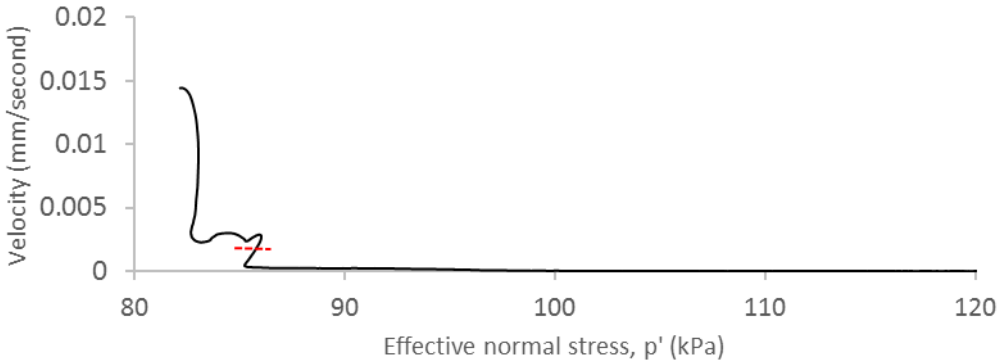

Figure 5.19: Complete velocity profile of the PSD2 OC2 sample during PPI test. Note: An Initial failure occurs, before drainage of the shear surface causes a drop in PWP (increase in p') resulting in the stabilisation of velocity before another failure develops. Red-dashed line indicates sample drainage following initial failure.

The normally consolidated PSD2 sample initially displays a fluctuating asymptotic trend in 1/Velocity-time space, before transitioning to a smoother asymptotic trend for

the majority of its deformation. Just prior to the conclusion of the test, the sample exhibits a very minor period of linearity. The PSD2 OC2 sample displays a very similar trend to that of the PSD2 sample, characterised by an initially fluctuating asymptotic trend which evens out before a short period of linearity prior to failure. The 1/Velocity trend exhibited by the PSD2 OC4 sample is substantially different to the others, initially displaying a slightly asymptotic, but highly fluctuating 1/Velocity trend, before evolving into a linear trend after ~88,300 seconds. This period of linearity prior to failure is much longer than those that occurred in the PSD2 and PSD2 OC2 samples. To better understand these trends observed in 1/Velocity-time space, a regression analysis was undertaken to emphasise the appropriateness of the trends and reveal their closeness of fit.

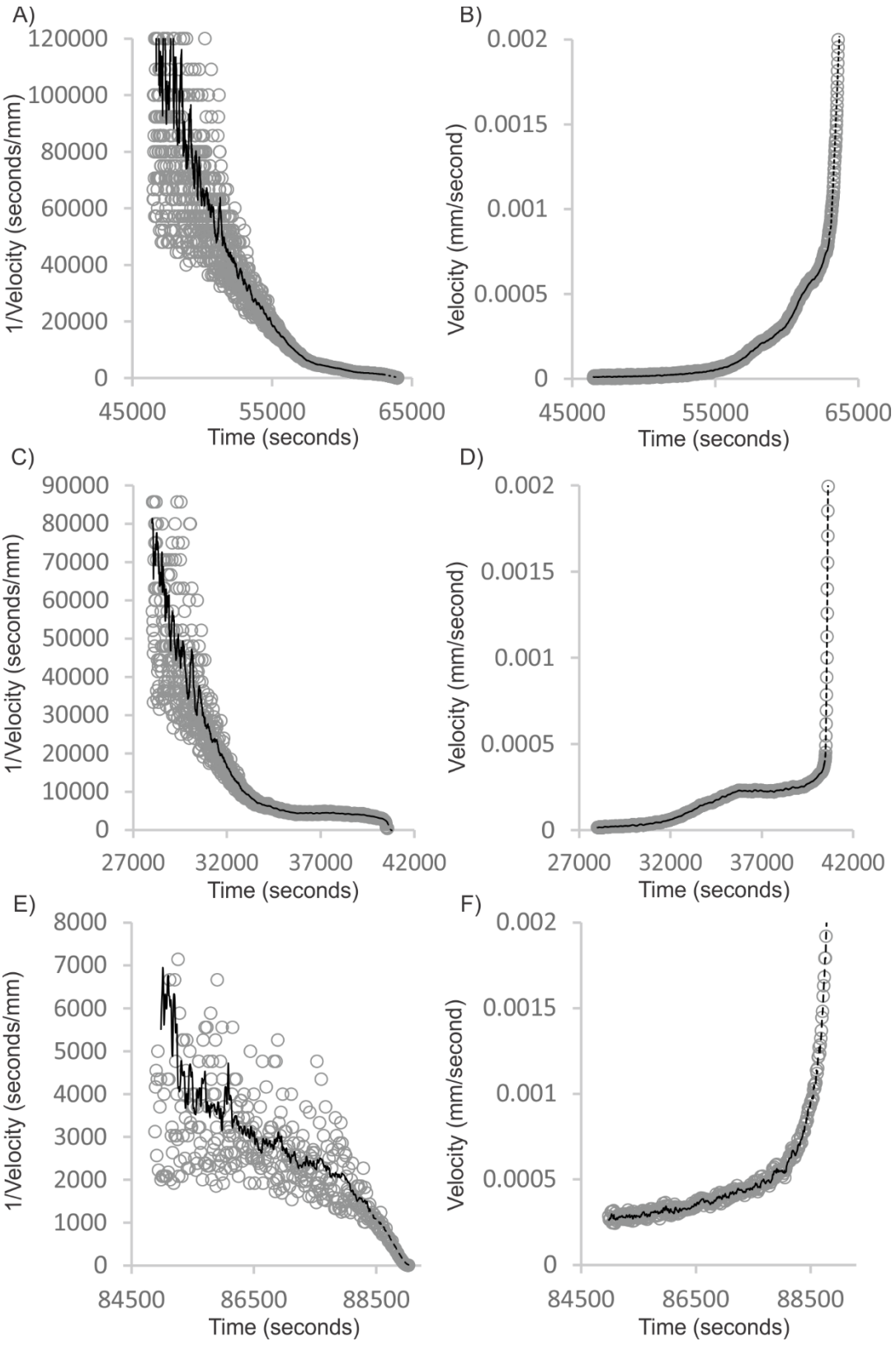

Figure 5.20: Deformation behaviour of the three PSD2 materials with different consolidation histories. A) & B) PSD2, C) & D) PSD2 OC2, E) & F) PSD2 OC4. Note: Grey circles = raw data, black lines = averaged data; black-solid lines = asymptotic trend in 1/Velocity – time space, black-dashed = linear trend in 1/Velocity – time space.

Figure 5.21 displays the best-fit lines of the periods preceding failure in 1/Velocity-time space, while Table 5.4 presents the statistical significance of those fits, as well as the fit of other models.

The regression analysis demonstrates that the PSD2 sample displays the closest fit to an asymptotic trend, with the data showing a high correlation with both a power law (R^2 =0.9625) and exponential model (R^2 =0.9736) (Figure 5.21 A). Similarly, the PSD2 OC2 sample also displays a strong correlation to both a power law (R^2 =0.9217) and exponential model (R^2 =0.8981), indicating a strong asymptotic trend (Figure 5.21 B). In contrast, the PSD2 OC4 displays a much closer correlation to a linear model (R^2 =0.9031), than either the power law or exponential models (R^2 = 0.6490 and 0.6524 respectively) (Figure 5.21 C). This indicates a much more linear trend is exhibited by the PSD2 OC4 sample during PPI testing, as indicated previously.

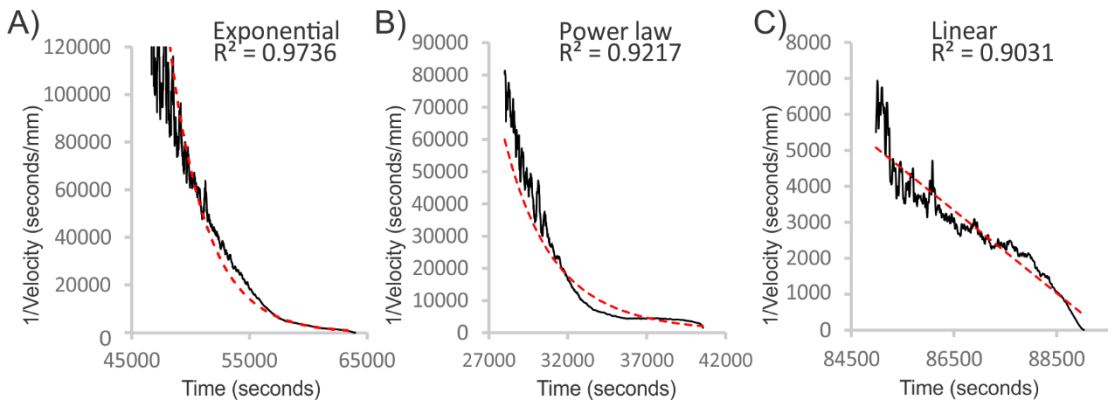

Figure 5.21: Regression analysis of the failure behaviour in linear PPI tests on samples with different consolidation histories displaying best fit line for each test. A) PSD2, B) PSD2 OC2, C) PSD2 OC4. Black-solid line represents averaged data, red-dashed line indicates line of best fit.

Table 5.4: Results of regression analysis on pre-failure behaviour in linear PPI tests on samples with different consolidation history, displayed as R-squared values for the functions fitted.

Test	Linear fit	Power law fit	Exponential fit
PPILinear2	0.8112	0.9625	0.9736
PPILinear2 OC2	0.6996	0.9217	0.8981
PPILinear2 OC4	0.9031	0.6490	0.6524

Axial strain data from PPI testing on all PSD2 samples identifies a common trend of sample dilation across all tests (Figure 5.22). The normally consolidated PSD2 sample displayed a continual, hyperbolic decrease in axial strain throughout the entire test,

ultimately undergoing the smallest amount of dilation in response the PPI. Similarly, the PSD2 OC4 sample also displayed a smooth, continual hyperbolic decrease in sample dilation. However, the PSD2 OC4 sample experienced well over double the total amount of dilation as the other two samples. While still dilating for the entire test, the PSD2 OC2 sample revealed a more inconsistent pattern. Initially, the sample experienced a hyperbolic increase in dilation, but is then punctuated by a kink, where an increase in the rate of dilation increases. This kink corresponds to the onset of rapid deformation in the PSD2 OC2 sample (Appendix B, Fig. B6).

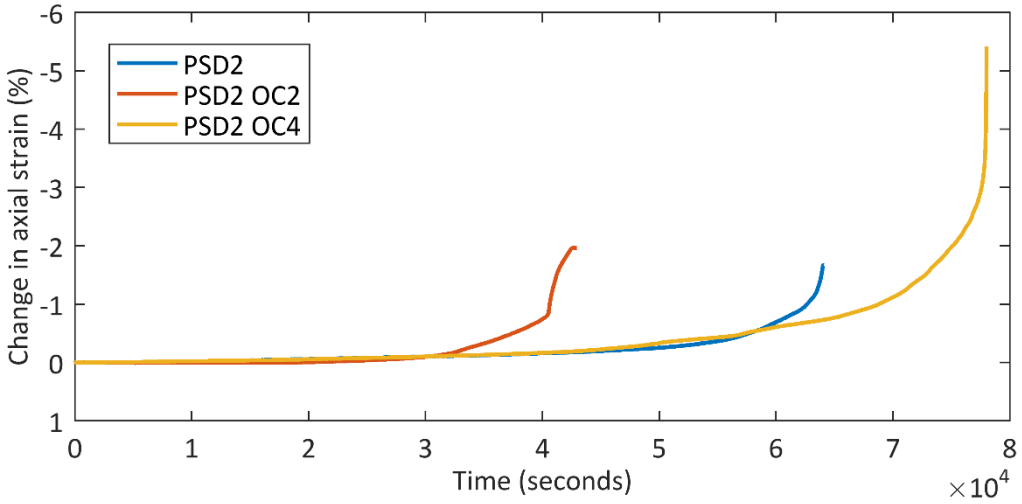

Figure 5.22: Change in axial strain experience by PSD2 samples during PPI testing. Note: an increasingly negative value indicates sample dilation is occurring.

5.3 Summary of key results from DBPSB testing

A series of specialist DBPSB tests were undertaken on samples of fill material taken from the Priscilla Crescent landslide site to study the potential rainfall-induced failure mechanisms.

Rapid shear testing

During rapid direct shear testing, all samples displayed contractive behaviour and were able to generate excess PWPs. The maximum generated PWP, rate of generation, and rate of diffusion were influenced by both the particle-size and consolidation history. The PSD1 material was able to generate the most PWP the quickest, and sustain it for the longest, while the PSD2 sample generated slightly less at a similar rate, but drained much quicker. The PSD3 sample generated the least excess PWP the slowest, and drained them the quickest. Furthermore, increased sample density resulted in the

generation of over three times more excess PWP across all samples, and was also associated with an increased rate of diffusion.

Pore-pressure inflation (PPI) testing

All samples initially experienced a period of zero displacement before the onset of deformation during PPI testing, with the length of the period influenced by both particle-size and consolidation history. Deformation initiated first (at the highest effective stress) in PSD3 and PSD2 samples, while deformation began much later (lowest effective stress) in the PSD1 sample. The OC2 PSD2 sample began deforming before the normally consolidated PSD2 sample, while the OC4 sample began deforming much later.

Once deformation began, samples experienced varying periods of pre-failure deformation, before undergoing final acceleration to failure. Pre-failure deformation was characterised by roughly asymptotic trends in 1/Velocity-time space, before transitioning to a more linear trend leading up to final failure. The relative duration of the asymptotic and linear trends was strongly influenced by both the particle-size and consolidation history of the sample, with all but the PSD1 and OC4 PSD2 samples displaying asymptotic trends for the majority of the deformation period. Contrastingly, both the PSD1 and OC4 PSD2 sample exhibited strong components of linearity in 1/Velocity-time space.

6 Discussion

This chapter combines the specialist laboratory testing results with existing knowledge and literature to develop an understanding of failure mechanisms and post-failure behaviour of fill slopes. The results are first used to evaluate whether liquefaction is a credible failure mechanism in fill materials. The influence of particle-size distribution and consolidation history of fill slopes on failure behaviour are then considered. These interpretations provide new insight into the potential failure mechanisms observed during the recent rainfall-induced fill slope failures in the Wellington Region, and the future hazards they may pose.

Note: during the discussion and conclusions, the samples will be referred to as fine (PSD1), mixed (PSD2), and coarse (PSD3), to better convey the effect of the different particle-size ranges.

6.1 Deformation mechanism: is liquefaction a credible model for failure?

As outlined in Section 2.7, liquefaction is typically characterised as a rapid, fluidised failure caused by a sudden loss in shear strength in response to a rise in pore-water pressure. Although this mechanism has been attributed to many catastrophic fill slope failures (e.g. Bishop, 1973; Take et al., 2004), it was not observed during this study. During all PPI tests movement initiated at very slow displacement rates, indicating a gradual deformation mechanism, consistent with steady-state ductile behaviour observed in other laboratory studies (Ng & Petley, 2009). This observation unequivocally demonstrates that liquefaction was not responsible for triggering failure in any of the samples (Figure 6.1).

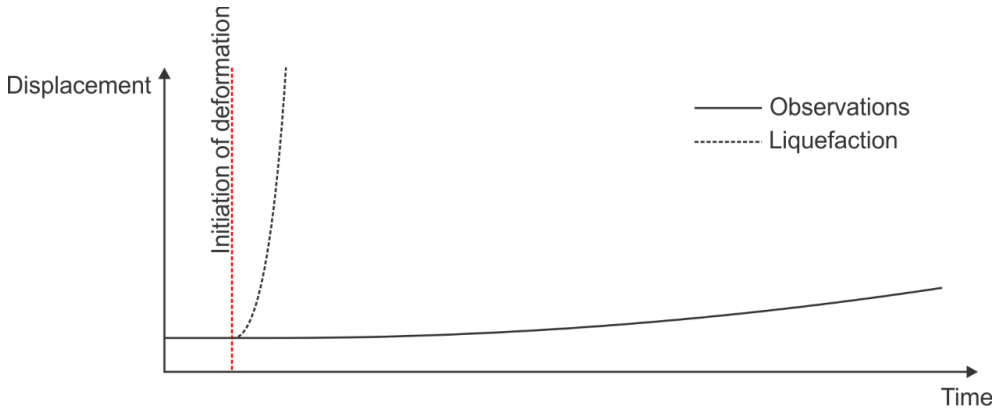

Figure 6.1: Conceptual diagram displaying the difference between the observed deformation behaviour and what liquefaction-induced deformation would look like. Note: observation trend only represents the early stage of observed deformation (Stage 2, Figure 6.2).

During the initial stages of PPI testing, little or no measurable displacement was observed in all samples (Stage 1, Figure 6.2). This behaviour can be interpreted as plastic deformation (Ng, 2007; Selby, 1993), and has previously been observed during laboratory testing studies (e.g. Anderson & Sitar, 1995; Ng, 2007). This behaviour occurs as the stress state during the early period of the tests is inadequate to surpass each materials' yield stress (Selby, 1993). Referring to behaviour at the particle level within this phase, the applied shear stress is likely insufficient to overcome the inter-particle contacts of the material (Ng, 2007). Once this yield stress was surpassed as a result of increasing pore-water pressure, ductile deformation was observed to initiate in all samples (Stage 2, Figure 6.2).

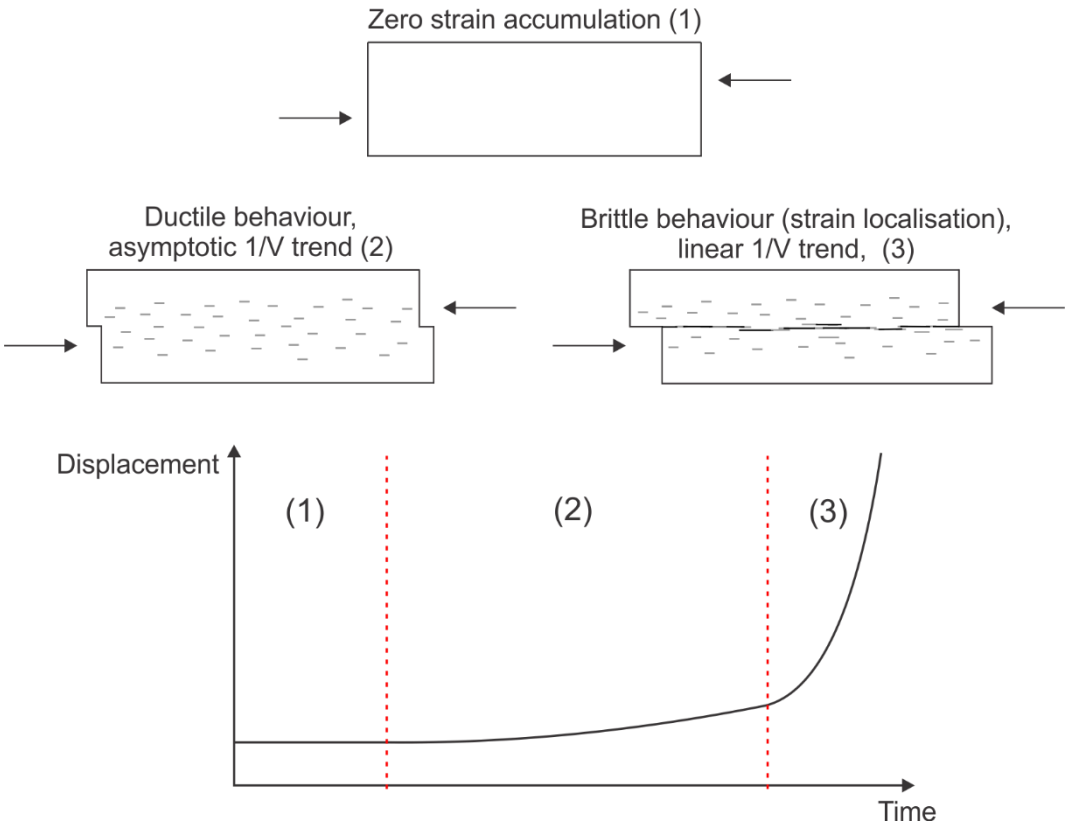

Figure 6.2: Observed stages of failure development during PPI testing. 1), 2), 3) represent different stages of failure development. Note: steady-state deformation (stage 2), is characterised by a constant velocity for a given stress state, however, as the stress state was constantly reducing during PPI testing, we see a slow, constant increase in velocity.

During stage 2, all samples displayed asymptotic trends in 1/Velocity-time space which is characteristic of either ductile deformation or failure along pre-existing shear surfaces (Kilburn & Petley, 2003; Petley et al., 2002). As all samples had not previously been sheared, it suggests that each sample initially experienced a steady-state ductile failure mechanism, where the displacement rate increases to a constant

value for a given stress state. This interpretation is consistent with the behaviour observed in other laboratory testing on remoulded and non-cohesive materials (Ng, 2007). Most samples deformed via this mechanism for the majority of the test, before a final failure was induced by the DBPSB (discussed in more detail in Section 6.2.1). Two samples, however, transitioned from an asymptotic to linear trend in 1/Velocity-time space during the early stages of deformation (Figure 5.15 A; Figure 5.20 E). This transition to linearity indicates that strain localisation occurred within a more focused shear zone, resulting in rapid movements through the development of a shear surface (Stage 3, Figure 6.2). The patterns of movement observed during these tests are consistent with the micro-crack model proposed by Petley et al. (2005) (discussed in Section 2.6.4), which has been demonstrated in both laboratory (Petley et al., 2008) and field (Cooper et al., 1998) studies.

Despite the variation in failure mechanisms observed during the experiments, the progressive movement in each instance indicates that liquefaction did not occur in any of the samples. While liquefaction may not be a credible model of slope failure, however, contractive behaviour and pore pressure responses measured during rapid shear tests suggests that the material could be susceptible to post-failure liquefaction.

During rapid shearing, while displaying slightly varying trends, all samples both contracted and generated excess pore-water pressure. Observing this behaviour is significant, as contractive behaviour in a saturated soil is widely suggested to have an important control on landslide movement behaviour, potentially causing a transition from stable to unstable motion (Schulz et al., 2009). This occurs as soil contraction causes a reduction in pore-space that rapidly increases pore-water pressure, reducing the mean effective stress and enabling a landslide to accelerate rapidly. This landslide failure mechanism has been observed in both laboratory (Okura et al., 2002; Wang & Sassa, 2003) and field studies (Sassa, 2000). Based on these results, it is suggested that one of two fundamentally similar but slightly different mechanisms may facilitate a transition from stable to unstable motion in the fill slopes through either: 1) a dilatancy feedback mechanism, as proposed by Iverson (2005), or 2) a sliding-surface liquefaction mechanism as proposed by Sassa (2000); Sassa et al. (1996).

Both the mechanisms proposed by Iverson (2005) and Sassa (2000) are conceptually similar, and characterised by an initial failure, which can subsequently cause rapid, liquefied landslide behaviour (Figure 6.3). Iverson's proposed dilatancy feedback

model is based on a feedback between shear-surface dilation/contraction and pore-water pressure, as discussed in Section 2.6.3. This model is consistent with laboratory based studies by Iverson et al. (1997) and Iverson et al. (2000), who observed transformations from landslides in a steady state, to rapid, liquefied flows. The requirement of this model is that the initial density state of a soil is below the critical-state density, thus allowing contraction and the consequent evolution in behaviour. Similarly, Sassa's (2000) sliding-surface liquefaction model is based on the premise that an initial failure causes shear-zone contraction resulting in the generation of excess pore-water pressure and a transition to rapid, fluidised failure. However, as discussed in Section 2.7, and contrary to Iverson's dilatancy model, Sassa specifies that shear-zone contraction is caused by shear-induced grain crushing, and does not depend on a soil being below a critical-state density.

Although the results obtained from this study are insufficient to differentiate which of these two mechanisms may operate during failure in the fill samples, both mechanisms and subsequent behaviours are fundamentally the same. This suggests that all samples are susceptible to post-failure liquefaction and consequently, rapid, liquefied failure behaviour. Critically, it is the initial failure which causes liquefaction, and not liquefaction that causes the initial failure.

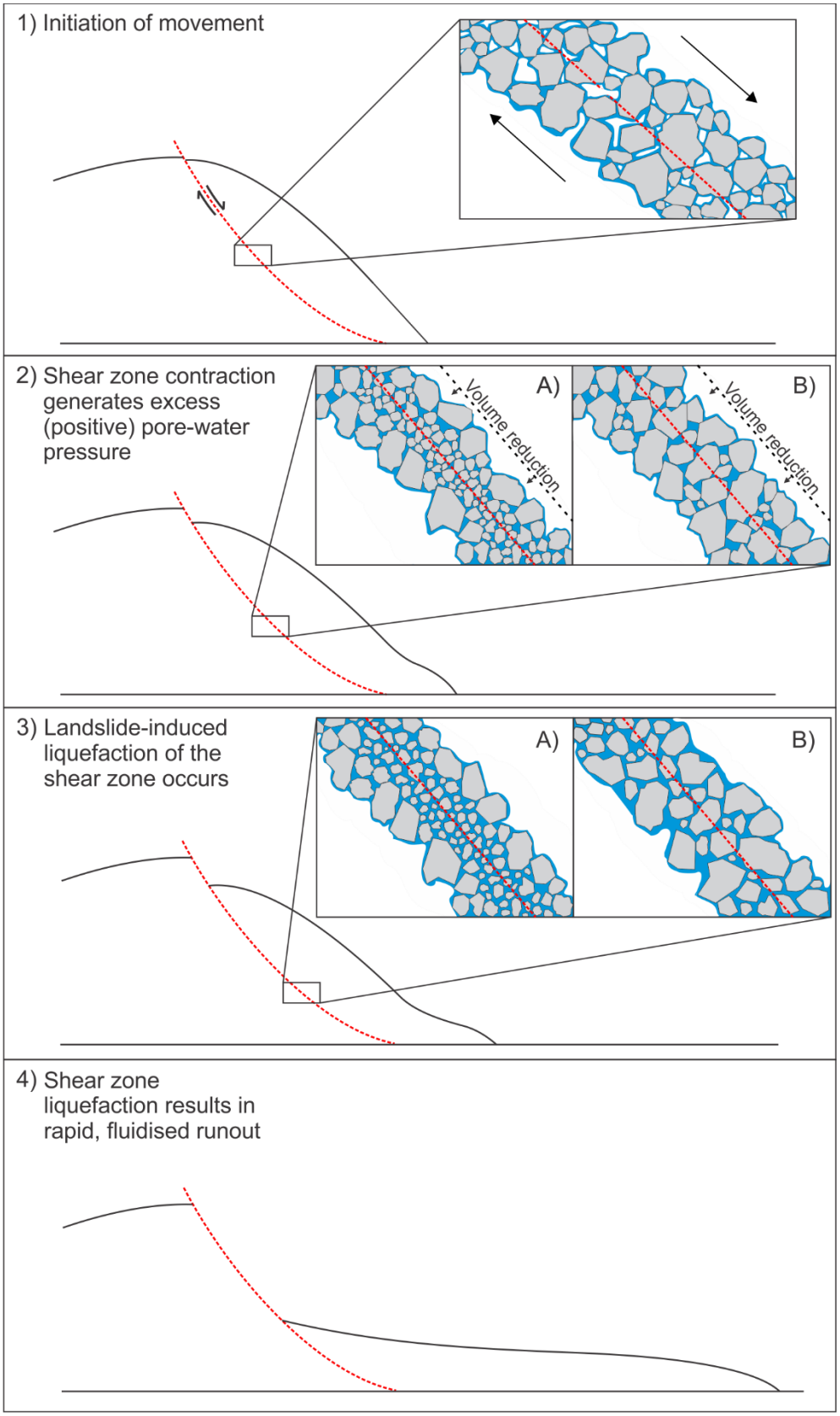

Figure 6.3: Conceptual diagram showing the stages of failure for the suggested landslide-induced liquefaction mechanism responsible for fluidised failure. Note A) specifies sliding surface liquefaction as proposed by Sassa (2000), whereas B) refers to general contraction of the shear-zone as discussed by Iverson (2005).

6.2 The effect of particle-size on movement behaviour

Although similar trends of deformation were observed across the three different sample types, the particle-size distribution clearly influenced both the failure behaviour during PPI testing, and the potential susceptibility to post-failure liquefaction.

6.2.1 Observed movement behaviour

At the beginning of PPI tests, the samples experienced a period of little/no displacement, interpreted as plastic deformation behaviour. Using the initiation of movement as an indication for the yield stress for each of the materials (Selby, 1993), we can observe that particle size influences the effective stress at which deformation initiates. The yield stress for the fine sample is equal to a p' of ~90kPa, the lowest of the three samples, while the yield stress for the mixed and coarse samples were approximately the same at p'≈ 105kPa. These results indicate that the fine and possibly also the mixed samples had cohesive bonds present.

Given the fine material has the lowest effective internal angle of friction (φ') but failed at the lowest effective normal stress suggests cohesion is likely to have been present in the sample. This is not unexpected as electrostatic bonding is found between clay and silt sized particles which are present in the fine material (De Blasio, 2011). The mixed sample also contains clay and silt particles, and failed at approximately the same effective stress as the coarse sample while displaying a slightly lower φ' value, suggesting a small amount of cohesion may also have been present. This behaviour indicates that the mixed and coarse samples are the most susceptible to pore-water pressure induced failure as they require the smallest reduction in effective normal stress to initiate deformation, while the fine sample requires a greater decrease in effective stress to initiate failure.

Once the effective normal stress was low enough to overcome each materials yield stress, deformation was observed. In all samples, this was characterised by ductile deformation behaviour, as identified by the asymptotic trend in 1/Velocity-time space (Figure 5.15). This ductile deformation continued until the asymptotic trend in 1/Velocity-time space progressed to a linear trend indicating the onset of brittle deformation. The occurrence of this transition, however, varied considerably between samples. This change from asymptotic to linear form in 1/Velocity-time space is best illustrated by plotting *log* 1/Velocity against time, where an asymptotic trend will appear linear, and linearity will be demonstrated by a downward arcing line.

In the fine sample, a transition in behaviour from a ductile to brittle deformation style was observed relatively early in the test and is best illustrated in log 1/Velocity-time space (Figure 6.4 A). This suggests that only a small amount of ductile deformation occurs in the sample before strain localisation occurs and more rapid failure is induced. This behaviour is consistent with the previous experiments on cohesive soils which have been interpreted as a brittle deformation (Carey & Petley, 2014; Petley et al., 2005). Brittle deformation occurs as a reduction in the effective stress leads to micro-crack development proximal to the future-shear surface, which with a continual decrease in the effective stress culminates in the formation of a complete shear-surface and brittle failure (Carey & Petley, 2014; Petley et al., 2005).

Conversely, the transition to the linear trend in both the mixed and coarse samples is not observed until much later in the test (~17,000 and 23,000 seconds), after the onset of ductile deformation at ~46,500 and ~43,500 seconds respectively (Figure 6.4 B & C). This indicates that ductile deformation is the dominant mechanism acting during failure in those samples, and that observing linearity late in the deformation period is likely the product of the method. The direct shear nature of the DBPSB forces deformation to occur along a discrete shear zone towards the conclusion of the test, as displacing the lower half of the sample chamber relative to the top will eventually compel deformation to occur along the specified shear zone (Figure 6.5).

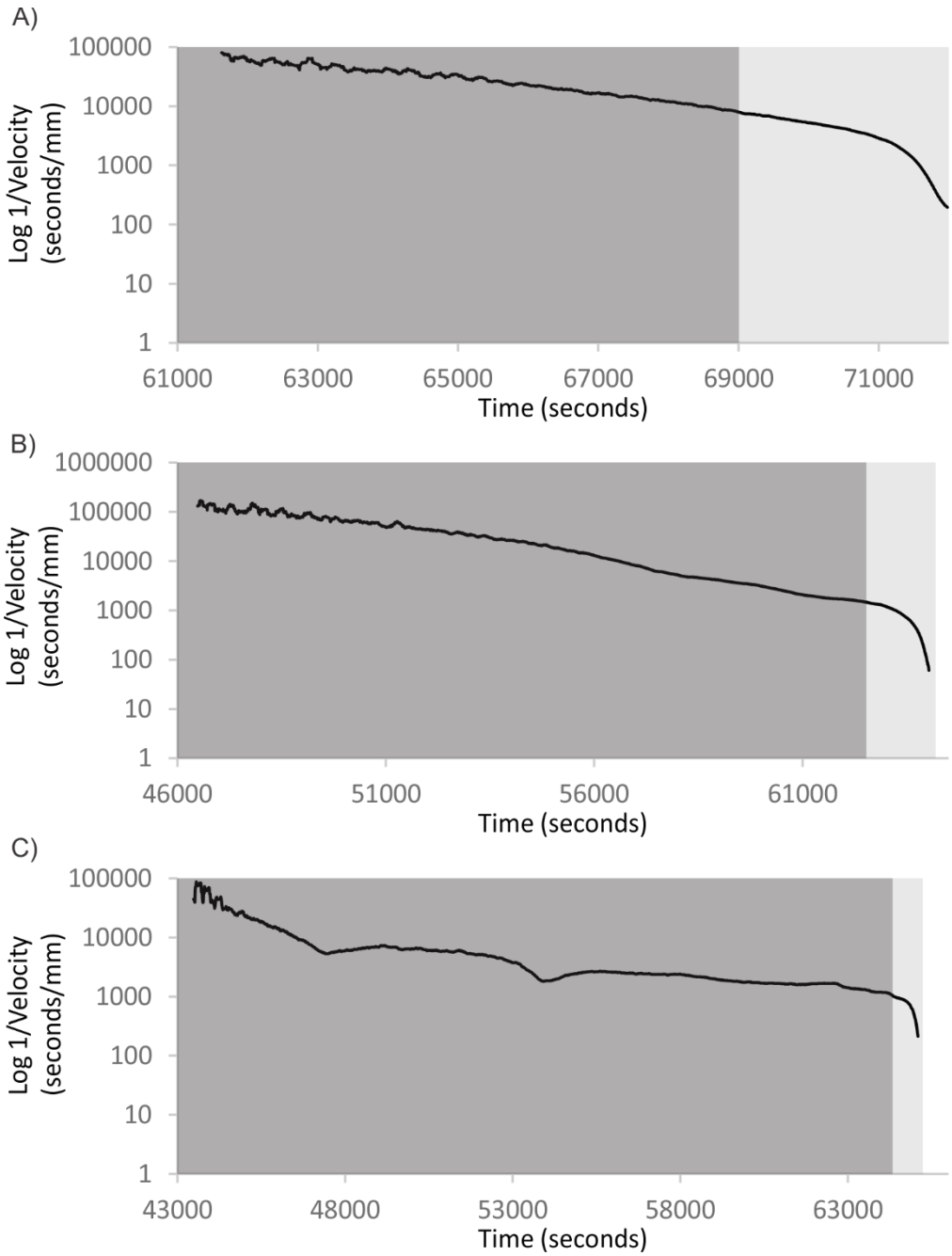

Figure 6.4: Investigating stages of asymptotic and linear trends of 1/Velocity – time space during PPI testing on different PSD samples. A) fine, B) mixed, C) coarse. Dark grey shading highlights asymptotic form, light grey highlights linear form. Note in a log plot of 1/Velocity – time, an asymptotic trend will appear as a linear line, whereas a linear trend will be indicate by a downward curving line.

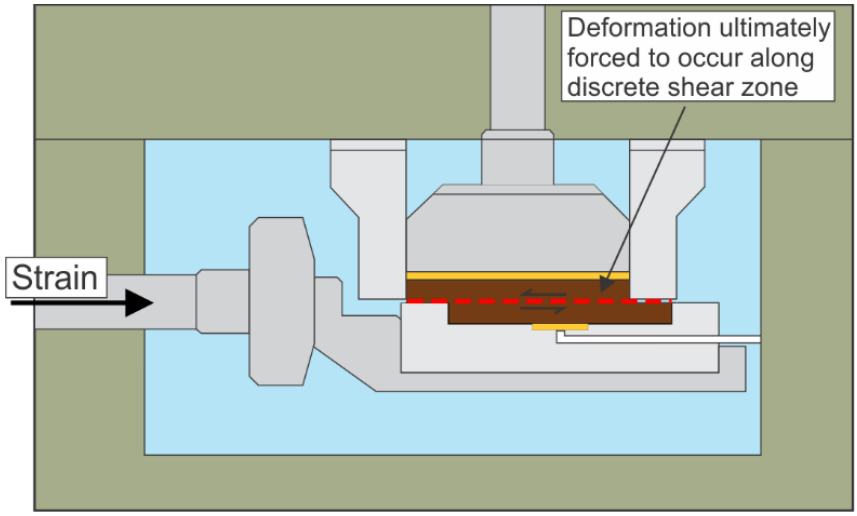

Figure 6.5: Final position of a sample in the DBPSB displaying how strain is induced in direct shear. Note the design of the apparatus ultimately forces deformation along the shear zone. Figure modified from Brain et al. (2015).

Secondly, the ability of strain to concentrate in the fine material relatively soon after deformation begins, suggests that the fine particle-size allows strain to localise much more easily than a coarse particle-size. Additionally, the presence of coarse particles in the mixed (and coarse) sample retards the localisation of strain. Normalising the 1/Velocity and time data further helps evaluate the different trends by creating scales that enable the trends to be overlain (Figure 6.6).

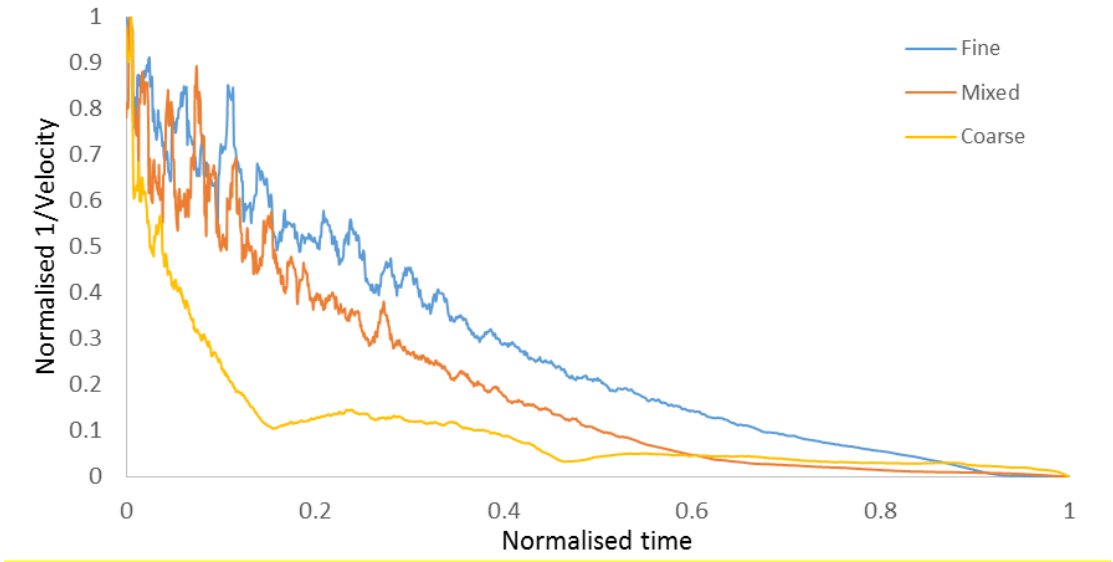

Figure 6.6: Normalised 1/Velocity and time data comparing the shapes of the 1/Velocity trends obtained from PPI testing on different PSD samples.

Figure 6.6 reveals that the shape of the curves for the fine and mixed samples are very similar and may indicate that the fine particle content in those samples has a dominant role during deformation. The fine and mixed asymptotic trends are broadly consistent

for most of the test and only diverge as the fine sample starts to display linearity, while the mixed sample maintains an asymptotic trend. This further reiterates the interpretation that the presence of coarse particles in the mixed material is prohibiting the localisation of strain to a more confined shear zone.

Interestingly, these results imply that while the mixed and coarse materials are the most susceptible to rainfall-induced failure, landslides in these materials will likely exhibit ductile movement behaviour, where velocities accelerate to a constant value for a given stress state. On the other hand, the fine material appears to be less susceptible to rainfall-induced failure, however, the results indicate that it could be more prone to rapid accelerations to failure.

Although the coarse material displayed ductile failure behaviour, the trend is significantly different to both the mixed and fine samples. This reflects the spikes in displacement rate that were experienced as deformation developed (Figure 5.15 F), similar to the stick-slip movement type suggested by Allison and Brunsden (1990). A key difference, however, is that in this case, the periods of episodic increases in movement rate are interspersed with continuous displacement instead of zero displacement. As noted in Section 5.2.4, these spikes correlate well with changes in the axial strain occurring (Appendix B, Fig. B4). The results demonstrate that as the velocity begins to increase, sample dilation also accelerates. This is then followed by a reduction in the velocity back towards the typical trend, mirrored by a subsequent fall in dilation rate. This behaviour strongly suggests a negative feedback mechanism, such as the one proposed by Iverson (2005), between sample dilation and pore-pressure is operating in the coarse sample that ultimately hinders runaway acceleration. This feedback has been observed in both field (Schulz et al., 2009) and laboratory (Moore & Iverson, 2002) studies. As the movement rate accelerates due to rising pore-water pressures, sample dilation accelerates, which can cause either the pore-water pressure to reduce, or the rate of pore-water pressure increase to slow. This impedance to the system ultimately acts to arrest accelerating movement. Once the pore-water pressure is able to sufficiently develop again, the same process can then occur. This implies that the coarse material is also susceptible to an episodic style of landslide movement, similar to the stick-slip movement type proposed by Allison and Brunsden (1990), and to that observed by Schulz et al. (2009) in the Slumgullion landslide in Colarado, USA.

6.2.2 Influence on potential post-failure liquefaction

While all samples displayed contractive behaviour and a subsequent predisposition to rapid, fluidised failure, they also displayed differing characteristics which imply their susceptibility likely varies considerably (Figure 5.10). Crucially, each sample generated differing amounts of excess pore-water pressure in response to shearing, and similarly showed different rates of pore-water pressure dissipation.

The fine material generated the most excess pore-water pressure, generated it the quickest, and also sustained it for the longest period. The mixed material generated only slightly less than the fine sample at a similar rate, however dissipated it much quicker. And the coarse material generated the least, and dissipated it the quickest. These results are consistent with the behaviour observed by Wang and Sassa (2003), and indicate the significant control particle-size has on pore-water pressure generation and dissipation behaviour. These differing behaviours can most likely be attributed to the different permeability of the samples (Iverson & LaHusen, 1989; Iverson et al., 1997; Wang & Sassa, 2003).

As shown by Iverson and LaHusen (1989) and Iverson et al. (1997), the pore-water pressure generated by a landslide is predominantly controlled by the landslide velocity and deformation, as well as the permeability of the landslide material. Suggesting, that given the same conditions, a landslide comprised of a less permeable material will generate greater excess pore-water pressures when compared to a landslide with greater permeability, as the greater permeability allows for more efficient drainage (Wang & Sassa, 2003). Given this, and the consistent conditions used during testing, it is reasonable to assume that the fine material is the least permeable of the three samples, closely followed by the mixed, while the coarse material is the most permeable; consistent with the current understanding of the influence of grainsize on permeability (e.g. Beard & Weyl, 1973; Shepherd, 1989; Terzaghi et al., 1996). These differing behaviours have significant implications for the possibility of landslide-triggered liquefaction in the materials, and are ultimately associated with the ability of pore-water pressure to enhance landslide mobility by facilitating flow-like behaviour (e.g. Legros, 2002; Schulz et al., 2009).

Critically, if excess pore-water pressure is able to persist, or is generated during landslide motion, a transition from a stable, to a more unstable type of movement can occur (Iverson, 2005; Iverson et al., 1997; Legros, 2002; Schulz et al., 2009). This

being said, a material which either: 1) is able to generate greater amounts of pore-water pressure, or 2) sustain generated pore-water pressures for longer, will therefore be more susceptible to unstable motion. This suggests that the fine and mixed samples are more predisposed to post-failure liquefaction than the coarse sample, as they are able to generate greater pore-water pressures and/or sustain them for longer. This finding is consistent with the results of other laboratory based testing such as the work by Wang and Sassa (2003) and Okada et al. (2004), who both found a similar relationship between permeability and susceptibility to flow-like behaviour.

Specifically, the findings made by Wang and Sassa (2003) strongly support the results obtained in this study, regarding the effect of particle-size on pore-water pressure generation and dissipation. Furthermore, the work by Wang and Sassa also provides a clear link to the consequence on potential landslide movement behaviour. Utilizing a flume device to simulate rainfall-induced landsliding on silica sand samples with different particle-size distributions and fine-particle contents, Wang and Sassa (2003) found that a coarse sand had a tendency to fail retrogressively, while a finer sand exhibited more rapid flow-slide behaviour, offering three key reasons as to why: 1) the finer silica sand was able to generate greater pore-water pressure during failure, 2) the coarser silica sand dissipated the generated pore-water pressure quicker due to its greater permeability, and 3) the finer sand is more likely to float due to the smaller grainsize.

The results from this study clearly support existing literature in highlighting how the relationships between landslide initiation mechanism and the generation and dissipation of pore-water pressures are fundamental controls on landslide mobility. Fill slopes with a large difference between the rate of pore-water generation and dissipation with have higher susceptibility to fluidised failure behaviour and higher mobility, while fill slopes with either a small, or no difference will have low mobility and are less likely to be susceptible to fluidised failure.

6.3 The effect of consolidation history on movement behaviour

The consolidation history was also found to have an influence on the initiation of deformation, the pattern of deformation, and also how the samples generate and sustain pore-water pressure. This indicates that fill slope compaction has a strong control on the potential failure mechanisms and landslide behaviour.

6.3.1 Observed movement behaviour

Consistent with the normally consolidated sample, both the OC2 and OC4 samples initially experience a period of little/no displacement, indicating the samples may be behaving as a plastic material (as discussed previously) (Selby, 1993). The yield point, however, differed between samples, indicating rainfall-induced landslide deformation initiates under different conditions depending on the density of the material. The normally consolidated mixed sample had a yield stress of p' ≈ 105kPa, while the OC2 and OC4 mixed samples had yield stresses of p' ≈ 120 and 65kPa respectively. This suggests that the OC2 sample was weakest of the three samples. OC4 was significantly stronger.

It was anticipated that over-consolidating the samples would increase the shear strength, as greater consolidation produces a denser sample, which results in an increase in the internal angle of friction as the inter-particle contacts strengthen (Terzaghi et al., 1996). The relationship between the internal angle of friction and shear strength is shown in Equation 2.3. While this explains why the OC4 sample is the strongest of the three materials, it does not explain why the OC2 sample was able to deform at the highest effective normal stress. It is likely this behaviour is observed because sample OC2 did not consolidate a significant amount more than the normally consolidated sample (Figure 5.4 C). In comparison, during consolidation, the OC4 sample experienced 12% more axial strain than the normally consolidated (Linear PPI) sample, while the OC2 sample only experienced 2% more. These results suggest that the amount of consolidation experienced by the OC2 sample was not sufficiently different to that experienced by the normally consolidated sample, and suggests that the sample physical properties were not significantly different. Furthermore, as the OC2 sample was weaker, sample variability has likely also played a role. Once the yield stress was surpassed, deformation behaviour was analogous to that observed in PPI testing on the different particle-size samples, initiating via a ductile mechanism.

Deformation initiates in the normally consolidated and OC2 samples as a ductile mechanism after ~46,500 and 28,000 seconds respectively, displayed strong asymptotic trends in 1/Velocity-time space. This behaviour carries on for the majority of the deformation period (~17,000 and 12,000 seconds respectively), before transitioning to a linear trend just prior to the conclusion of the test (Figure 5.20; Figure 6.7 A & B). This suggests that the dominant failure mechanism operating in

both samples is ductile, while observing linearity so late in the deformation period may be a product of the testing method (discussed in Section 6.2). The similarity in the observed failure behaviour between these two samples is consistent with the earlier notion that the OC2 sample did not consolidate to a significantly different state to that of the normally consolidated sample. This interpretation is further supported by the similarity of the normalised 1/Velocity-time curves (Figure 6.8), which show the OC2 and normally consolidated samples exhibit relatively similar behaviours, while the OC4 sample displayed a significantly different trend.

The deformation behaviour of the OC4 material is significantly different than that of the normally consolidated and OC2 mixed samples, displaying a much greater component of linearity in 1/Velocity-time space. Initially, the OC4 sample displays a broadly asymptotic trend consistent with ductile deformation. However, unlike the normally consolidated and OC2 samples, this asymptotic form becomes linear at a much earlier stage of deformation, only ~3,500 seconds after ductile deformation initiates at the 85,000 second mark (Figure 6.7 C). This indicates that strain is concentrating and coalescing in a more confined shear zone, suggesting shear-surface development and brittle failure is occurring. Failure via this mechanism is ultimately responsible for the rapid acceleration to failure observed.

These results illustrate that significant over-consolidation results in brittle deformation, while normal consolidation of remoulded materials results in ductile deformation. This finding is consistent with similar findings made elsewhere (e.g. Carey & Petley, 2014; Hatibu & Hettiaratchi, 1993; Petley et al., 2005), and in particular, correlates well with the observation that failures in over-consolidated clays are characterised by deformation occurring along discrete shear bands due to strain localisation (Palmer & Rice, 1973; Viggiani et al., 1994).

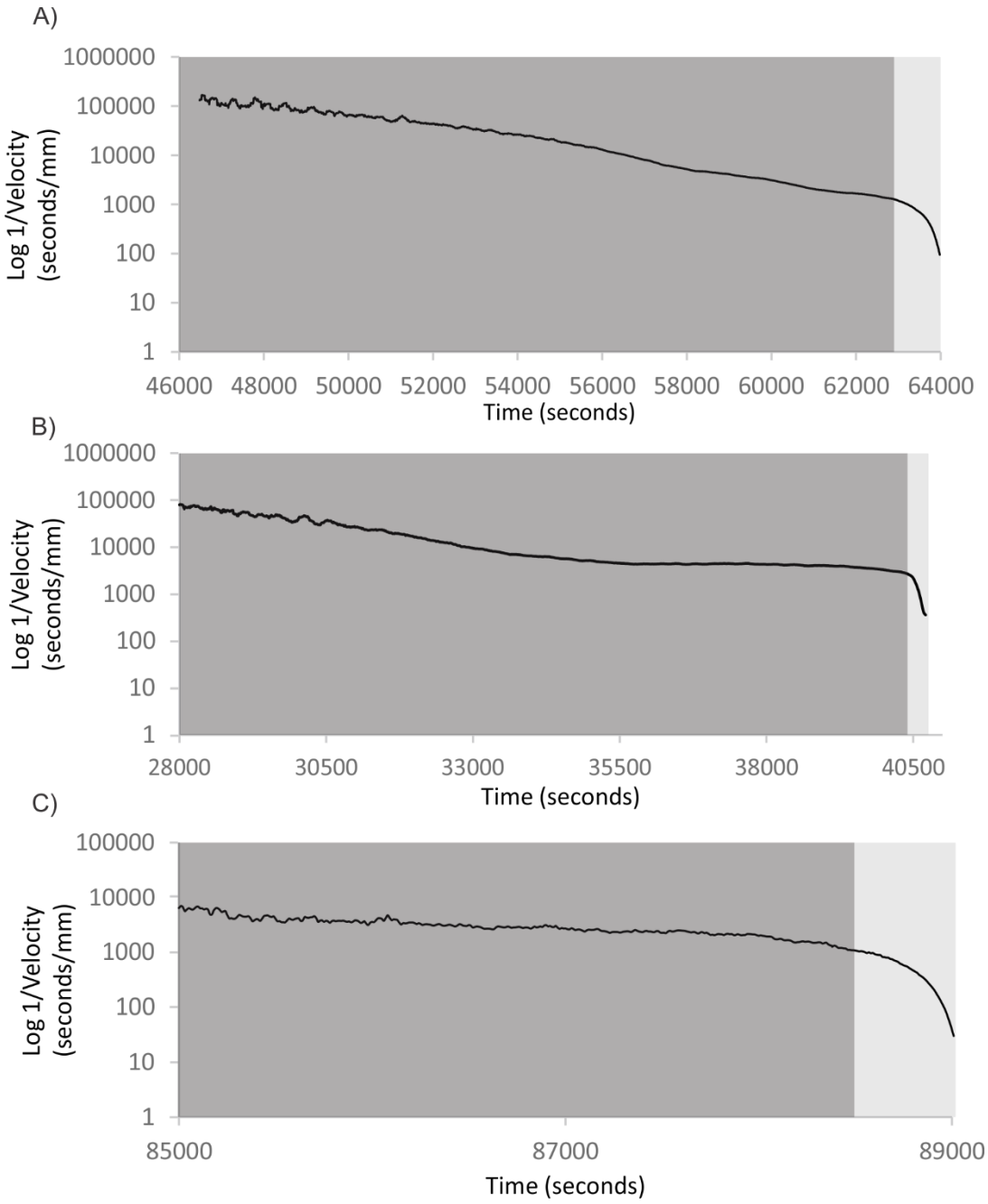

Figure 6.7: Investigating stages of asymptotic and linear trends of 1/Velocity – time space during PPI testing on samples with different consolidation history. A) mixed, B) mixed OC2, C) mixed OC4. Dark grey shading highlights asymptotic form, light grey highlights linear form. Note: in a log plot of 1/Velocity – time, an asymptotic trend will appear as a linear line, whereas a linear trend will be indicate by a downward curving line.

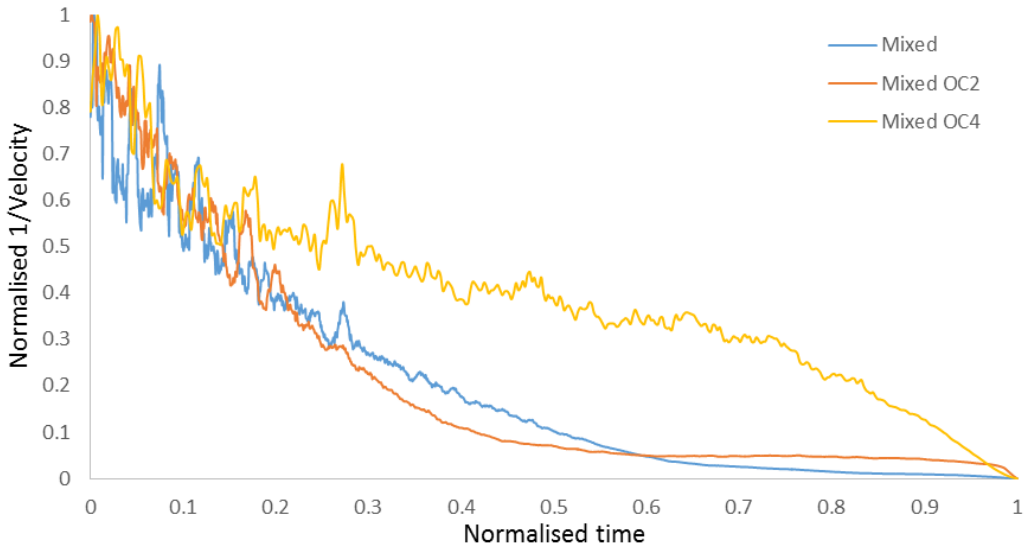

Figure 6.8: Normalised 1/Velocity and time data comparing the shapes of trends observed in 1/Velocity-time from PPI testing on samples with different consolidation history.

These interpretations imply that the consolidation history of fill slopes will have a significant impact on the mechanisms of landslide movement and failure behaviour. The normally consolidated and OC2 mixed samples, which consolidated to similar states, are the most susceptible to rainfall-induced failure as they failed at the highest effective normal stress. However, while they are the most susceptible to failure, they both displayed a ductile failure mechanism. This indicates steady-state failure behaviour, where landslide velocity increases towards a constant value for any given stress state. Contrastingly, the OC4 mixed sample is the least susceptible of the three samples to rainfall-induced failure, owing to the significantly greater sample density and resulting increase in shear strength. Although, when failure was induced in the sample, it was characterised by brittle failure. This indicates that the OC4 mixed sample is prone to rapid failure behaviour, and could poses a much greater hazard in certain conditions.

6.3.2 Influence on potential post-failure liquefaction

Results from rapid shear testing suggest that consolidation history may also have an influence on the susceptibility of the material to post-failure liquefaction, as it was observed to influence the pore-water pressure generation and dissipation characteristics of the three different particle-size samples.

All samples consolidated during the first rapid shear test, indicating that they had increased in density during the first shear (Figure 5.11). During the second rapid shear stage, all three samples generated at least three times more excess pore-water pressure

than in the first test, with the rate of pore-water pressure generation and dissipation also increasing (Figure 5.10). Both the amount of excess pore-water and the rate of increase is likely the result of changes in the physical properties of the samples altered by further consolidation. Specifically, it is expected that the increased density of the sample would have acted to reduce the permeability (e.g. Terzaghi et al., 1996; Wang & Sassa, 2003). As discussed in Section 6.2.2, this reduction in permeability would explain the observed increase in excess pore-water pressure generation and also the increased rates at which they were generated. However, the decrease in sample permeability would also be expected to decrease the rate of dissipation, yet the drainage rate was observed to increase significantly in all samples. This suggests that a more efficient drainage path developed inside the samples, which could be the result of two factors.

Firstly, as a result of the method, the sample had already been sheared prior to the second rapid shear test. This means that a shear surface/zone and preferential drainage paths had already been developed within the sample. As a result, when the second rapid shear test took place, the excess pore-water generated would have more readily been able to drain from the shear surface/zone through the already well-established drainage paths. Furthermore, in Section 6.3.1, it was suggested that increased sample density resulted in strain localisation within a discrete shear zone. Applying the same reasoning, that increased density allows greater strain localisation, may also have contributed to the increased rate of diffusion. Strain localisation in the denser samples may have helped develop a more defined shear zone and better connected drainage paths, which again may allow excess pore-water to drain more rapidly from the shear zone. While this drainage is possible in the DBPSB, it is likely in a landslide that (approximately) undrained conditions would exist, so the rapid diffusion observed in the test may not occur.

The inferences made here, suggest that the consolidation history of a slope is likely to have a strong influence on the potential for post-failure liquefaction to occur. Importantly, as discussed previously (Section 6.2.2), soil material that is able to generate greater excess pore-water pressure, or sustain it for longer, is more likely to develop into rapid, fluidised landslide. As such, the increase in sample density, and resultant reduction in permeability observed during rapid shear testing indicates that the slopes that have experienced more consolidation are more prone to develop into a

rapid, fluidised failure via either of Iverson's (2005) or Sassa's (2000) mechanisms. However, it should be noted that it is widely accepted that a critical-state soil density exists (as briefly mention in Section 6.1). Whereby, a soil that's density state is above that material's critical point (i.e. is denser than), will experience sample dilation rather than sample contraction (e.g. Iverson, 2005; Iverson et al., 2000; Schulz et al., 2009). This dilation would, in turn, act to retard landslide movement through a reduction in pore-water pressure.

Crucially, this provides an important stipulation for the potential development of fluidised failure via Iverson's proposed mechanism. Although the increased density of the samples during the second rapid shear test meant they were more likely to develop into a fluidised failure, it is not correct to say that increasing sample density leads to increased susceptibility to fluidised failure. This is because once the density state is above the critical value, sample contraction is replaced by sample dilation, and the potential for fluidised failure decreases markedly as dilation acts to reduce the pore-water pressure. Furthermore, studies such as those by Wang and Sassa (2001) and Wang and Sassa (2003) illustrate that an optimal density index exists for maximum pore-water pressure generation post-failure. This optimal value varies for every material type, however, represents a density value at which the greatest amount of pore-water pressure is generated. As the sample density decreases from this value, the ability to generate excess pore-water pressure during shearing reduces. Likewise, as the density increases from the optimal value towards the critical value, and the propensity for sample contraction to occur decreases, the ability to generate excess pore-water pressure also reduces (Figure 6.9).

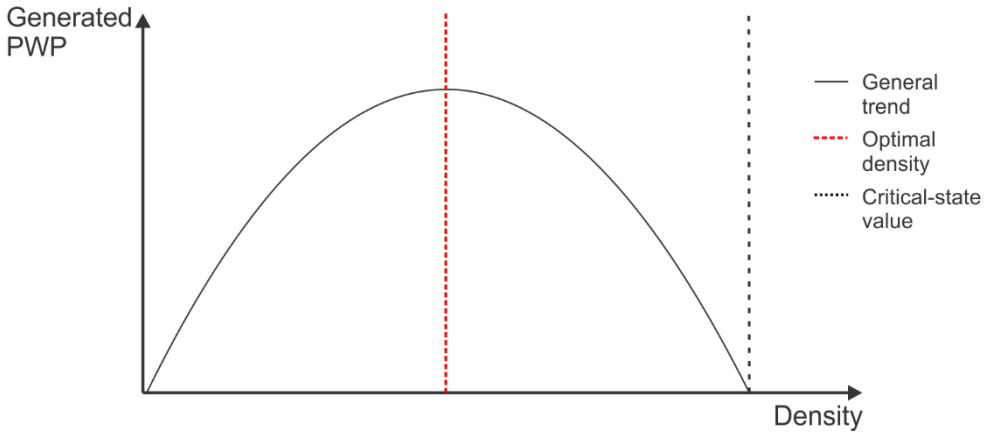

Figure 6.9: Conceptual diagram displaying relationship between sample density and pore-water pressure generation.

On the other hand, with regards to Sassa's (2000) proposed mechanism, as long as grain-crushing and consequent shear-zone contraction can still take place, these results suggest that increasing the sample density will likely increase the susceptibility to post-failure liquefaction.

6.4 Implications for Wellington's fill slopes

As described in Section 3.2, there have been several significant landslides since 2006 which have raised concerns of the susceptibility of some of Wellington's fill slopes to rainfall-induced, rapid, fluidised failure. The 2013 and 2017 failures in the Wellington suburb of Kingston, and the 2006 failure in the Lower Hutt suburb of Kelson, all displayed fluidised failure characteristics, analogous to some catastrophic failures observed globally (Figure 3.6). These failure behaviours signalled that liquefaction is a plausible mode of failure, and would be consistent with findings from many catastrophic, rainfall-induced fill slope failures (e.g. Bishop, 1973; Hungr et al., 2002). Although the results from this study demonstrate that liquefaction is unlikely to be the triggering mechanism responsible for these failures, testing demonstrated that excess pore-water pressures can develop during rapid shearing.

Therefore, the most credible mechanism for explaining the recent fluidised failures in Wellington's fill slopes is progressive failure where post-failure liquefaction of the shear zone occurs, consistent with the findings made by others (e.g. Iverson, 2005; Okada et al., 2004; Sassa, 2000; Schulz et al., 2009; Wang & Sassa, 2003). This identification has important implications, as it provides practitioners with new insight that can aid their ability to identify those slopes that are susceptible to failure, consequently allowing them to develop the most effective management practices to mitigate their future hazard.

Based on a geomorphic analysis of the three fill slope failures, convergent topography, such as gully-heads and other topographic hollows, develop the most vulnerable conditions. This is due to the potential for high permanent water tables resulting from groundwater concentration, or the increased likelihood for saturated conditions to develop during rainfall events owing to the localisation of drainage. Additionally, for a fill slope to be susceptible to post-failure liquefaction, the fill material must contract upon shearing. This stipulates that the fill must either, 1) be susceptible to grain-crushing and/or the breakdown of aggregates, or 2) be in a density state below the critical-state value so that sample contraction can occur.

Based on the necessary conditions, two mitigation strategies can immediately be suggested. Firstly, consolidation of the fill material beyond the critical-state density value may help mitigate the potential for shearing-induced contraction. However, as grain-crushing may have been responsible for the behaviour observed during rapid direct shear testing, this should not be the only measure employed without further research. The best mitigation approach is likely through effective slope drainage in vulnerable locations. Specifically, ensuring that drainage in fill slopes located in convergent topography is sufficient, so that high permanent water tables are not present, and that saturated conditions are unable to readily develop during heavy rainfall.

7 Conclusions

This study has investigated mechanisms of rainfall-induced failure in fill slopes through a series of specialist tests carried out using a dynamic back-pressured shear box. Patterns of displacement and pore-water pressure response identified potential mechanisms of failure development for Wellington's fill slopes.

The results demonstrate that both the consolidation history and particle size composition of fill slopes have a significant influence on shear surface formation. Non-cohesive and normally-consolidated material begins deforming in response to the lowest pore-water pressures and has a tendency to display ductile failure behaviour. This indicates that although the non-cohesive and normally consolidated material is the most susceptible to rainfall-induced failure, it will display steady-state, less rapid failure behaviour.

Fine grained (cohesive), or over-consolidated materials, require the highest amount of pore-water pressure to initiate failure, and exhibit a brittle style of deformation where strain localises and develops a confined shear surface. This indicates, that while fine grained and over-consolidated fill is less susceptible to rainfall-induced failure, the material may be prone to more rapid failure behaviour if pore-water pressure is sufficient enough in the slope.

Shear zone liquefaction as a result of increasing pore-water pressure was not observed in any of the fill materials suggesting that the shear surface did not form through this process in the conditions tested. Excess pore-water pressures were generated in response to rapid shearing, however, suggesting that post-failure liquefaction could occur in certain conditions once a landslide has been triggered. This post-failure liquefaction would require pore-water pressures to be sufficiently elevated and sustained within a shear zone that does not have adequate drainage.

These results have been used to develop a conceptual model of how debris flow-slides may develop from fill slopes during rainstorms. This model is broadly consistent with those previously proposed by Sassa (2000) and Iverson (2005), requiring shearing-induced contraction of the shear zone and the subsequent generation of excess pore-

water pressures. If sufficient pore-water pressures are generated and sustained, liquefaction can then occur.

The model indicates that fluidised, long runout fill slope failures require certain conditions to occur. Firstly, convergent topography that acts to concentrate groundwater flow and/or drainage during rainfall is necessary to develop the saturated conditions that are required. Secondly, soil that is not only susceptible to shearing-induced contraction, but also has a permeability that allows the generated pore-water pressures to be sufficiently maintained, is necessary.

This study has provided new insight which could improve the ability to identify susceptible slopes and develop management practices to mitigate their future hazard. Specifically, based on the conditions identified as conducive to liquidised failure behaviour, the most suitable mitigation strategies are the effective drainage of vulnerable slopes and appropriate consolidation of fill material.

7.1 Recommendation for future research

Whilst this study has identified a credible mechanism of failure for the observed fluidised fill slope landslides in the Wellington Region, this empirical data could now be used to underpin future fill slope hazard research.

Although rapid direct shear testing identified that post-failure liquefaction is a credible model for explaining the fluidised failures in Wellington's fill slopes, the data was not able to deduce if the grain-crushing or simple contraction mechanisms, if not both, were observed. Carrying out detailed particle-size analysis on a sample prior and post direct rapid shear testing would allow this differentiation to be made, if it was the case that only one of the mechanisms was acting.

Pore-pressure inflation (PPI) testing that replicated rainfall-induced failure was successfully undertaken, it should also be acknowledged that rainfall can fall with various intensities and patterns, which would likely result in differing patterns of displacement and potentially different failure mechanisms. Carrying out further PPI scenarios, using different rates and/or patterns of pore-water pressure change, would help development a much more complete picture of how fill slopes may fail under various rainfall conditions.

Additionally, another avenue of research which would further develop a more complete picture of the hazard posed by rainfall-induced fill slope failures in

Wellington is the effect of seismicity. With multiple active faults running through the region, Wellington experiences large amounts of seismic activity each year. While seismicity alone can be responsible for landsliding, it also has the potential to alter the physical properties of the fill material, and in turn, influence their susceptibility to rainfall-induced failure. Prior to PPI testing, using the DBPSB to run a series of tests that replicate the effects of seismicity on the fill material will help illustrate how the susceptibility to rainfall-induced failure evolves with seismic activity. In addition to the findings from this thesis, testing for the effects of seismicity will further the understanding of researchers and practitioners regarding the hazard posed by Wellington's fill slopes.

8 References

Aleotti, P., & Chowdhury, R. (1999). Landslide hazard assessment: summary review and new perspectives. *Bulletin of Engineering Geology and the Environment, 58*(1), 21-44.

Allison, R. J., & Brunsden, D. (1990). Some mudslide movement patterns. *Earth Surface Processes and Landforms, 15*(4), 297-311.

Anderson, S. A., & Sitar, N. (1995). Shear strength and slope stability in a shallow clayey soil regolith. *Reviews in Engineering Geology, 10*, 1-11.

Beard, D., & Weyl, P. (1973). Influence of texture on porosity and permeability of unconsolidated sand. *AAPG bulletin, 57*(2), 349-369.

Begg, J., & Johnston, M. (2000). Geology of the Wellington area. 1: 250 000 Geological map 10. *Institute of Geological and Nuclear Sciences, Lower Hutt, New Zealand*.

Bishop, A. W. (1973). The stability of tips and spoil heaps. *Quarterly Journal of Engineering Geology and Hydrogeology, 6*(3-4), 335-376.

Bjerrum, L. (1967). Progressive failure in slopes of overconsolidated plastic clay and clay shales. *Journal of Soil Mechanics & Foundations Div*.

Blight, G. (2008). Slope failures in municipal solid waste dumps and landfills: a review. *Waste Management & Research, 26*(5), 448-463.

Blight, G., & Fourie, A. (2005). Catastrophe revisited–disastrous flow failures of mine and municipal solid waste. *Geotechnical and Geological Engineering, 23*(3), 219-248.

Boyer, S., & Daly, M. (2013, June 1). Wellington homes evacuated by landslide. *Dominion Post*. Retrieved from http://www.stuff.co.nz/national/8745337/Wellington-homes-evacuated-by-landslide

Brain, M. J., Rosser, N. J., Sutton, J., Snelling, K., Tunstall, N., & Petley, D. N. (2015). The effects of normal and shear stress wave phasing on coseismic landslide displacement. *Journal of Geophysical Research: Earth Surface, 120*(6), 1009-1022.

Caine, N. (1980). The rainfall intensity: duration control of shallow landslides and debris flows. *Geografiska Annaler. Series A. Physical Geography*, 23-27.

Carey, J. M., & Petley, D. (2014). Progressive shear-surface development in cohesive materials; implications for landslide behaviour. *Engineering geology, 177*, 54-65.

Carey, J. M. (2011). *The progressive development and post-failure behaviour of deep-seated landslide complexes.* Durham University.

Carey, J. M., McSaveney, M., & Petley, D. (2017). Dynamic liquefaction of shear zones in intact loess during simulated earthquake loading. *Landslides, 14*(3), 789-804.

Carey, J. M., McSaveney, M. J., Lyndsell, B., & Petley, D. N. (2016). *Laboratory simulation of a slow landslide mechanism.* Paper presented at the Landslides and Engineered Slopes. Experience, Theory and Practice.

Carey, J. M., Moore, R., & Petley, D. (2015). Patterns of movement in the Ventnor landslide complex, Isle of Wight, southern England. *Landslides, 12*(6), 1107-1118. doi:10.1007/s10346-014-0538-1

Chappell, P. R. (2014). *The climate and weather of Wellington.* Retrieved from

Chen, H., Lee, C., & Law, K. (2004). Causative mechanisms of rainfall-induced fill slope failures. *Journal of geotechnical and geoenvironmental engineering, 130*(6), 593-602.

Collins, B. D., & Znidarcic, D. (2004). Stability analyses of rainfall induced landslides. *Journal of geotechnical and geoenvironmental engineering, 130*(4), 362-372.

Cooper, M., Bromhead, E., Petley, D., & Grants, D. (1998). The Selborne cutting stability experiment. *Geotechnique, 48*(1), 83-101.

Cotton, C. A. (1957). *Tectonic features in a coastal setting at Wellington.* Paper presented at the Transactions of the Royal Society of New Zealand.

Craig, R. F. (2004). *Craig's soil mechanics*: CRC Press.

Crosta, G. B., & Frattini, P. (2008). Rainfall-induced landslides and debris flows. *Hydrological processes, 22*(4), 473-477.

Crozier, M. J. (1986). *Landslides: causes, consequences & environment*: Taylor & Francis.

Crozier, M. J. (1999). Landslides *Environmental Geology* (pp. 371-375): Springer.

Crozier, M. J., & Glade, T. (2005). Landslide hazard and risk: issues, concepts and approach. *Landslide hazard and risk*, 1-40.

Cruden, D. M. (1991). A simple definition of a landslide. *Bulletin of Engineering Geology and the Environment, 43*(1), 27-29.

Cruden, D. M., & Varnes, D. J. (1996). Landslides: investigation and mitigation. Chapter 3-Landslide types and processes. *Transportation research board special report*(247).

Dai, F., Lee, C., & Ngai, Y. Y. (2002). Landslide risk assessment and management: an overview. *Engineering geology, 64*(1), 65-87.

Das, B. M. (2013). *Advanced soil mechanics*: CRC Press.

Davies, E., Harding, H., & Lawrence, V. (1967). Report of the Tribunal Appointed to Inquire into the Disaster at Aberfan on October 21st 1966: London: Her Majesty's Stationary Office.

Dawson, R., Morgenstern, N., & Stokes, A. (1998). Liquefaction flowslides in Rocky Mountain coal mine waste dumps. *Canadian Geotechnical Journal, 35*(2), 328-343.

De Blasio, F. V. (2011). Friction, Cohesion, and Slope Stability *Introduction to the Physics of Landslides* (pp. 23-52): Springer.

Duff, M. (2013, June 10). A Wellington problem that won't go away. *Dominion Post*. Retrieved from http://www.stuff.co.nz/dominion-post/news/wellington/8771245/A-Wellington-problem-that-won-t-go-away

Eyles, R., Crozier, M., & Wheeler, R. (1978). Landslips in Wellington city. *New Zealand Geographer, 34*(2), 58-74.

Eyles, R., & McConchie, J. (1992). Wellington. *Landforms of New Zealand. Longman Paul, Aukland*, 382-406.

Fernandes, N. F., Guimarães, R. F., Gomes, R. A., Vieira, B. C., Montgomery, D. R., & Greenberg, H. (2004). Topographic controls of landslides in Rio de Janeiro: field evidence and modeling. *Catena, 55*(2), 163-181.

Glade, T. (1997). *The Temporal and Spatial Occurrence of Rainstorm-triggered Landslide Events in New Zealand: an Investigation Into the Frequency, Magnitude and Characteristics of Landslide Events and Their Relationship with Climatic and Terrain Characteristics: A Thesis Submitted [to The] Victoria University of Wellington in Fulfilment of the Requirements for the Degree of Doctor of Philosophy in Physical Geography*.

Glade, T. (1998). Establishing the frequency and magnitude of landslide-triggering rainstorm events in New Zealand. *Environmental Geology, 35*(2), 160-174.

GNS. (2018). National Landslide Database. Available from GNS Science National Landslide Database Retrieved 9/02/2018 http://data.gns.cri.nz/landslides/index.html

Grant, H., Guard, J., & Wall, K. (2005). *Natural hazards: background report*: Greater Wellington.

Guzzetti, F., Peruccacci, S., Rossi, M., & Stark, C. P. (2007). Rainfall thresholds for the initiation of landslides in central and southern Europe. *Meteorology and atmospheric physics, 98*(3-4), 239-267.

Guzzetti, F., Peruccacci, S., Rossi, M., & Stark, C. P. (2008). The rainfall intensity–duration control of shallow landslides and debris flows: an update. *Landslides, 5*(1), 3-17.

Hancox, G. T., Dellow, G. D., Massey, C., & Perrin, N. D. (2007). *Reconnaissance studies of landslides caused by the July-October 2006 rainstorms in southern North Island, New Zealand*: GNS Science.

Hatibu, N., & Hettiaratchi, D. (1993). The transition from ductile flow to brittle failure in unsaturated soils. *Journal of agricultural engineering research, 54*(4), 319-328.

Helmstetter, A., Sornette, D., Grasso, J. R., Andersen, J. V., Gluzman, S., & Pisarenko, V. (2004). Slider block friction model for landslides: Application to Vaiont and La Clapiere landslides. *Journal of Geophysical Research: Solid Earth, 109*(B2).

Huang, Y., Zhang, W., Xu, Q., Xie, P., & Hao, L. (2012). Run-out analysis of flow-like landslides triggered by the Ms 8.0 2008 Wenchuan earthquake using smoothed particle hydrodynamics. *Landslides, 9*(2), 275-283.

Hungr, O. (2007). Dynamics of rapid landslides. *Progress in landslide science*, 47-56.

Hungr, O., Dawson, R., Kent, A., Campbell, D., & Morgenstern, N. (2002). Rapid flow slides of coal-mine waste in British Columbia, Canada. *Reviews in Engineering Geology, 15*, 191-208.

Hungr, O., Leroueil, S., & Picarelli, L. (2014). The Varnes classification of landslide types, an update. *Landslides, 11*(2), 167-194.

Hunt, T., & George, D. (2017, April 7). Slip-prone Wellington hillside to get full examination after two massive mudslides. *Dominion Post*. Retrieved from https://www.stuff.co.nz/national/91318527/Three-homes-evacuated-in-Wellington-after-land-slip-in-suburb-of-Kingston

Hutchinson, J. (1986). A sliding–consolidation model for flow slides. *Canadian Geotechnical Journal, 23*(2), 115-126.

Iverson, R. M. (2005). Regulation of landslide motion by dilatancy and pore pressure feedback. *Journal of Geophysical Research: Earth Surface, 110*(F2).

Iverson, R. M., George, D. L., Allstadt, K., Reid, M. E., Collins, B. D., Vallance, J. W., . . . Magirl, C. S. (2015). Landslide mobility and hazards: implications of the 2014 Oso disaster. *Earth and Planetary Science Letters, 412*, 197-208.

Iverson, R. M., & LaHusen, R. G. (1989). Dynamic pore-pressure fluctuations in rapidly shearing granular materials. *Science, 246*(4931), 796-800.

Iverson, R. M., Reid, M., Iverson, N. R., LaHusen, R., Logan, M., Mann, J., & Brien, D. (2000). Acute sensitivity of landslide rates to initial soil porosity. *Science, 290*(5491), 513-516.

Iverson, R. M., Reid, M. E., & LaHusen, R. G. (1997). Debris-flow mobilization from landslides. *Annual Review of Earth and Planetary Sciences, 25*(1), 85-138.

Khan, S., Crozier, M., & Kennedy, D. (2012). Influences of place characteristics on hazards, perception and response: a case study of the hazardscape of the Wellington Region, New Zealand. *Natural hazards, 62*(2), 501-529.

Kilburn, C. R., & Petley, D. N. (2003). Forecasting giant, catastrophic slope collapse: lessons from Vajont, Northern Italy. *Geomorphology, 54*(1-2), 21-32.

Lavigne, F., Wassmer, P., Gomez, C., Davies, T. A., Hadmoko, D. S., Iskandarsyah, T. Y. W., . . . Heng, M. B. (2014). The 21 February 2005, catastrophic waste avalanche at Leuwigajah dumpsite, Bandung, Indonesia. *Geoenvironmental Disasters, 1*(1), 10.

Legros, F. (2002). The mobility of long-runout landslides. *Engineering geology, 63*(3), 301-331.

Malone, A. (1988). The role of government in landslide disaster prevention in Hong Kong and Indonesia. *Geotechnical Engineering, 19*(2), 227-252.

Massey, C. I., Petley, D. N., & McSaveney, M. (2013). Patterns of movement in reactivated landslides. *Engineering geology, 159*, 1-19.

Montgomery, D. R., & Dietrich, W. E. (1994). A physically based model for the topographic control on shallow landsliding. *Water Resources Research, 30*(4), 1153-1171.

Moore, P. L., & Iverson, N. R. (2002). Slow episodic shear of granular materials regulated by dilatant strengthening. *Geology, 30*(9), 843-846.

Nemčok, A., Pašek, J., & Rybář, J. (1972). Classification of landslides and other mass movements. *Rock mechanics, 4*(2), 71-78.

Ng, K. (2007). *Mechanisms of Shallow Rainfall-induced Landslides in Residuali Soils in Humid Tropical Environments.* Durham University.

Ng, K., & Petley, D. (2009). The use of pore pressure reinflation testing in landslide management in Hong Kong. *Quarterly Journal of Engineering Geology and Hydrogeology, 42*(4), 487-498.

NIWA. (n.d.). *CliFlo: NIWA's National Climate Database on the Web*. Retrieved from: http://cliflo.niwa.co.nz/

Okada, Y., Sassa, K., & Fukuoka, H. (2000). Liquefaction and the steady state of weathered granitic sands obtained by undrained ring shear tests: a fundamental study of the mechanism of liquidized landslides. *Journal of Natural Disaster Science, 22*(2), 75-85.

Okada, Y., Sassa, K., & Fukuoka, H. (2004). Excess pore pressure and grain crushing of sands by means of undrained and naturally drained ring-shear tests. *Engineering geology, 75*(3-4), 325-343.

Okura, Y., Kitahara, H., Ochiai, H., Sammori, T., & Kawanami, A. (2002). Landslide fluidization process by flume experiments. *Engineering geology, 66*(1-2), 65-78.

Palmer, A. C., & Rice, J. (1973). *The growth of slip surfaces in the progressive failure of over-consolidated clay.* Paper presented at the Proc. R. Soc. Lond. A.

Petley, D. (2010). Landslide hazards. *Geomorphological hazards and disaster prevention. Cambridge University Press, Cambridge*, 63-74.

Petley, D., Bulmer, M., & Murphy, W. (2002). Patterns of movement in rotational and translational landslides. *Geology, 30*(8), 719-722.

Petley, D., Higuchi, T., Petley, D., Bulmer, M., & Carey, J. M. (2005). Development of progressive landslide failure in cohesive materials. *Geology, 33*(3), 201-204.

Petley, D., Petley, D., & Allison, R. (2008). Temporal prediction in landslides-Understanding the Saito effect.

Rahardjo, H., Ong, T., Rezaur, R., & Leong, E. C. (2007). Factors controlling instability of homogeneous soil slopes under rainfall. *Journal of geotechnical and geoenvironmental engineering, 133*(12), 1532-1543.

Saito, M. (1965). *Forecasting the time of occurrence of a slope failure.* Paper presented at the Proceedings of the 6th international conference on soil mechanics and foundation engineering.

Saito, M. (1969). *Forecasting time of slope failure by tertiary creep.* Paper presented at the Proc. 7th Int. Conf on Soil Mechanics and Foundation Engineering, Mexico City.

Sassa, K. (1989). Geotechnical classification of landslides. *Landslide News, 3*(1), 21-24.

Sassa, K. (2000). *Mechanism of flows in granular soils.* Paper presented at the ISRM International Symposium.

Sassa, K., Fukuoka, H., Scarascia-Mugnozza, G., & Evans, S. (1996). Earthquake-induced-landslides: distribution, motion and mechanisms. *Soils and Foundations, 36*(Special), 53-64.

Sassa, K., Fukuoka, H., Wang, G., & Ishikawa, N. (2004). Undrained dynamic-loading ring-shear apparatus and its application to landslide dynamics. *Landslides, 1*(1), 7-19.

Schulz, W. H., McKenna, J. P., Kibler, J. D., & Biavati, G. (2009). Relations between hydrology and velocity of a continuously moving landslide—evidence of pore-pressure feedback regulating landslide motion? *Landslides, 6*(3), 181-190.

Selby, M. J. (1993). *Hillslope Materials and Processes*: Oxford University Press.

Shepherd, R. G. (1989). Correlations of permeability and grain size. *Groundwater, 27*(5), 633-638.

Sidle, R. C., & Ochiai, H. (2006). *Landslides: processes, prediction, and land use* (Vol. 18): American Geophysical Union.

Skempton, A. (1964). Long-term stability of slopes. *Geotechnique, 14*(2), 75-102.

Take, W., Bolton, M., Wong, P., & Yeung, F. (2004). Evaluation of landslide triggering mechanisms in model fill slopes. *Landslides, 1*(3), 173-184.

Terzaghi, K. (1950). *Mechanism of Landslides*: Harvard University, Department of Engineering.

Terzaghi, K., Peck, R. B., & Mesri, G. (1996). *Soil mechanics in engineering practice*: John Wiley & Sons.

Tomlinson, A. I., & Dyke, A. (1977). *The Wellington and Hutt Valley flood of 20 December 1976*: New Zealand Meteorological Service.

Tsai, T. L. (2008). The influence of rainstorm pattern on shallow landslide. *Environmental Geology, 53*(7), 1563-1569.

Varnes, D. J. (1958). Landslide types and processes. *Landslides and engineering practice, 24*, 20-47.

Varnes, D. J. (1978). Slope movement types and processes. *Special report, 176*, 11-33.

Vickers, B. (1978). *Soil mechanics*: Crosby Lockwood Staples.

Viggiani, G., Finno, R., & Harris, W. (1994). Experimental observations of strain localisation in plane strain compression of a stiff clay. *Localization and bifurcation theory for soils and rocks*, 189-198.

Voight, B., & Pariseau, W. (1978). Rockslides and avalanches: an introduction. *Rockslides and avalanches, 1*.

Wang, F., Sassa, K., & Wang, G. (2002). Mechanism of a long-runout landslide triggered by the August 1998 heavy rainfall in Fukushima Prefecture, Japan. *Engineering geology, 63*(1), 169-185.

Wang, G., & Sassa, K. (2001). Factors affecting rainfall-induced flowslides in laboratory flume tests. *Geotechnique, 51*(7), 587-599.

Wang, G., & Sassa, K. (2002). Post-failure mobility of saturated sands in undrained load-controlled ring shear tests. *Canadian Geotechnical Journal, 39*(4), 821-837.

Wang, G., & Sassa, K. (2003). Pore-pressure generation and movement of rainfall-induced landslides: effects of grain size and fine-particle content. *Engineering geology, 69*(1), 109-125.

Appendix A: Atterberg limit testing sheet

ENGINEERING GEOLOGY SECTION
NZ GEOLOGICAL SURVEY DSIR

LIQUID AND PLASTIC LIMITS CLASSIFICATION

PROJECT _____ MATERIAL Fill LAB No EN1336

WATER CONTENT DATE _____

Dish No.	Dish+wet soil	Dish+dry soil	Dish mass	Loss	Dry soil	w
504A	165.44	147.93	46.90	7.51	101.03	7.4
505A	171.01	167.20	47.64	8.81	119.56	7.7

WATER CONTENT (w)% 7.6

LIQUID AND PLASTIC LIMITS DATE _____

WHOLE SOIL ☐ FRACTION ____% PASSING ____ SIEVE CLAY CONTENT OF FRACTION ____%
SEPARATED BY SIEVING/HAND NATURAL/AIR DRY/OVEN DRY

No. of blows	Av. blows	Dish No.	D.+wet soil	D.+dry soil	Dish mass	Loss	Dry soil	w
	22	C24	14.51	12.37	5.04	2.14	7.33	29.2
	30	C33	19.44	16.29	5.05	3.15	11.24	28.0
	25	C42	14.95	12.74	5.00	2.21	7.74	28.6
		C66	7.36	7.01	5.08	0.35	1.93	18.1
		C47	7.79	7.35	5.04	0.44	2.31	19.0
		C25	7.42	6.96	5.03	0.46	1.93	20.2

Calculation of "One point" L.L.
$L.L. = w \times k$
where
w = water content
and K is given below

BLOWS	K
20	0·977
21	0·983
22	0·987
23	0·992
24	0·996
25	1·000
26	1·004
27	1·008
28	1·012
29	1·015
30	1·019

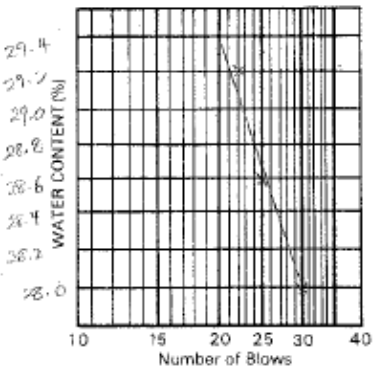

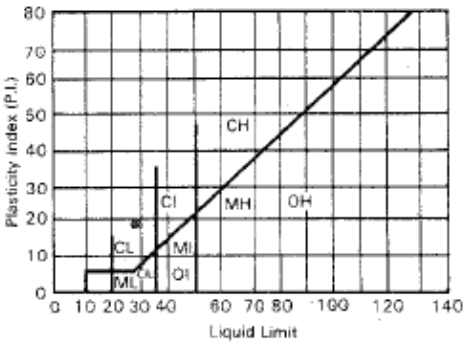

CLASS CL

"ONE POINT" LIQUID LIMIT

BLOWS	22	30	25			
W/C	29.2	28.0	28.6			
LL	28.8	28.6	28.6			

REMARKS

Liquid Limit	(W_L)	28.6
Plastic Limit	(W_p)	19.1
Plasticity Index	$(W_L - W_p)$	9.4
Liquidity Index	$\left(\frac{W - W_p}{W_L - W_p}\right)$	-1.2
Activity	$\frac{PI}{\text{Clay Content}}$	

TESTED BY Rmd CHECKED BY BL LAB No EN1336

Appendix B: DBPSB testing results

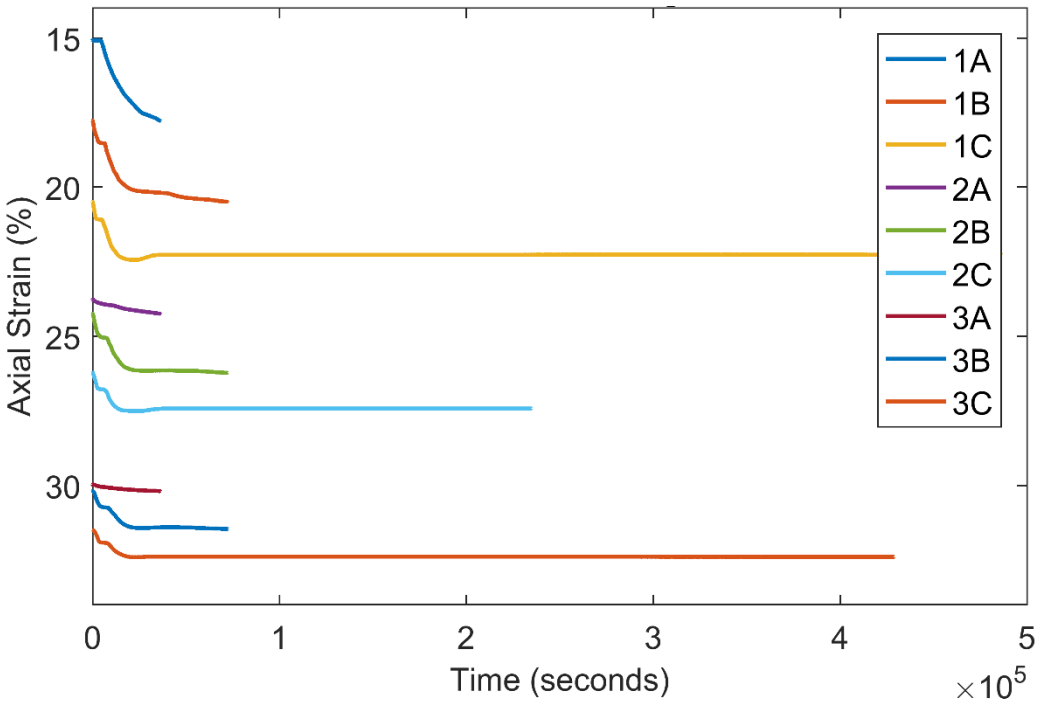

Fig. B1: Consolidation that occurred during CFE testing on sample PSD1

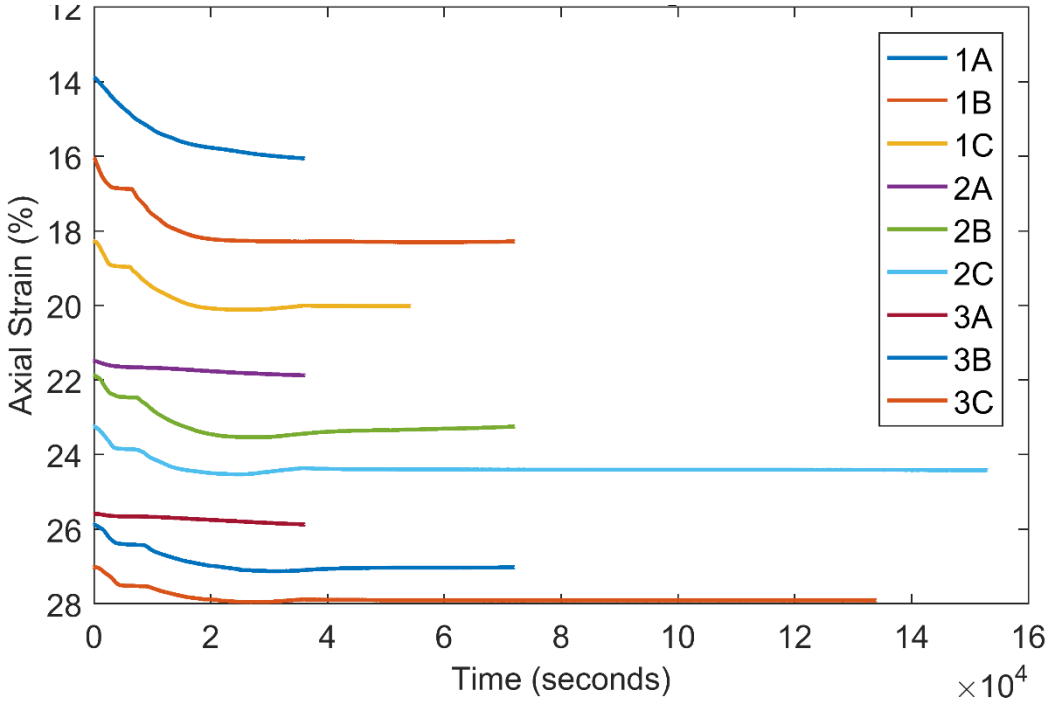

Fig. B2: Consolidation that occurred during CFE testing on sample PSD2

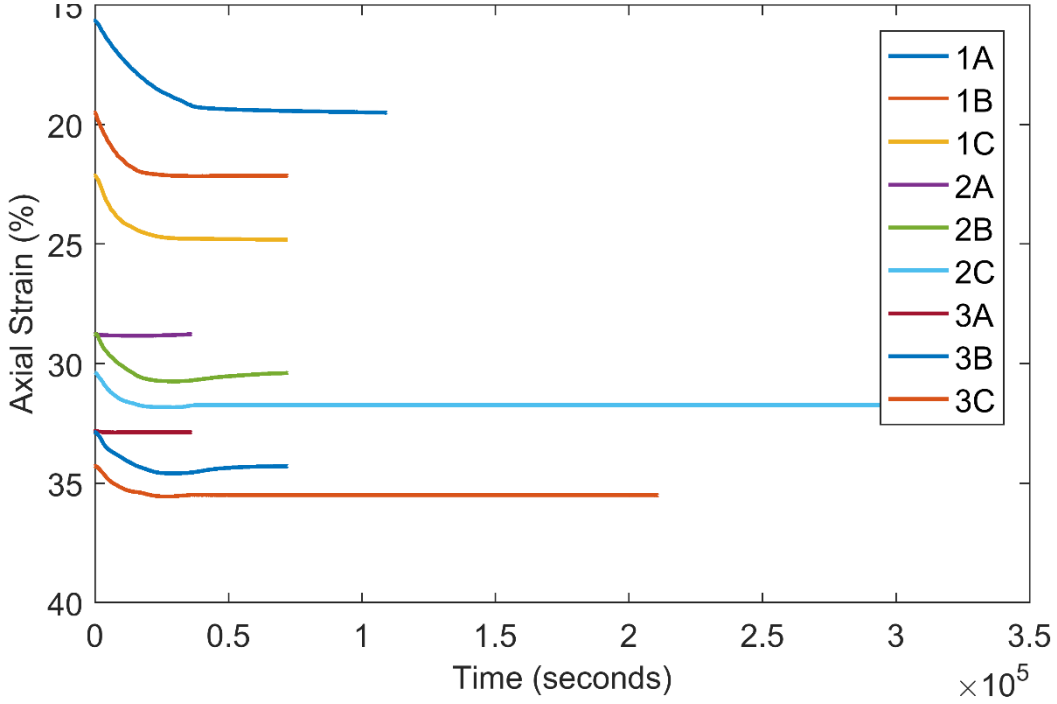

Fig. B3: Consolidation that occurred during CFE testing on sample PSD3

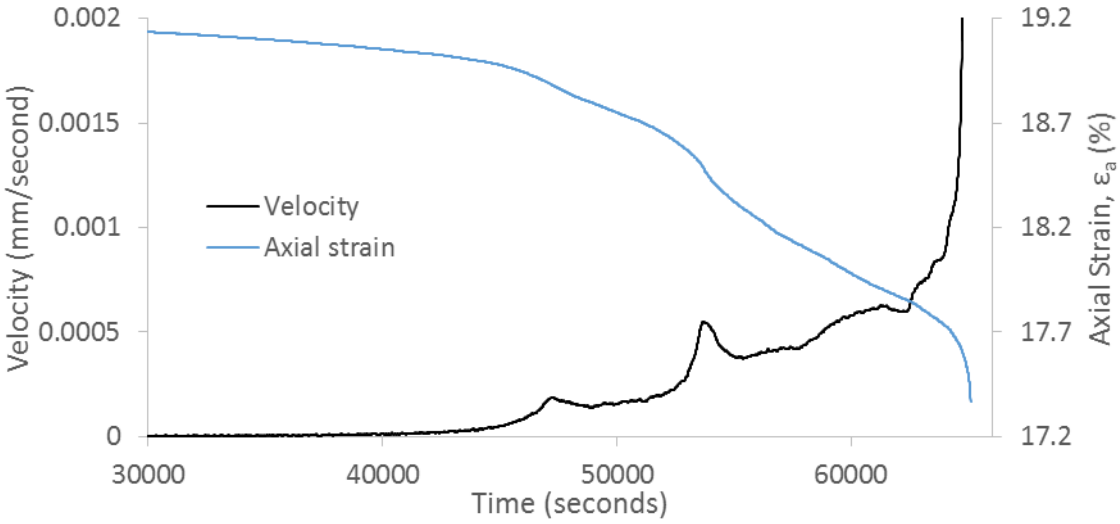

Fig. B4: Comparing Velocity and axial strain during linear PPI test on the PSD3 sample.

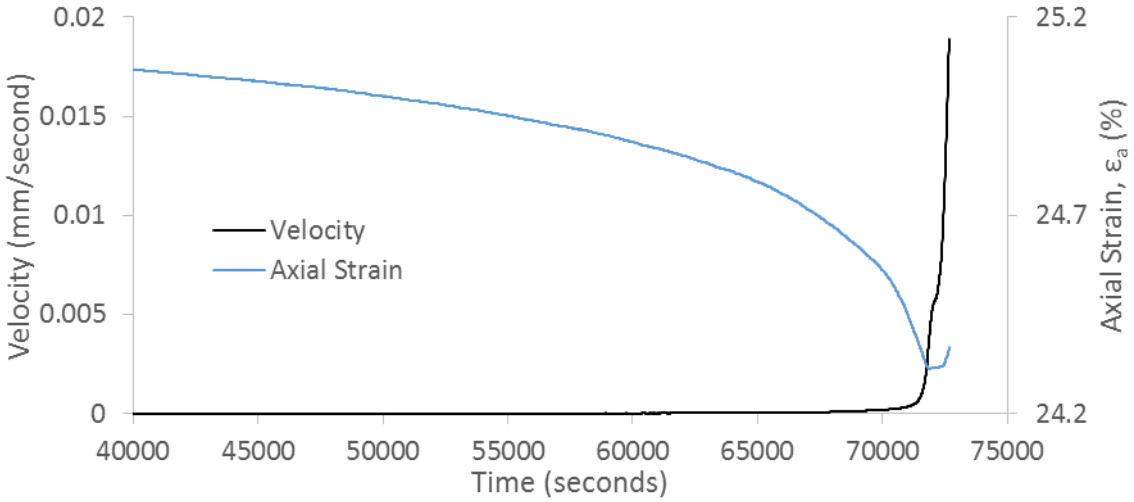

Fig. B5: Comparing Velocity and axial strain during linear PPI test on the PSD1 sample.

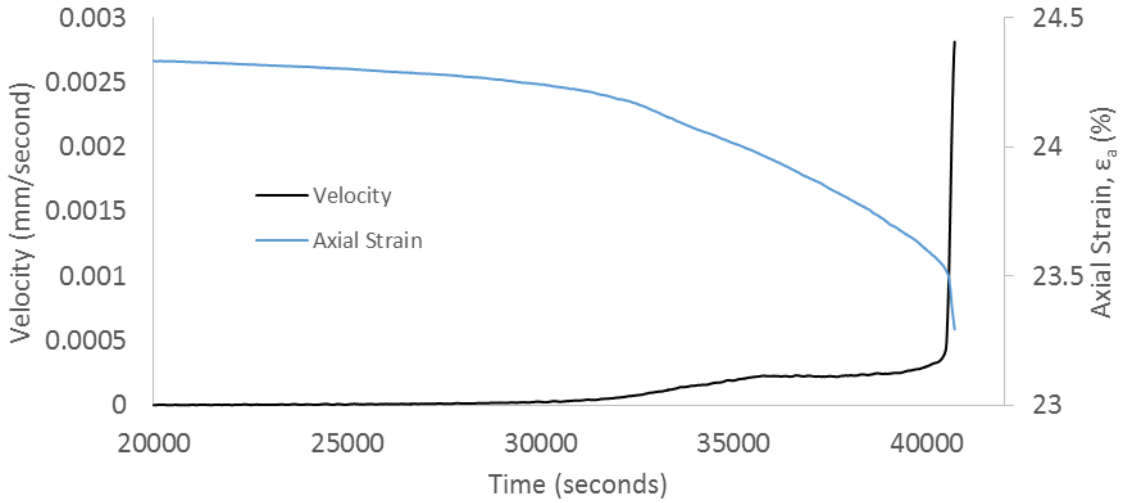

Fig. B6: Comparing Velocity and axial strain during linear PPI test on the PSD2 OC2 sample.